Ozone_cci

Algorithm Theoretical Basis Document
Phase 2 Version 2 (ATBDv2)

Reference: Ozone_cci_ATBD_Phase2_V2.docx

Date of issue: 7 Dec 2017

Distributed to: Ozone_cci Consortium

WP Manager: N. Rahpoe
WP Manager Organization: UBR

Other partners:
EOST: DLR-IMF, BIRA-IASB, RAL, KNMI, UBR, LATMOS, FMI, U. Saskatchewan, U. Chalmers, U. Oxford, IFAC Florence, ISAC Bologna
VALT: AUTH, NKUA, BIRA-IASB
CRG: DLR-PA, KNMI

This work is supported by the European Space Agency

DOCUMENT PROPERTIES

Title		ATBD version 2 Phase 2		
Reference		Ozone_cci_ATBD_Phase2_V2.docx		
Issue		00		
Revision		00		
Status		Final		
Date of issue		7 Dec 17		
Document type		Deliverable		

	FUNCTION	NAME	DATE	SIGNATURE
AUTHORS	Scientists	Ronald van der A Cristen Adams Peter Bernath Thomas von Clarmann Melanie Coldewey-Egbers Doug Degenstein Anu Dudhia Robert Hargreaves Alexandra Laeng Cristophe Lerot Diego Loyola Jacob van Peet Nabiz Rahpoe Viktoria Sofieva Gabriele Stiller Johanna Tamminen Joachim Urban Michel Van Roozendael Mark Weber Christophe Lerot Thomas Danckaert Rosa Astoreca Klaus-Peter Heue Patrick Sheese Kaley Walker Simo Tukiainen		
EDITORS	Scientists	**Phase 1** Alexandra Laeng (V1) Gabriele Stiller (V1) Mark Weber (V2) **Phase 2** Nabiz Rahpoe (V1)		
REVIEWED BY	ESA Technical Officer	Claus Zehner		
ISSUED BY	Scientist	Nabiz Rahpoe		

DOCUMENT CHANGE RECORD ATBD V1

Issue	Revision	Date	Modified items	Observations
00	00	25/05/2011		Creation of document
		15/07/2011	Timely provided processors' descriptions are inserted	
01	00	11/10/2011	All partners' processors' descriptions are inserted	
01	01	28/10/2011	Two out of three missing error budgets are inserted	
01	02	21/11/2011	Sections about compliance with URD are added	
01	03	01/12/2011		Version submitted to ESA
01	04	10/01/2012	ESA remarks incorporated. Last missing inputs inserted.	Version re-submitted to ESA
01	05	25/07/2012	Geophysical validation of GOMOS uncertainties is added as appendix	
01	06	20/09/2012	Updates on MIPAS algorithms are incorporated. Geophysical validation of MIPAS processors' error bars is incorporated as an appendix.	
01	07	5/10/2012	TN on re-gridding of diagnostics of atmospheric profiles is incorporated as appendix	Removed in ATBD V2
01	08	7/11/2012	Precision validation of SCIAMACHY limb profiles is incorporated as appendix	
01	09	12/03/2013	Precision validation of four MIPAS algorithms is incorporated as appendix	
01	10	18/04/2013	Error validation from three ENVISAT limb sensors decided to form one homogenized appendix. Individual GOMOS, SCIA and MIPAS appendices are taken out.	Version handed over to IUP Bremen who will be in charge of ATBD v2

Issue	Revision	Date	Modified items	Observations
02	01	27/11/2013	Some initial reformatting Accepting Changes from previous version	
02	02	28/11/2013	Update of Section 3.1 (total ozone)	
02	03	05/12/2013	Update of Sections 3.1.2 (merged total ozone), 3.2.5.2 (merged nadir ozone profile), and 3.3.10 (limb ozone data merging) Equation numbers added Clean up of MS Word literature data base for references	
02	04	08/12/2013	Add ACE-FTS (Section 3.3.9)	
02	05	13/12/2013	Add SMR (Section 3.3.8)	
02	06	18/03/2014	Add members of MIPAS consortium to author list	Final version from O3_CCI Phase 1
00	00	12/08/2014		Continuation of document for Phase 2
00	01	14/10/2014	• Three MIPAS algorithm descriptions removed • IASI FORLI added • Reference updated	
01	00	27/02/2015	• Tropospheric Ozone Column ECV added (Chapter 5) • Description of Limb-Nadir-Matching Algorithm	
01	01	06/07/2015	Update of Total Ozone GODFIT algorithm in Sec. 2.1	
01	02	24/09/2015	Include Tropical tropospheric column (TTOC) in Sec. 5	

02	00	03/02/2016	Some initial reformatting Accepting Changes from previous version	
02	01	08/02/2016	Description of U.S. sensors in Chapter 4.7 added	
03	00	30/05/2016	ACE-FTS V3.5 added GOMOS BRIGHT LIMB V1.2 added	
04	00	15/07/2017	SCIAMACHY V3.5 MLS 4.2 SABER V2.0	
04	01	15/08/2017	Limb MZM & MMZM	
04	02	25/08/2017	Reformatting. Consistent equation & figure numbering.	
04	03	04/09/2017	Checked and approved.	
04	04	06/12/2017	ALGOM2s (4.3), Limb Merged LatLon dataset (5.1.4), mesospheric (5.1.5) and UTLS datasets (5.1.6) by Viktoria and Alexandra	
00	00	07/12/2017	Release of Version 2	Final Issue

Table of Contents

1   Executive summary

The Algorithm Theoretical Basis Document version 0 (ATBDv0) is a deliverable of the ESA Ozone_cci project (http://www.esa-ozone-cci.org/). The Ozone_cci project is one of twelve projects of ESA's Climate Change Initiative (CCI). The Ozone_cci project will deliver the Essential Climate Variable (ECV) Ozone in line with the "Systematic observation requirements for satellite-based products for climate" as defined by GCOS (Global Climate Observing System) in (GCOS-107 2006): "Product A.7: Profile and total column of ozone".

During the first 2 years of this project, which started 1st Sept 2010, a so-called Round Robin (RR) exercise has been conducted. During this phase several existing retrieval algorithms to produce vertical profiles and total columns of ozone from satellite observations have been compared. For some of participating data products several algorithms have been used. At the end of the Round-Robin phase, algorithms have been selected as CCI baselines and used to generate the Ozone_cci Climate Research Data Package (CRDP) which has been publicly released in early 2014.

In April 2014, Ozone_cci entered in its second phase which will cover a 3-year time period. The purpose of this document is to provide an update of scientific descriptions of ozone algorithms as implemented at the start of Ozone_cci Phase-2. This includes specifications of data characterization, error budgets, quality flags, and auxiliary information provided with the products (e.g. averaging kernels).

1.1   Applicable documents

Ozone_cci SoW
Ozone_cci DARD
Oone_cci PSD
Ozone_cci_URD
ESA CCI Project Guidelines

1.2   Data and Error Characterization

1.2.1   Introduction

The purpose of this chapter is to establish a common terminology on error estimation and characterization, to summarize the essentials of error propagation, to provide an overview of which diagnostic quantities are available for the data sets used in this project and to suggest recipes how to reasonably characterize data when some diagnostic quantities are missing. Terminology is a particular problem because most of the related literature, particularly that recommended in (CCI-GUIDELINES 2010), namely the (Beers 1957), (Hughes and Hase 2010) and (BIPM 2008), but also (CMUG-RBD 2010), refers to scalar quantities while profiles of atmospheric state variables are by nature vectors where error correlations are a major issue. Further, there exists a chaotic ambiguity in terminology: the term "accuracy" has at least two contradictory definitions, depending on which literature is consulted; the meaning of the term "systematic error" is understood differently, the term bias changes its meaning according to the context. Part of the problem arises because the usual terminology has been developed for laboratory measurements where the same value can be measured several times under constant

conditions, which obviously is not possible for atmospheric measurements. Another problem with established terminology is that it does not distinguish between error estimates generated by propagation of primary uncertainties through the system and those generated statistically from a sample of measurements. The purpose of this chapter is to attempt to clarify these issues.

1.2.2 Theory (the ideal world)

In this chapter different types of errors will be defined, the principles of error propagation will be summarized and several kinds of error estimates will be discussed. We assume that we have indirect measurements. The processing chain is as follows: the step from raw data in technical units (e.g. detector voltages, photon counts etc) to calibrated measurement data in physical units (spectral radiances, spectral transmittances etc) are called level-1 processing; resulting data are called "level-1 data" and referred to by the symbol $\mathbf{y}$: y is a vector containing all measurements used during one step of the data analysis. The inference of geophysical data from the level-1 data is called "level-2 processing". The level-2 data product is called $\hat{\mathbf{x}}$. This step requires some kind of "retrieval" or "inversion", involving a radiative transfer model f. As level-2 processing often is carried out using Newtonean iteration, we assume that f is sufficiently linear around $\hat{\mathbf{x}}$ so that linear error estimation theory holds. Any auxiliary or ancillary data which are needed to generate level-2 data are referred to by the symbol $\mathbf{u}$ (e.g. spectroscopic data, measurement geometry information etc): $\mathbf{u}$ is a vector containing all these auxiliary or ancillary data. The direct problem – i.e. the simulation of measurements by the forward model – is

$$\mathbf{y} = f(\mathbf{x}, \mathbf{u})$$
Eq. 1.1

The inverse problem, i.e. the estimation of the level-2 product from the level-1 product is

$$\hat{\mathbf{x}} = \mathbf{x}_{initguess} + \mathbf{G}(\mathbf{y} - f(\mathbf{x}_{initguess}, \mathbf{u}))$$
Eq. 1.2

The ^ symbol is, in agreement with (C. D. Rodgers 2000) used for estimated rather than true quantities.

1.3 Errors

The error is the difference of the measured or estimated state of the atmosphere $\hat{\mathbf{x}}$ and the true state of the atmosphere $\mathbf{x}$[1]. Both $\hat{\mathbf{x}}$ and $\mathbf{x}$ are related to a certain finite air volume. Error estimation concepts referring to the state of the atmosphere at a point of infinitesimal size are in conflict with the nature of most atmospheric state variables because quantities like concentration, mixing ratio or temperature are defined only for an ensemble of molecules. For an infinitesimal point in space the mixing ratio of species n is either undefined (if there is no molecule at this moment) or one (if there is a molecule of species n at this point) or zero (if the point is taken by a molecule of a species different from n). This implies that it is only meaningful to report an error along with some characterization of the extent of the air volume it refers to.

---

[1] "True state of the atmosphere" is referred as "measurand" in (CCI-GUIDELINES 2010).

1.3.1 Type of errors

1.3.1.1 Classification by Origin

Parasite (illegitimate) error

This error can be removed by more careful procedure. Examples: errors of computations, algorithmic or coding errors, instrument disfunction. This type of error can hardly be predicted. Under favourable circumstances, their presence can be detected from outliers.

Noise

The level 1 product y is composed of a true signal $\mathbf{y_{true}}$ and some noise $\boldsymbol{\varepsilon}$. This measurement noise is mapped to the level 2 data and causes some error in the retrieved geophysical variables. We suggest to call the measurement noise related error in the level 1 data *"measurement noise"* ($\boldsymbol{\varepsilon_y}$), and the resulting error in the level 2 data - *"noise error"* ($\boldsymbol{\varepsilon_x}$). In the literature, this type of errors often is called "random error", but this terminology is misleading because the parameter errors (see below) also can have random characteristics. Thus, the random error goes beyond the measurement noise. However, and this is why this type of errors is called "statistical", its behaviour is subject to laws of mathematical statistics. When the measurement of quantity Q is repeated N times with statistical error σ_Q and zero systematic error, the mean value Q_{mean} tends toward the true value Q_{true} with an error $\sigma_Q / \sqrt{N}$.

Parameter errors

The retrieval of $\hat{x}$ from **y** involves other quantities **u** than the measurements **y** themselves, e.g. temperature information in a trace gas abundance retrieval, information on measurement geometry, or spectroscopic data to solve $f(\mathbf{x},\mathbf{u})$. Any errors in **u** will propagate to $\hat{x}$. We suggest calling the error estimates on **u** *"parameter uncertainties"* and their mapping on $\hat{x}$ *"parameter errors"*. The characteristics of the parameter errors can be random or systematic, according to the correlation of the parameter uncertainties.

More general, we suggest reserving the term "uncertainty" for the errors that come from other than measurements quantities involved in the retrieval.

Model errors

Typically the model f does not truly represent the radiative transfer through the atmosphere, due to physical simplification, coarse discretisation, etc. The mapping of these uncertainties to the **x**-space is called *model error*.

Smoothing error

The retrieval never represents the atmosphere at infinitesimal spatial resolution but is a smoothed picture of the atmosphere, and often contains some a priori information to stabilize the retrieval. Rodgers (2000) suggests to call the difference between the true atmospheric state at infinite spatial resolution and the smoothed state (which is possibly biased by a priori information) by "smoothing error". In older literature (Rodgers, 1990) this type of error was called "null-space error". We suggest not to follow the smoothing error concept for two reasons:

(1) the quantities under consideration are not defined for an infinitesimally small air volume,

(2) the evaluation of the smoothing error requires knowledge on the true small-scale variability of the atmosphere; this knowledge is more often unavailable than available. While for ozone the situation is slightly better, relevant information is still missing. Even the ozone sondes have calibration problems, their altitude coverage is limited to below 30 km, their data are sparse and they have their own uncertainties.

Instead we suggest reporting concentrations and estimated errors for a finite air volume along with a characterization of the spatial resolution.

1.3.1.2   Classification by Correlation Characteristics

Random error

An error component which is independent between two measurements under consideration is called random error. The noise error is a typical random error but also parameter errors can have a strong random component. The random error can be reduced by averaging multiple measurements. However, since we have no laboratory measurements but atmospheric measurements where the same measurement cannot be repeated, averaging implies loss of spatial and/or temporal resolution.

Systematic error

Systematic errors appear in the same manner in multiple measurements and thus do not cancel out by averaging. Typical systematic errors are model errors, errors in spectroscopic data, calibration errors. Errors can be systematic in many domains (see below). Conventionally this term is applied to errors systematic in the time domain. This convention, however, does not always help.

Correlated errors

Some errors are neither fully random nor fully systematic. We call these errors "correlated errors".

1.3.1.3   Suggested Terminology

The "precision" of an instrument/retrieval characterizes its random (in the time domain) error. It is the debiased root mean square deviation of the measured values from the true values. The precision can also be seen as scatter of multiple measurements of the same quantity. The difference between the measured and the true state can still be large, because there still can be a large systematic error component unaccounted by the precision.

The "bias" of an instrument/retrieval characterizes its systematic (in the time domain) error. It is the mean difference of the measured values from the true values.

The "total error" of an instrument/retrieval characterizes the estimated total difference between the measured and the true value. In parts of the literature the expected total error is called "accuracy" but we suggest not using this particular term because its use in the literature is ambiguous.

Caveat:

Whether an error is random or systematic depends on the applicable domain. Some errors are random in the time domain but systematic in the altitude domain. Other errors are systematic in the frequency domain but random in the inter-species domain. We illustrated this below with some typical examples:

1) Spectroscopic data (band intensity) will affect the entire ozone profile in quite a systematic way. If the zenith column amount is calculated by integrating densities over the profile, this error source is systematic, because all profile values are either too high or too low. If, in contrast, the total odd-oxygen budget is calculated from such measurements, the spectroscopic data error acts as random error, because the O_3 spectroscopic data error is independent of the atomic oxygen spectroscopic data error.

2) The pointing uncertainties of a limb sounding instrument can have a strong random component in altitude, i.e. the tangent altitude increments may vary in a random manner around the true or nominal increment. In contrast to the example 1), this error acts as random error when densities are integrated over the profile to give the zenith column amount, but will act as a systematic error when the total inorganic oxygen budget is calculated for one altitude.

In summary, it is of primary importance to always have the particular application in mind when a certain type of error is labelled "random" or "systematic".

1.3.1.4 Classification by way of assessment

The true error of the retrieval is not accessible because we do not know the true state of the atmosphere. We can only estimate the errors. There are two different ways to estimate retrieval errors:

Error propagation: If we know the primary uncertainties (measurement noise, parameter uncertainties, etc) or have good estimates on them, we can propagate them through the system and estimate the retrieval errors in the **x**-space. This type of error estimation can be performed without having any real measurement available: the knowledge of the instrument and retrieval characteristics is sufficient. This method is standard for pre-flight studies of future space-instrumentation. Von Clarmann (2006) has suggested to call these error estimates "ex ante" estimates, because they can be made before the measurement is performed.

Statistical assessment: With a sufficient number of measurements along with co-incident independent measurements available, measurement errors can be assessed by doing statistics on the mean differences, standard deviation of differences etc. Von Clarmann (2006) has suggested to call these error estimates "ex post" estimates, because they can be made only after the retrievals have been made available.

1.3.1.5 Error Propagation

The term refers to the error estimation for indirect measurements, i.e. error estimation of functions of measurements. Knowing the errors and the error correlation of a multi-dimensional argument, represented by its covariance matrix (e.g. S_a), the error covariance matrix of any linear operation $\mathbf{b} = \mathbf{Ma}$ is calculated as $\mathbf{S_b} = \mathbf{M S_a M^T}$. In case of non-linear function, one usually takes for M its linearization.

Example 1: Averaging of measurements with random errors.
Suppose we have 3 uncorrelated measurements:

$$\mathbf{x} = (\mathbf{x_1}, \mathbf{x_2}, \mathbf{x_3})$$

$$r_{12} = 0; \; r_{13} = 0; \; r_{23} = 0$$

Suppose further that all three measurements have same standard deviations:

$$\sigma = \sigma_1 = \sigma_2 = \sigma_3$$

The function in question is "averaging", i.e. the matrix of corresponding linear operator is

$$M = \left(\frac{1}{3}; \frac{1}{3}; \frac{1}{3} \right)$$
.

i.e. errors of all arguments are of the same expected size. Then the error of the mean is estimated as

$$\sigma_{mean} = \sqrt{ \left(\frac{1}{3} \; \frac{1}{3} \; \frac{1}{3} \right) \begin{pmatrix} \sigma^2 & 0 & 0 \\ 0 & \sigma^2 & 0 \\ 0 & 0 & \sigma^2 \end{pmatrix} \begin{pmatrix} \frac{1}{3} \\ \frac{1}{3} \\ \frac{1}{3} \end{pmatrix} } = \frac{\sigma}{\sqrt{3}}$$

Example 2: Averaging of measurements with systematic errors.
Again, let

$$\mathbf{x} = (\mathbf{x_1}, \mathbf{x_2}, \mathbf{x_3})$$

be three measurement, that are correlated this time:

$$r_{12} = 1; \; r_{13} = 1; \; r_{23} = 1$$

Suppose further that all three measurements have same standard deviations:

$$\sigma = \sigma_1 = \sigma_2 = \sigma_3$$

i.e. again errors of all arguments are of the same expected size, then
The function is "averaging", i.e. the matrix of corresponding linear operator is

$$M = \left(\frac{1}{3}; \frac{1}{3}; \frac{1}{3} \right)$$
.

Then the corresponding error can be estimated as

$$\sigma_{mean} = \sqrt{ \left(\frac{1}{3} \; \frac{1}{3} \; \frac{1}{3} \right) \begin{pmatrix} \sigma^2 & \sigma^2 & \sigma^2 \\ \sigma^2 & \sigma^2 & \sigma^2 \\ \sigma^2 & \sigma^2 & \sigma^2 \end{pmatrix} \begin{pmatrix} \frac{1}{3} \\ \frac{1}{3} \\ \frac{1}{3} \end{pmatrix} } = \sigma$$

1.3.1.6   Error Predictors

We call preliminary (ex ante) estimates of the errors "error predictors". We suggest the following notation: **S** is the covariance matrix, the first index is the space, the second index is the error source, see also (C. D. Rodgers 2000)

1.3.1.6.1   *Parasite Error*
These errors are not easily predictable. At best, implausible values can be detected.

1.3.1.6.2   *Noise Error*
The noise error is defined as

$$S_{\mathbf{x},noise} = \mathbf{G}S_{\mathbf{y},noise}\mathbf{G}^T$$

Eq. 1.3

where **G** is the so-called gain function defined as

$$\mathbf{G} = \frac{\partial \mathbf{x}}{\partial \mathbf{y}}$$

Eq. 1.4

A parameter error with respect to the ith parameter is defined as:

$$S_{\mathbf{x},parameter} = \mathbf{G}S_{\mathbf{y},parameter}\mathbf{G}^T$$

Eq. 1.5

with

$$S_{\mathbf{y},parameter} = \mathbf{K}_{\mathbf{u}_i}S_{\mathbf{u}_i}\mathbf{K}_{\mathbf{u}_i}^T$$

Eq. 1.6

where

$$\mathbf{K}_{\mathbf{u}_i} = \frac{\partial \mathbf{y}}{\partial \mathbf{u}_i}$$

Eq. 1.7

1.3.1.6.3   Model Error

Often limitations in computation power force one to use a model inferior to the best available model. In this case, the error caused by the use of a sub-optimal model can be estimated as follows:

$$\Delta_{\mathbf{y},model} = f_{as\ good\ as\ possible}(\mathbf{x},\mathbf{u}) - f_{as\ used\ in\ retrieval}(\mathbf{x},\mathbf{u})$$

Eq. 1.8

so that

$$\Delta_{\mathbf{x},model} = G\Delta_{\mathbf{y},model}$$

Eq. 1.9

and

$$S_{\mathbf{x},model} = \Delta_{\mathbf{x},model}\Delta_{\mathbf{x},model}^T$$

Eq. 1.10

1.3.1.6.4   Smoothing Error

While, as discussed in section 1.3.1.1, we are not convinced that the smoothing error with respect to the true atmosphere is a meaningful and useful quantity, the smoothing error difference between two retrievals is definitely useful. It is needed to compare instruments of

different altitude resolution. For this purpose we need the sensitivity of the retrieval with respect to the true atmospheric state (Rodgers, 2000), represented by the averaging kernel matrix $\mathbf{A}$.

Recall that $\mathbf{A}$ is defined as

$$\mathbf{A} = \frac{\partial \hat{\mathbf{x}}}{\mathbf{x}} = \mathbf{GK}$$

Eq. 1.11

where $\mathbf{G}$ is the gain function and

$$\mathbf{K} = \frac{\partial \mathbf{y}}{\partial \mathbf{x}}$$

Eq. 1.12

The smoothing error difference between two datasets $\mathbf{a}$ and $\mathbf{b}$ is then given by

$$(A_a - A_b)\mathbf{S}_{comparison}(A_a - A_b)^T$$

Eq. 1.13

where $S_{comparison}$ is the climatological covariance matrix of the comparison ensemble. Rigorous theory requires that $S_{comparison}$ characterizes exactly the climatology of the geolocation (within coincidence criteria) of intersect of measurement geolocations $\mathbf{a}$ and $\mathbf{b}$. This means that it is not allowed to apply Eq 10.48 of (Rodgers, 2000) just to one of the datasets to transform it to the a priori of the other.

1.3.1.6.5 *Total Predicted Error*

We assume that the errors of different sources are uncorrelated among each other. Then the total error at a given resolution is

$$\mathbf{S}_{\mathbf{x},total} = \mathbf{S}_{\mathbf{x},noise} + \sum_i \mathbf{S}_{\mathbf{x},parameter_i} + \mathbf{S}_{\mathbf{x},model}$$

Eq. 1.14

1.3.1.7 **Error Evidences**

We call the ex post (a posterior) estimates of the errors "error evidences". Since we do not know the true state of the atmosphere, we need reference measurements. For the moment we assume perfect coincidences of the measurements under consideration and the reference measurement, i.e. the reference measurement measures exactly the same air parcel at the same time at the same spatial resolution. We further assume that the reference measurement is debiased and perfectly characterized in terms of precision:

$$bias = <\hat{\mathbf{x}} - \hat{\mathbf{x}}_{ref}>$$

Eq. 1.15

$$\mathbf{S}_{\mathbf{x},random} = \frac{(\hat{\mathbf{x}} - \hat{\mathbf{x}}_{ref} - bias)^T(\hat{\mathbf{x}} - \hat{\mathbf{x}}_{ref} - bias)}{n-1} - \mathbf{S}_{\mathbf{x}_{ref},random}$$

Eq. 1.16

Further details (significance of bias estimate, alternate options etc.) are discussed in teasing detail in (von Clarmann, 2006). It should be pointed that further complication may arise from the fact that reference measurements might have sounded another part of the atmosphere at another time. Problems arising from the fact that measurements may have different a priori knowledge is discussed in "Validation" (section 1.3.2).

1.3.2   Validation and comparison

Validation means to (von Clarmann, 2006)
(a) determine the bias between the instrument under assessment and a reference instrument
(b) verify the predicted precision by analysis of the debiased standard deviation between the measurements under assessment and the reference measurement.
(c) more advanced: assess the long-term stability, i.e. to falsify the hypothesis of a drift of the differences between the measurements under assessment and the reference measurement.

All three operations involve calculation of differences between two measurements. These differences are only meaningful if

- both retrievals contain the same a priori information. Some retrievals use a priori information $\mathbf{x_a}$ to constrain the retrievals. If profiles contain different a priori informations, meaningful comparison of retrievals requires to transform the retrievals to the same a priori information: (Rodgers, 2000) Eq. 10.48 or

$$\hat{\mathbf{x}}_{transformed} = \hat{\mathbf{x}} + (\mathbf{I} - \mathbf{A})(\mathbf{x}_{a,new} - \mathbf{x}_{a,old})$$

<div align="right">Eq. 1.17</div>

where $\mathbf{I}$ is unity;

- the a priori information must be the climatology (expectation value and covariance) of the geolocation of the intersect of both instruments used;

- the same air mass is observed. If this is not the case, there will be a "coincidence error". This can be estimated and considered when the significance of differences between the two data sets under assessment is analysed;

- the altitude resolution (or, in more general terms) spatial resolution is the same. If this is not the case, the "smoothing error difference" can be estimated and considered when the significance of differences between the two data sets under assessment is analysed.

    If the contrast in resolution between two measurements $\hat{\mathbf{x}}^{fine}$ and $\hat{\mathbf{x}}^{coarse}$ is large, the following approximation is valid (Rodgers and Connor, 2003)

$$\hat{\mathbf{x}}_{smoothed}^{fine} = \mathbf{A}_{coarse}\hat{\mathbf{x}}^{fine} + (\mathbf{I} - \mathbf{A})\mathbf{x}_{a\ priori}^{coarse}$$

<div align="right">Eq. 1.18</div>

where $\hat{\mathbf{x}}_{smoothed}^{fine}$ is the degraded well resolved measurement, $\mathbf{A}_{coarse}$ is the averaging kernel of the poorly resolved measurement, I is unity, $\mathbf{x}_{a\ priori}^{coarse}$ is the a priori information used for the poorly resolved retrieval. The rationale behind this transformation is to remove differences between the measurements which can be explained by different altitude resolutions. The remaining differences thus are substantial. The same transformation has, of course, to be applied to the errors:

$$\mathbf{S}_{\mathbf{x}_{smoothed}^{fine}} = \mathbf{A}_{coarse}\mathbf{S}_{\mathbf{x}^{fine}}\mathbf{A}_{coarse}^{T}$$

Eq. 1.19

In case of long-term stability validation the comparability of measurements is less critical because one can hope that inconsistencies in first order cancel out when the double differences are calculated.

1.3.3   The real world

A detailed questionnaire about Data and Error Characterization of the data (profiles and total columns) retrieved from remotely sensed measurement was filled out by all the partners of the consortium, as well as by some third parties. Altogether, 11 processors were analysed: 8 processors of limb viewing instruments data, 2 processors of nadir data and 1 of stellar occultation. This allowed sketching a state of the art of Data and Error Characterization, which is outlined in this chapter. It should be kept in mind that the questionnaire was designed targeting the limb viewing geometry instruments. So, the parts of it dealing with retrieval success are not quite well adapted for nadir or especially stellar occultation retrieval algorithms. However, everything concerning the error characterization does apply.

1.3.4   Review of existing practices in error characterization

This section will provide some evidences that indeed the error and data characterization crucially miss a common terminology. The most striking example is the interpreting of the terms "parametric error" and "systematic error". To begin with, 3 partners just suppose not having parametric errors at all. Listed below are the factors, named by remaining 8 partners as "parametric errors" affecting their retrievals.

- instrument pointing
- calibration gain
- temperature
- tangent pressure
- strength, position and width of infrared emission lines
- assumed column above the highest retrieved ozone value
- LTE assumption
- interfering species (H_2O, CO_2, N_2O_5, HCN)
- surface albedo
- clouds: tropospheric, polar stratospheric, polar mesospheric
- stratospheric aerosols

- width of apodised instrument line shape
- uncertainty in gaseous continua
- horizontally homogeneous atmosphere assumption

Difference of interpretations aside, the representation of this error is quite poor in the consortium: only stellar occultation processors characterize their parameter errors by their full covariance matrices. But as understanding of what is the parameter error varies a lot among the consortium, the best way to resume would be to say that these processors fully characterize (for all measurement or for selected measurements) only part of its parameter errors. Five processors characterize their parametric errors in a simplified way for selected measurement, and three processors, having the parameter errors, do not have parameter error characterization at all.

Mapping of measurement noise is treated as following. Four processors provide or can provide the whole S_{x_noise} matrix. Two more processors provide this matrix only for representative atmospheric conditions or selected measurements. Seven processors out of 11 provide (or designed to provide, hence can easily provide) only the diagonal elements of the matrix S_{x_noise}, that is, the variances. Only one processor does provide neither variance nor covariance information.

Some processors retrieve other variables jointly with ozone (8 out of 11). For five among them, the joint fit covariance matrix is available for the complete vector of unknowns. Three more processors (including the one performing 2D retrieval) store only the diagonal block related to ozone.

Four processors out of 11 have the details about their calculation of S_{x_noise} published in per-review journals.

1.4   Review of existing ways to characterize the data

Differences in instrument and retrieval processors designs constrain the choice of the retrieval grid, and it turns out that all possible choices - altitude / pressure grid, independent retrieval grid or grid defined by the tangent altitudes, common grid for all measurements or not - are implemented through the consortium. When comparing different instruments, the standard way to proceed is to transform the compared profiles on a common grid, the choice of which is dictated by the validation approach in mind. The corresponding diagnostic data (averaging kernels, covariance matrices) should then be propagated together with the profiles. In the processors in which it is done (3 processors out of 11 analyzed), the propagation of covariance matrices does follow the concept introduced in section 1.3.1.5, namely for linear operation $b = Ma$, where M is the interpolation matrix from one grid to another, the corresponding covariance matrix becomes $S_b = MS_aM^T$.

Averaging Kernels
Recall that the averaging kernels matrix of a retrieval is defined as $A = GK$ where G is the gain function and

$$\mathbf{K} = \frac{\partial \mathbf{y}}{\partial \mathbf{x}}$$

Eq. 1.20

Averaging kernel can be thought of as a measure of how and where the retrieval is sensitive to changes in the "true" state vector. It seems to be a common understanding of their importance because among the consortium, there is a clear effort to provide (profile or total column) vertical averaging kernels: half of the processors provide them for each retrieval, another half have them for sample retrievals. The situation is quite different when it comes to the horizontal averaging kernels: no processor provides them for each retrieval, only one processor actually provides them for sample retrievals, only one more processor is designed so that it can easily provide them, and only one more processor is designed so that they can be provided by a conceptually clear workaround. The reason is that in most processors, the atmosphere is assumed to be locally homogeneous in the horizontal domain, i.e. no horizontal variability is considered during the analysis of one limb scan. The processor that does provide them is the one performing 2D-retrieval, the processor which can easily provide them is the one retrieving horizontal gradients from measurements, and the processor proposing a workaround for providing horizontal averaging kernels is the one that treats the horizontal variability of the atmosphere by assuming it being locally spherically symmetric.

The estimation of vertical resolution is done and provided only in 2 processors out of 8 for which it is applicable.

Data quality report: qualification of the data, data flagging, quality degrading factors.
Among the consortium, there is a diversity of ways to report the data quality. Data can be declared not meaningful, corrupted, simply unphysical, unphysical but mathematical. In plus, the data retrieved among the consortium, can be degraded by clouds, ice/snow and Southern Atlantic anomaly.

For non-meaningful data, 6 processors out of 11 include all the data in the files. One processor includes the data only on valid altitude/pressure range. The 4 remaining processors use NaN entries or equivalent, for data outside a valid altitude/pressure range.

As to the corrupted data, 3 processors report all data. For 5 processors, data considered corrupted are reported but there exist easy to handle indicators to sort them out. Two processors overwrite such data by a flag (zero or large negative value or NaN entry). Finally, only one processor does not report corrupted data at all.

Negative values are reported as they are by 6 processors (i.e. despite that the data are unphysical, they are taken into account being mathematically significant). One processor overwrites negative values by a flag. Two processors set negative values to 0 or close to 0 (it should however be pointed that such a maneuver corrupts the subsequent calculations of the means).

The flags can mark the data below the lowermost tangent altitude (case of 2 processors), data where clouds interfere (4 processors), number of macro/micro iterations too big (1 processor), invalid data (2 processors), quality flag (set to 0 or 1, holds for 1 processor). The most used flag is convergence reached – 7 the processors have it their standard product.

Auxiliary data

In all processors, the data come along with other data characterizing the atmosphere and/or measurement conditions. Eight processors provide the temperature estimation. Five processors, out of 7 retrieving on altitude grids, provide pressure estimation. Two processors, out of 3 retrieving on pressure gird, provide altitude estimation.

1.4.1 Review of diagnostics in use (success of the retrieval)

The following quantities are used by partners to characterize the success of their retrievals:
- χ^2 (normalized)
- residuals (rms)
- number of iterations
- condition number
- χ^2_x
- χ^2_y
- number of degrees of freedom for each retrieval parameter
- convergence flag for each retrieval parameter
- detailed plots of convergence sequence
- evaluation of cost function
- DFS
- Marquardt parameter
- retrieved pointing.

The χ^2 statistics is the most "popular" and is a part of the standard product of 6 processors. The residuals (rms) are stored with data of 5 processors. The number of iterations is part of standard product of 2 processors and is part of operational (internal, but publicly unavailable) product of one more processor. Only 3 processors use convergence quality flag based on more than three of diagnostics above: one of those three processors uses 9 diagnostics above, the two others – 4 diagnostics each. All three of them provide these diagnostics as part of their official data. However, all analyzed processors have a number of "auxiliary" diagnostics, used in retrieval but not provided with the standard product.

It is worth to point out that, unlike for the vertical averaging kernel matrix, its trace, which reflects the number of vertical degree of freedom and is an important diagnostic of retrieval success, is provided by only 2 processors out of 11.

1.4.2 Recipes proposed

Often the application of the pure theory as described in Chapter 1.2.2 is not easily feasible. Thus, we propose some recipes how to characterize retrievals when some key quantities are not available.

The approach is simple and follow the principle "what the most of us can provide with reasonable effort". Based on this,
1) vertical averaging kernels should be provided with the data, or at least the corresponding diagonal (the number of degree of freedom). At least an estimate of the altitude resolution should be provided.

2) diagonal elements of the matrix $\mathbf{S_{x\_noise}}$, that is, the variances should be provided

3) there should be a data quality flag, based on χ^2 statistics and rms of the difference between the measurement and the best fit.

4) all the data (corrupted, not meaningful etc) should be included in the file, together with relevant flagging

5) temperature and pressure/altitude should be provided together with profiles.

6) negative values should be just reported, not replaced by zeros or flags

2   Total Ozone ECV retrieval algorithms

2.1   GODFIT (BIRA-IASB)

Within the Ozone_cci project, the baseline algorithm for total ozone retrieval from backscatter UV sensors is the GOME-type direct-fitting (GODFIT) algorithm jointly developed at BIRA-IASB, DLR-IMF and RT-Solutions for implementation in version 5 of the GOME Data Processor (GDP) operational system. In contrast to previous versions of the GDP which were based on the DOAS method, GODFIT uses a least-squares fitting inverse algorithm including direct multi-spectral radiative transfer simulation of earthshine radiances and Jacobians with respect to total ozone, albedo closure and other ancillary fitting parameters. The algorithm has been described in details in the GDP5 Algorithm Theoretical Basis Document (Spurr et al. 2011). More details about description below can also be found in (C. Lerotet al. 2010), (C. Lerot et al., 2014) and (Van Roozendael et al., 2012).

2.1.1   Overview of the algorithm

The direct fitting algorithm employs a classical inverse method of iterative least squares minimization which is based on a linearized forward model, that is, a multiple-scatter radiative transfer (RT) simulation of earthshine radiances and associated weighting functions (Jacobians) with respect to state vector elements. The latter are the total ozone column and several ancillary parameters including albedo closure coefficients, a temperature shift, amplitudes for Ring and undersampling corrections, and a wavelength registration shift. On-the-fly RT calculations are done using the LIDORT discrete ordinate model (R. Spurr, LIDORT and VLIDORT: Linearized pseudo-spherical scalar and vector discrete ordinate radiative transfer models for use in remote sensing retrieval problems 2008). The performance of the radiative transfer computations has been significantly enhanced with the development of a new scheme based on the application of Principal Components Analysis (PCA) to the optical property data sets (Spurr, Natraj and Lerot, et al. 2013). Alternatively, the simulated radiances and Jacobians can be extracted from pre-computed tables in order to further accelerate the retrievals (see section 2.1.1.5). This facilitates greatly the treatment of large amount of data provided by sensors with a very high spatial resolution such as OMI aboard the AURA platform and the future Sentinel-4 and -5(p) instruments.

The flowchart in Figure 2.1 gives an overview of the algorithm. It is straightforward, with one major decision point. Following the initial reading of satellite radiance and irradiance data, and the input of auxiliary data (topography fields, optional temperature profiles, fractional cloud

cover and cloud-top-height), the iteration counter is set (n=0), and an initial guess is made for the state vector (total ozone amount, temperature shift, closure coefficients, etc.). A unique ozone profile $P(n)$ is then constructed from the total column estimate $C(n)$, using a 1-1 column-profile map based on column-classified ozone profile climatology. For this, we use the climatological database developed for the TOMS Version 8 total ozone retrieval (Bhartia 2003). Next, pressure, temperature and height profiles are constructed; this is where the current value of the temperature shift $S(n)$ is applied. Spectral reference data are also prepared for the fitting window (trace gas cross-sections, Rayleigh cross-sections and depolarization ratios).

The algorithm then enters the forward model step, in which optical properties are created and the LIDORT model called to deliver top-of-atmosphere (TOA) radiances $I(n)$, and the associated ozone column, albedo, T-shift and other weighting functions $K(n)$ at each iteration step n. These simulated quantities are then corrected for the molecular Ring effect. Next, the inversion module yields a new guess for the ozone column and ancillary state vector parameters. The iteration stops when suitable convergence criteria have been satisfied, or when the maximum number of iterations has been reached (in which case, there is no established convergence and final product). The ozone total column and other parameter errors are computed directly from the inverse variance-covariance matrix.

When the simulated spectra are extracted from a lookup table (LUT) instead of being computed online, the inversion procedure is further simplified. The optical properties do not have to be computed and the calls to the RT model LIDORT are replaced by interpolation procedures through the LUT using directly the state vector variables as input in addition to the geolocation parameters. The radiance LUT has obviously been pre-computed using the same forward model as the online scheme in order to have full consistency between the two approaches (see section 2.1.1.5).
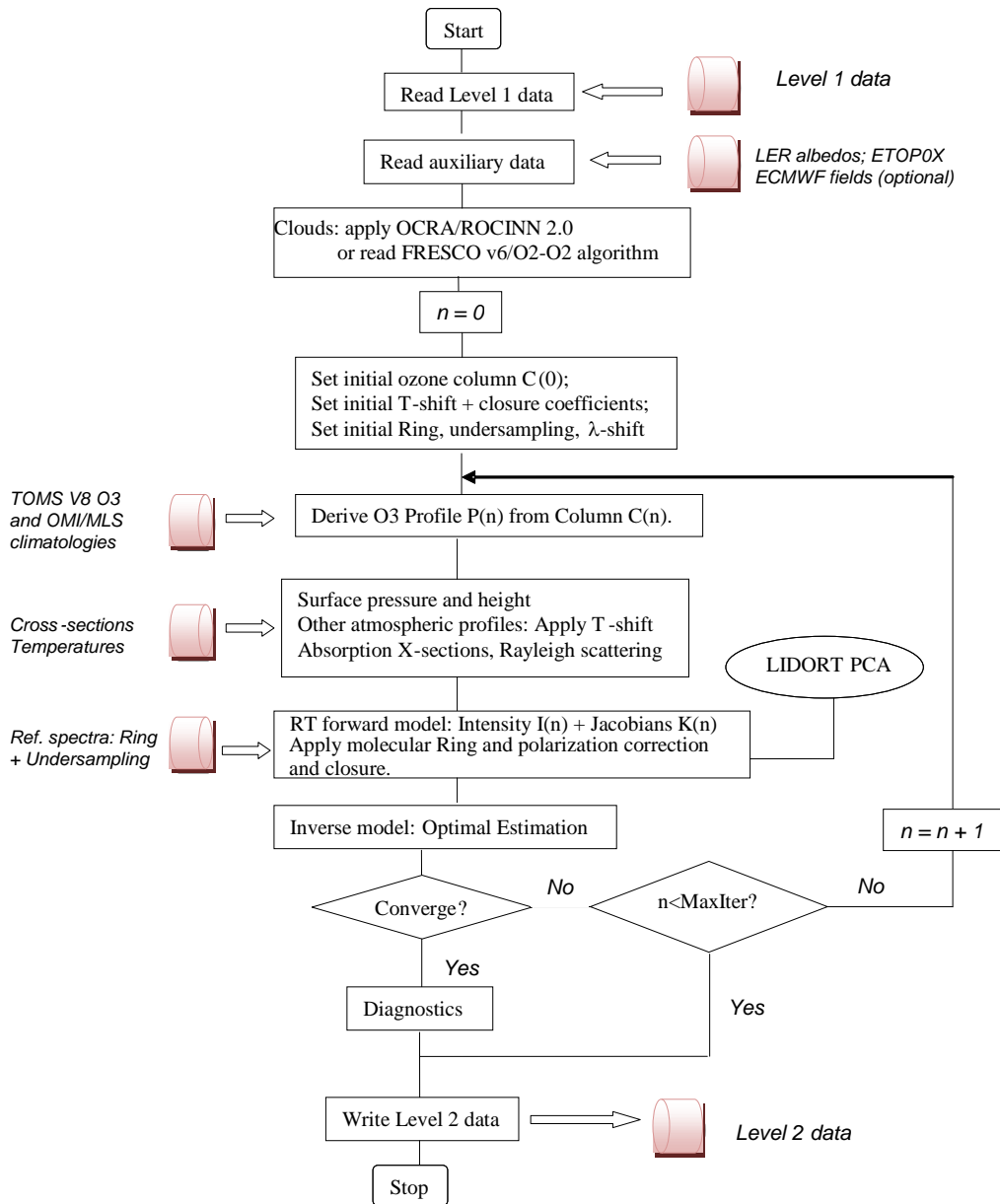
Figure 2.1: Flow Diagram of the GOME-type direct fitting retrieval algorithm

2.1.1.1 Forward model

Simulation of earthshine radiances and retrieval-parameter Jacobians is done using the multi-layer multiple scattering radiative transfer code LIDORT (R. Spurr, LIDORT and VLIDORT: Linearized pseudo-spherical scalar and vector discrete ordinate radiative transfer models for use in remote sensing retrieval problems 2008). LIDORT generates analytic Jacobians for atmospheric and/or surface properties (a.o. Jacobians for total ozone, surface albedo and temperature shift). LIDORT solves the radiative transfer equation in each layer using the discrete-ordinate method (Chandrasekhar 1960), (Stamnes, et al. 1988); boundary conditions (surface reflectance, level continuity, direct incoming sunlight at top-of-atmosphere) are applied to generate the whole-atmosphere field at discrete ordinates; source function integration

is then used to generate solutions at any desired viewing geometry and output level. The entire discrete ordinate RT solution is analytically differentiable with respect to any atmospheric and/or surface parameter used to construct optical properties (R. Spurr, Simultaneous derivation of intensities and weighting functions in a general pseudo-spherical discrete ordinate radiative transfer treatment 2002), and this allows weighting functions to be determined accurately with very little additional numerical computation.

In addition to the usual pseudo-spherical (P-S) approximation (solar beam attenuation treated for a curved atmosphere) LIDORT also has an outgoing sphericity correction, in which both solar and viewing angles are allowed to vary along the line-of-sight (LOS) path treated for a spherical-shell atmosphere. This approach gives sufficient accuracy[2] for off-nadir viewing geometries (maximum 60°) encountered with polar orbiting sun-synchronous sensors.

A new accelerated-performance scheme for the radiative transfer computation has been implemented within GODFIT. This scheme is based on the application of Principal Component Analysis (PCA) to optical property data sets used for RT simulation – most of the variance in the mean-removed optical data is contained in the first and most important empirical orthogonal functions (EOFs). Thus, full multiple-scattering (MS) computations with LIDORT are done only for the mean profile and the first few EOF optical profiles. These LIDORT MS results are then compared with MS radiances from a 2-stream (2S) RT code (Spurr und Natraj, A linearized two-stream radiative transfer code for fast approximation of multiple-scatter fields 2011), and a second-order central difference scheme based on these LIDORT/2S difference and on the data Principal Components is then used to provide correction factors to the MS field at every wavelength. Thus it is only necessary to compute the MS radiances at every wavelength using the much faster 2S code.

LIDORT is a scalar code and therefore polarization is neglected in the RT modeling. Ideally, a vector code such as VLIDORT should be used in the forward model. However, to minimize the computational burden with GODFIT, polarization correction factors are applied to simulated scalar radiances. These factors are extracted from a lookup table of VLIDORT-LIDORT intensity relative differences. This LUT provides correction factors classified according to ranges of the solar zenith, viewing zenith, and relative azimuth angles (from 20 to 85 degrees, 0 to 55 degrees and 0 to 180 degrees respectively), surface altitude (from 0 to 15 km), ground albedo (from 0 to 1) and the total ozone column (from 125 to 575 DU).

2.1.1.2 Lookup Atmospheric profiles and the T-shift procedure

In a multilayer atmosphere, the forward model requires the specification of a complete ozone profile. In GODFIT, the ozone profile is parameterized by total column, time and latitude. The use of total column as a proxy for the ozone profile was recognized a number of years ago and column-classified ozone profile climatologies were created for the TOMS Version 7 (Wellemeyer, et al. 1997), and Version 8 (V8) retrieval algorithms (Bhartia 2003). The same mapping is used for GODFIT. This climatology neglects the longitudinal variations of tropospheric ozone. To improve the representativeness of the *a priori* profiles, it is combined with the OMI/MLS tropospheric ozone column climatology (Ziemke et al., 2011).

---

[2] In this context," accuracy" is the total error of the retrieval.

Since ozone absorption in the Huggins bands is highly sensitive to temperature, temperature profiles are not only required for hydrostatic balance but also for the determination of ozone cross sections. In GODFIT, a-priori temperature profiles are taken from the monthly zonal temperature climatology supplied with the TOMS Version 8 ozone profiles (Bhartia 2003). In addition, a temperature shift adjustment is being used to improve total ozone accuracy[3] and better reflect the dependence of the ozone absorption signature on temperature at the scale of satellite pixels (Van Roozendael et al., 2012).

2.1.1.3 Surface and cloud treatment

Lower boundary reflection properties must be specified as an input for the forward model. By default, one assumes a Lambertian surface characterized by a total albedo *L*. Most ozone being above the tropopause, clouds can be treated as a first-order correction to the basic ozone retrieval using the independent pixel approximation (IPA). TOA radiance in a partially cloudy scenario is simulated as a linear combination of radiances from clear and fully cloudy scenes, weighted by the effective cloud fractional cover f_c assuming clouds as Lambertian reflecting boundary surfaces. Alternatively, the observed scene can be treated as a single effective surface, located at an altitude resulting from the cloud fraction weighted mean of the ground and cloud altitudes (Coldewey-Egbers et al., 2005). The effective surface albedo is retrieved simultaneously to the total ozone column using the internal closure mode of GODFIT. We found that this approach minimizes the impact of cloud contamination on the retrieved ozone columns, especially for high clouds and it has been consequently adopted in the current version of the algorithm. By default, cloud optical properties (cloud fraction, cloud top albedo and height) come from the FRESCOv6 algorithm (Koelemeijer et al., 2003; Wang et al., 2008) for GOME, SCIAMACHY and GOME-2 and from the O2-O2 cloud product (Acarreta et al., 2004) for OMI. Interfaces also allow for application of the OCRA/ROCINN algorithm Version 2.0 (Loyola et al., 2010).

2.1.1.4 Albedo and other forward model closure terms

For internal closure, tropospheric aerosol scattering and absorption and surface reflectivity are brought together in an albedo closure term that is fitted internally, in the sense that coupling between surface and atmosphere is treated properly in a full multiple scattering context. The code thus determines an effective wavelength-dependent albedo in a molecular atmosphere. Assuming that surface albedo **R** is a quadratic or cubic polynomial function, we write:

$$R(\lambda) = \gamma_0 + \sum_{m=1}^{M} \gamma_m (1 - \lambda/\lambda_0)^m$$

Eq. 2.0

We assume first guess values $\gamma_m = 0$ for $m > 0$, and an initial value for γ_0 is taken from a suitable database.

---

[3] I.e. to diminish the total error of the retrieval.

In order to complete the forward model process, additional effects must be taken into account before simulated intensities can be compared with Level 1b measurements in the inverse model. In particular, the Ring effect which shows up as small-amplitude distortions in earthshine and sky spectra due to the effect of inelastic rotational Raman scattering by air molecules (Grainger und Ring 1962) must be corrected for. To this aim, we use a semi-empirical revisited semi-empirical formulation including tabulated effective air mass factors and reproducing closely filling-in factors calculated with the LIDORT-RRS radiative transfer code (Lerot et al., 2014).

We then simulate sun-normalized radiances at wavelengths specified by the solar irradiance spectrum supplied with every orbit. There is a wavelength registration mismatch between irradiance and radiance spectra, arising mainly from the solar spectrum Doppler shift; this mismatch varies across an orbit due to changes in the instrument temperature. To correct for this, an earthshine spectrum shift is fitted as part of the retrieval procedure, and this shift value is then an element in the state vector of retrieval parameters. In general, the retrieved spectrum shift value is around 0.008 nm, in line with a Doppler shift. Re-sampling is always done by cubic-spline interpolation.

2.1.1.5   Lookup tables of LIDORT sun-normalized radiances

The goal of the lookup table approach is to replace the online radiative transfer calculation by an interpolation of precalculated radiances. Therefore, we construct a multi-dimensional lookup table of radiances as a function of all varying parameters that enter the LIDORT simulation: the fitted parameters (total ozone column and the ancillary fitting parameters scene albedo and temperature shift), angles describing the observation geometry, surface pressure, as well as latitude and time of year, by which we select the appropriate profile shapes from the TOMSv8 database (see section 2.1.1.2.). The tabulated radiances are then calculated for a fixed wavelength grid spanning the 325nm-335nm range at 3 times the instrument sampling rate, using cross sections convolved with the instrument's slit function.

The forward model calculation for a set of parameter values now becomes an interpolation of the radiances at surrounding grid points. For the total ozone column and solar zenith angle, we use quadratic interpolation through 3 surrounding grid points. For the other dimensions of the table, linear interpolation is sufficient. This results in an interpolated radiance as a function of the lookup table's wavelength grid, which is then resampled onto the wavelength grid of the observed spectrum using cubic spline interpolation. The derivative of this interpolation procedure produces the needed Jacobians.

In order to keep the interpolation procedure simple and efficient, the LUT uses a wavelength-independent scene albedo. Within the inversion procedure, only a wavelength-independent albedo is fitted, and the possible wavelength dependence of the spectrally-smooth variation of the measured radiance is taken into account via the fit of a polynomial of which the constant term is neglected.

In order for the lookup table approach to be faster than the online algorithm, frequent hard disk access must be avoided. Because all forward model parameters, except for the time of year, vary rapidly within a single orbit file, this restriction translates into the requirement that the radiances for the full range of those parameters fit in memory. This puts a limit on the density of the table's parameter grid, and some experimentation is necessary to obtain a grid which fits in memory and produces accurate interpolation results over the whole parameter space. To save space, the parameter grid does not include a longitudinal dimension. The precalculated

radiances are therefore based solely on the TOMSv8 profile database, which has no longitudinal dependence, instead of the combination of TOMSv8 and the tropospheric climatology OMI/MLS, which would be used in the online approach (section 2.1.1.2). After the retrieval, we use the averaging kernels (see section 2.1.1.9.) and the difference between the profile used for the retrieval (TOMSv8) and another more accurate profile to apply a correction to the retrieved total column. Using these techniques, we have managed to construct a lookup table which reproduces the retrieved columns of the online algorithm with an accuracy better than 1%, and a tenfold performance improvement.

2.1.1.6   Inversion scheme

GODFIT is a direct fitting algorithm, using iterative non-linear least squares minimization. In the scientific prototype version mostly used for Ozone_cci work, the optimal estimation inverse method is being used with loose a priori regularization on the state vector elements. The optimal estimation method is well known (Rodgers, 2000); we minimize the quadratic functional cost function:

$$\chi^2 = (y_{meas} - f(x))^T S_y^{-1} (y_{meas} - f(x)) + (x - x_a)^T S_a^{-1} (x - x_a)$$

Eq. 2.1

Here, we have the measurement vector of TOA radiances y_{meas}, the state vector x, the forward model simulations $f(x)$, and the error covariance matrix S_y. x_a is the a priori state vector, with S_a the corresponding covariance matrix. The inversion proceeds iteratively via a series of linearizations about the atmospheric state at each iteration step:

$$x_{i+1} = x_a + \mathbf{D}_y \left[y_{meas} - f(x_i) - \mathbf{K}_i (x_i - x_a) \right]$$

Eq. 2.2

Where:

$$\mathbf{D}_y = \mathbf{S}_{i+1} \mathbf{K}_i^{\mathbf{T}} \mathbf{S}_y^{-1} \quad \textbf{and} \quad \mathbf{S}_{i+1} = \left(\mathbf{K}_i^{\mathbf{T}} \mathbf{S}_y^{-1} \mathbf{K}_i + \mathbf{S}_a^{-1} \right)^{-1}$$

Eq. 2.3

$K_i = df(x_i)/dx_i$ is the matrix of Jacobians, $\mathbf{D}_y$ is the matrix of contribution functions, and $\mathbf{S}_{i+1}$ is the solution covariance matrix. The latter is the main diagnostic output. The iteration stops when one or more convergence criteria are met. The computation proceeds efficiently with an SVD (singular value decomposition) on the scaled matrix Jacobians; see for example (Van Oss, Voors and Spurr, Ozone Profile Algorithm 2002). Since the total ozone inverse problem is not ill-posed, the regularization is only present to ensure numerical stability. The a priori constraints are deliberately made very loose, so that the precision is not compromised in any serious way by a priori smoothing. The a priori vector is taken to be the initial state vector.

2.1.1.7   State vector and inverse model settings

There are typically 7 to 8 elements in the retrieval state vector, listed in Table 2.1, along with their initial value settings. Aside from total ozone, the algorithm fits the temperature-profile shift parameter, 3 polynomial coefficients for internal albedo closure, 2 amplitudes for the semi-empirical molecular Ring correction and the (optional) undersampling correction and an earthshine spectrum wavelength shift.

Table 2.1: Summary of fitting parameters for direct fitting total ozone algorithm

State Vector Element Type	# of parameters	Initial Value
Total ozone (unit: [DU])	1	Previous-pixel
Polynomial Coefficient (Internal Closure)	3	R_{335}, 0.0, 0.0
T-shift (unit: [K])	1	0.0
Ring Fraunhofer	1	1.0
Earthshine Shift (unit: [nm])	1	0.008
Undersampling	1	0.0

The total ozone first guess is taken from the previous pixel value. If this value is not available for some reason, the initial total ozone column is taken from a zonal averaged climatology based on TOMS data (Stolarski and Frith, 2006). For closure, the initial value R_{335} is extracted from the surface albedo database at 335 nm as described in section 2.4; other albedo parameters are initialized to zero. Initial values of the under-sampling and T-shift parameters are all zero, while the earthshine shift is initialized to 0.008 corresponding to the average Doppler shift due to the platform speed of around 7000 m/s.

2.1.1.8   Soft-calibration of level-1 reflectances

Although a common group of retrieval settings are applied consistently to all three level-1 data sets from GOME, SCIAMACHY and GOME-2, systematic differences between the individual total ozone data sets remain. These originate from systematic radiometric errors and degradation effects affecting the measured level-1 reflectances. To deal with these patterns and enhance the inter-sensor consistency, a soft-calibration scheme has been developed. This procedure relies on comparisons of measured level-1 reflectances to simulated values in the spectral interval 325-335 nm, the simulations being performed with the same forward model as that used for the retrievals. In particular, ozone columns from Brewer observations at a limited number of European stations have been used as an external reference to realize these simulations. The systematic comparison of the level-1 and simulated reflectances for all satellite observations co-located with the selected stations allows to identify and characterize possible (broad-band or high-frequency) artifacts in the measurements. Based on this analysis, lookup tables (LUTs) of spectral correction factors have been constructed for all three sensors using all computed satellite/simulation reflectance ratios. These LUTs have 3 dimensions: one for the time and two for the viewing and solar zenith angles. Before the total ozone retrieval, the level-1 reflectance is multiplied by the appropriate correction factor spectrum. More details on this soft-calibration scheme are given in (Lerot et al. 2014). It is important to note that the good level-1 calibration of the OMI spectra and the very limited degradation of the instrument have made the application of the soft-calibration procedure unnecessary for generating the CCI OMI total ozone data set. The consistency with the other level-2 data sets is nevertheless excellent.

2.1.1.9 Averaging kernels

In optimal estimation, the averaging kernel **A** is defined as the product of the contribution function matrix **D**$_y$ and the Jacobian matrix **K**. Generally speaking, it is a measure of the departure of the estimator from the truth and the dependence on a priori settings. For the total column retrieval, the problem is well-posed. Accordingly, the averaging kernel matrix reduces to a vector that indicates the sensitivity of the retrieved total column to changes in ozone concentration in different layers. We calculate the averaging kernel as follows. At each wavelength, LIDORT is called to derive the ozone profile layer Jacobians **K*** using the TOMS V8 ozone profile corresponding to the final retrieved total column. The contribution function **D**$_y$ is obtained making use of the column weighting function **K**$_i$ calculated as part of the retrieval process. The averaging kernel is then given by $\mathbf{A} = \mathbf{D_y}\,\mathbf{K^*}$.

When using the LUT approach, calculating the averaging kernels would require that all Jacobians at all wavelengths are stored in a table, too, which would multiply the size of the table, again making it impossible to keep all the required data in memory. Therefore we chose to store directly precomputed averaging kernels for each grid point, fixing the fitted forward model parameters which are not part of the lookup table grid (closure, Ring amplitude and wavelength shift) at their initial values. We found that this approximation does not have any significant impact.

2.1.1.10 Error budget

Table 2 summarizes our current assessment of the main contributions to the global error budget on total ozone retrieval by direct-fitting. The error budget is given separately in two different regimes, corresponding respectively to low (<80°) and large (>80°) values of the SZA.

It includes the random error (or precision) associated with instrument signal-to-noise and which can be derived easily by the propagation of radiance and irradiance statistical errors provided in the level-1 products through the inversion algorithm. It is generally less than 0.5% at moderate SZAs and may reach 2% at SZAs larger than 80°.

The smoothing error associated to the a priori ozone profile shape used in the forward model is assessed using the formalism of Rodgers. Once we have the averaging kernel A, the error S_p due to the profile shape may be estimated as $S_p = A^T S_a A$ where S_a is the covariance matrix associated with the *a priori* profile climatology used in the inversion. What is really required here is the covariance associated with the particular retrieved total column for a specific latitude band and season. This being unavailable, we have used another total ozone classified climatology (Lamsal et al., 2004) as a proxy to construct S_a. As illustrated in Figure 2.2, the mean total ozone error due to the profile shape is less than 0.5 % at low SZAs and is as large as 4% at extreme SZA for clear sky pixels. In the case of cloud contamination, the error increases, especially at low SZA, where it may reach 1%.
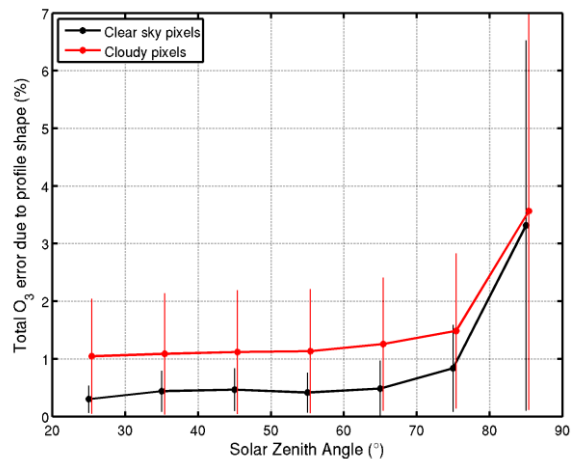
Figure 2.2: Mean total ozone error due to a priori O3 profile shape, as a function of the SZA for clear sky and cloudy pixels. Error bars represent the standard deviation of the errors.

In GODFIT, both absorption by trace gases other than ozone and the impact of aerosols are neglected in the forward model. Here, we estimate the resulting total ozone errors using closed-loop tests. Synthetic radiances are generated using the GODFIT forward model based on optical inputs that include these sources of error (e.g. NO_2 or aerosols). Then, total ozone retrieval is performed using these synthetic spectra and the retrieval settings baseline (i.e. neglecting other trace gases or aerosols in the forward model). The difference with respect to the "true" state gives the error estimate.

To simulate the impact of stratospheric NO_2, a typical stratospheric profile as depicted in Figure 2.3 has been used to generate synthetic radiances. Total ozone columns retrieved from the resulting synthetic spectra show errors of less than 0.5% for all SZAs and all surface albedos. When considering a profile with a large amount of NO_2 in the lowermost layer (e.g. representative of a heavily polluted scenario), total ozone errors increase slightly but are still less than 0.5% for low surface albedo (0.05). The errors are slightly larger than 1% when the surface albedo is high (0.8), but the likelihood of such a high NO_2 concentration above a bright surface is very small. Similar sensitivity tests have been carried out for BrO and SO_2. The errors due to their neglect are generally negligible, except for a major volcanic eruption scenario with SO_2 column amounts exceeding 50-100 DU. In this case, total ozone errors may reach a few percent.
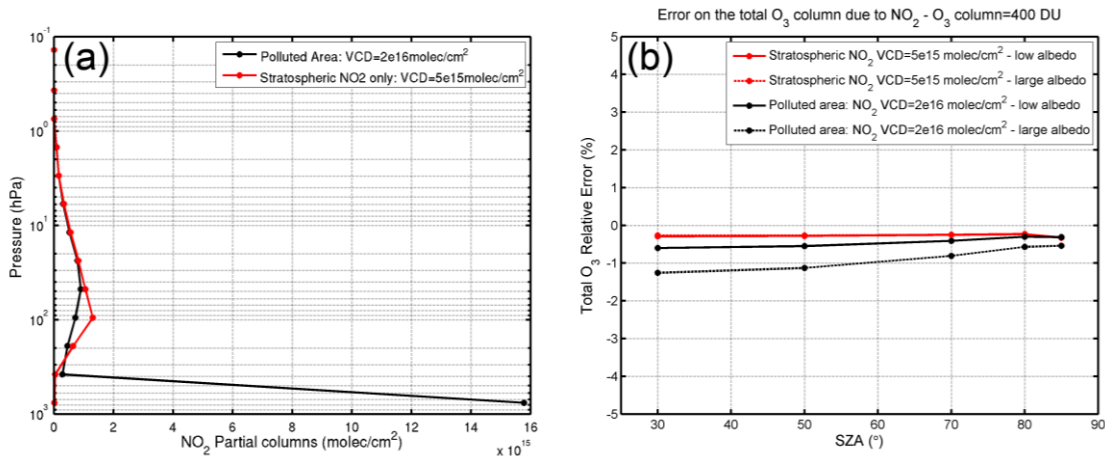
Figure 2.3: (a) NO2 vertical profiles used for generating synthetic radiances. (b) Total ozone error (%) due to neglect of NO2 in the retrieval scheme, as a function of SZA. For the two profiles shown in (a), ozone errors are plotted for low and high surface albedos (0.05 and 0.8) and for a total ozone column of 400 DU.

The same closed-loop approach has been adopted to estimate the ozone error due to neglect of aerosols in the forward model. A number of scenarios were considered, including a background aerosol case, a heavily polluted scenario with a large amount of absorbing aerosol in the lowermost layer, a dust storm scenario with a large amount of scattering aerosol in the lowermost layer and finally, two scenarios representing major volcanic eruptions with stratospheric injections of absorbing or scattering aerosols. Optical property profiles for these scenarios are plotted in Figure 2.4(a-b). The associated total ozone errors, plotted as a function of SZA in Figure 2.4(c), are generally within 1%. This small impact is mainly due to the simultaneous fit of the effective surface albedo. As seen in Figure 2.4(c) for the pollution scenario, total ozone errors are much larger (up to 4%) if the surface albedo is fixed to a climatological value. This nicely illustrates the added-value of the internal closure mode of GODFIT, which implicitly accounts for tropospheric absorbing and scattering aerosols and avoids relying on the ingestion of highly uncertain external aerosol optical property information. For a scenario with a strong injection of stratospheric aerosols due to a major volcanic eruption such as Pinatubo, the total errors may reach 10% (Figure 2.4(d)).
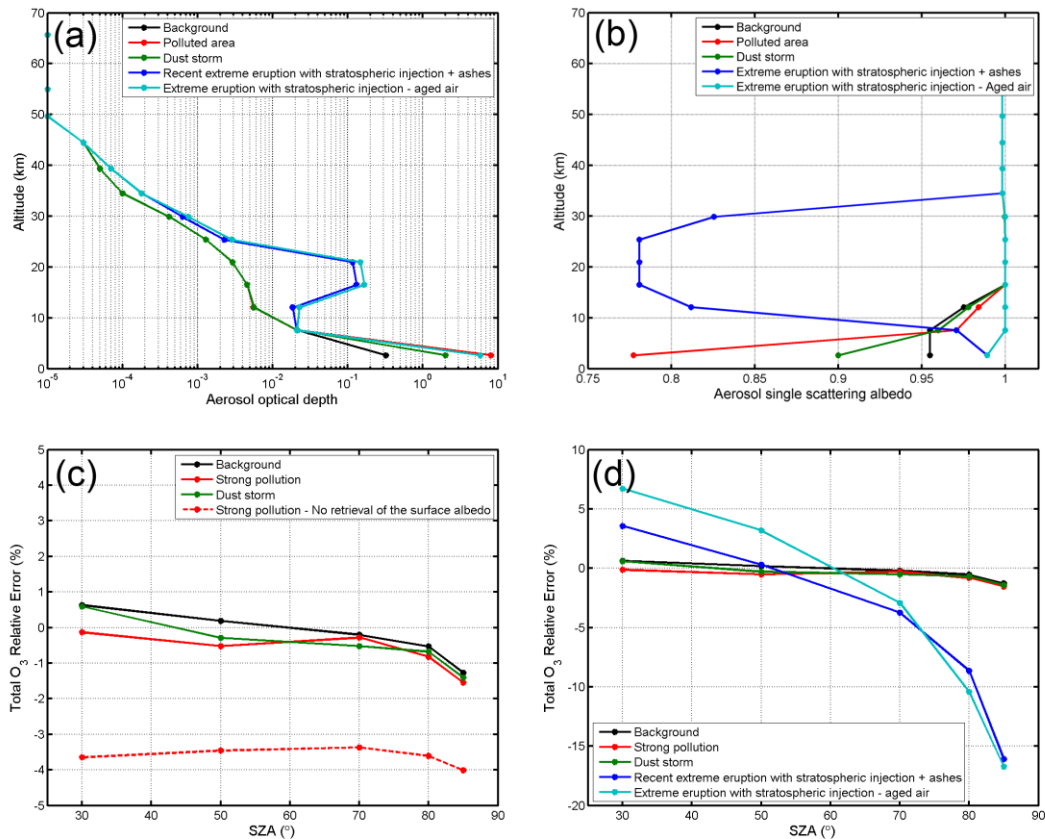
Figure 2.4: (a) Aerosol optical depth and (b) aerosol single scattering profiles used for generating synthetic radiances for a variety of scenarios (see inset and text for more details). (c) Total ozone error (%) due to neglect of aerosols in the retrieval scheme, plotted as a function of SZA for the background, polluted and dust storm scenarios. The red dashed line shows the much larger errors obtained when a fixed (non-fitted) albedo is used. (d) Same as (c) but for strong volcanic eruption scenarios.

Other uncertainty estimates have been derived from similar sensitivity tests studies carried out within previous projects (GODFIT A/B, GDP4 and GDP5) or extensively described in Lerot et al. (2013). Total errors are computed assuming all contributions are mutually uncorrelated. The total random errors are estimated to be 1.7 and 2.6 % for the low/moderate and high SZA regimes respectively. The corresponding total systematic errors are about 3.6 and 5.3%.

Table 2.2 : Estimation of the error sources of the direct-fitting total ozone retrievals (single pixel retrieval). Blue fields indicate random errors, and red fields systematic errors. The errors due to the cloud parameters (orange) are random or systematic depending on the time scale.

Error source	Per cent error	
	SZA < 80°	SZA > 80°
Instrument signal-to-noise	< 0.5	< 2
Soft calibration: Absolute recalibration + structures removal	< 1.5	< 1.5
O_3 absorption cross-sections and its atmospheric temperature	< 2.5	< 2.5
Interferences with other species (except in case of volcanic eruption)	< 1.5	< 1
Aerosols (except in case of volcanic eruption)	< 1	< 1.5
Instrument spectral stability (wavelength registration)	< 0.5	< 0.5
Solar I_0-effect	< 0.2	< 0.2
Ring effect (Rotational Raman Scattering)	< 0.1	< 0.5
O_3 profile shape	< 1	< 4
Cloud fraction	< 0.5	< 0.5
Cloud top height	< 1.5	< 1.5
Total random error (including cloud fields)	**< 1.7**	**< 2.6**
Total systematic error	**< 3.6**	**< 5.3**

2.2 Total ozone column merging algorithm

An inter-satellite calibration approach is used to create the merged total column product from GOME/ERS-2, SCIAMACHY/ENVISAT, and GOME-2/METOP-A. In order to minimize the differences between the individual sensors, SCIAMACHY and GOME-2 data are adjusted to the GOME measurements during overlap periods (D. Loyola, et al. 2009) (Loyola und Coldewey-Egbers 2012). The production of the GTO-ECV_V2 monthly mean gridded total ozone data record from April 1996 to June 2011 is as follows:

Individual GOME, SCIAMACHY, and GOME-2 level 2 total ozone data, processed with GODFIT v3.0 retrieval algorithm, are the input to the level 3 processing. Level 2 data are

first projected onto a regular grid of 1°x1°. Then, daily averages for each individual sensor are calculated for this grid, taking into account all available measurements per day and using as weighting the normalized areas of the satellite ground pixel and the regular grid intersecting polygons.

1° latitudinal monthly means are computed for GOME and SCIAMACHY based on common daily gridded data only. The correction factors for SCIAMACHY with respect to GOME are derived using the ratios of these monthly means. They comprise of two parts: (1) a 'basic' correction for each month of the year (averaged over all years from 2002 to 2011) in terms of polynomials as a function of latitude, and (2) an offset for each individual month, which is added to the 'basic' correction. This offset does not depend on latitude, but it accounts for the time-dependence in the differences between SCIAMACHY and GOME. The correction factors are then applied to the SCIAMACHY daily gridded data by linear interpolation in time.

In preparation for the GOME-2 adjustment, an intermediate product of averaged GOME and corrected SCIAMACHY daily gridded data is generated for the overlap period with GOME-2 from January 2007 to June 2011 (→ GS_MERGED daily gridded data).

The 1° latitudinal monthly means are computed for GS_MERGED and GOME-2 based on common daily gridded data only. The correction factors for GOME-2 with respect to GS_MERGED data are derived similar to the SCIAMACHY correction: polynomials as a function of latitude and month plus a time-dependent offset. They are applied to GOME-2 daily gridded data by linear interpolation in time.

The 1°x1° monthly mean gridded data are computed for GOME, adjusted SCIAMACHY, and adjusted GOME-2. Cut-off values for latitude as a function of month (see Table 2.3: Latitude coverage of the GTO-ECV_v2 total ozone data record for each month,) have been defined so that only representative monthly means are provided that contain a sufficient number of measurements equally distributed over time.

The merged GTO-ECV_V2 data record then contains GOME data from 04/1996 to 03/2003, adjusted SCIAMACHY data from 04/2003 to 03/2007, and adjusted GOME-2 data from 04/2007 to 06/2011.

Table 2.3: Latitude coverage of the GTO-ECV_v2 total ozone data record for each month,

Month	Latitudes	Month	Latitudes
January	60.0° N – 90.0° S	July	90.0° N – 57.5° S
February	70.0° N – 90.0° S	August	90.0° N – 62.5° S
March	80.0° N – 80.0° S	September	82.5° N – 72.5° S
April	90.0° N – 65.0° S	October	72.5° N – 85.0° S
May	90.0° N – 60.0° S	November	65.0° N – 90.0° S
June	90.0° N – 57.5° S	December	60.0° N – 90.0° S

2.2.1 Assessment of URD implementation for total ozone data

Table 2.4 is based on the table 5 from (O3_CCI-URD 2011) and is completed with information what is currently achievable as of the date of today.

Table 2.4: Assessment of product requirements implementation for total ozone.

Requirements as stated in URD					Compliance of the product with these requirements
Quantity	**Driving research topic**	**Geographical Zone**			
		Tropics	**Mid-latitudes**	**Polar Region**	
Global horizontal resolution	- Evolution of the ozone layer (radiative forcing); - Seasonal cycle and interannual variability; - Short-term variability: exchange of air masses, streamers, regime studies	20 – 100 km	20-50/100 km	20 – 50/100 km	A resolution of 100 km is achieved from 2002. Before, it is coarser due to the poorer resolution of GOME (~300 in Tropics; ~100 in Polar regions). A resolution better than 20 km will be achieved with future sensors.
Observation frequency		3 days	3 days	3 days	Compliant
Time period	Evolution of the ozone layer (radiative forcing)	1980-2010	1980-2010	1980-2010	From 1995 until now if focus is only on European sensors.
Accuracy[4]		2% (7 DU)	2% (7 DU)	2% (7 DU)	Compliant
Accuracy[5]	- Seasonal cycle and interannual variability; - Short-term variability: exchange of air masses, streamers, regime studies	3% (10 DU)	3% (10 DU)	3% (10 DU)	Compliant
Stability (after corrections)	Evolution of the ozone layer (1980-2010 trend detection; radiative forcing)	1 – 3% / decade	1 – 3% / decade	1 -3% / decade	3% is OK in the current status. 1% should be reached after corrections and merging.

---

[4] In this context: total error of the retrieval.

[5] idem

3   Nadir profile ECV retrieval algorithms

Both KNMI and RAL have developed algorithms for ozone profile retrieval from nadir looking instruments. After completion of the Round-Robin intercomparison exercise in summer 2013, the RAL algorithm has been selected as CCI baseline for the generation of the first version of the Ozone_cci CRDP. In this section, both KNMI and RAL algorithms are described since work is still ongoing in CCI Phase-II to incorporate elements of the KNMI algorithm in a revised CCI ozone profile algorithm baseline. The last two paragraphs describe the merged level 3 and level 4 data.

3.1   OPERA (KNMI)

The OPERA (Ozone Profile Retrieval Algorithm) is developed at KNMI to retrieve ozone profiles from nadir looking instruments. It can retrieve profiles from GOME, GOME-2, OMI. and SCIAMACHY.

3.1.1   Basic retrieval equations

When the number of profile elements to be retrieved exceeds the number of independent profile elements that can be retrieved, a naive least squares fitting produces meaningless results for real and noisy spectra. Small-scale variations in atmospheric quantities that are poorly constrained by the measurement will cause noise amplification, resulting in spurious retrieved values often showing strong oscillations. Two methods for circumventing this ill conditioning can be distinguished: (i) limiting the number of profile elements to be retrieved, and (ii) regularising the inversion problem. The first option can be realised by fitting profile elements at a limited number of carefully chosen levels in accordance with the restricted profile information in the measurement. This would require a specification of the shape of the profile between the layers. The use of a fixed vertical grid would be non-optimal for most cases.

Regularisation suppresses noise amplification by using information from a source other than the measurement. Regularisation is achieved by adding a second term to the least squares cost function J to be minimised:

$$J = \left(\mathbf{y}_m - F(\mathbf{x})\right)^{\mathbf{T}} S_y^{-1}\left(\mathbf{y}_m - F(\mathbf{x})\right) + R(\mathbf{x})$$

Eq. 3.1

Here, $\mathbf{y}_m$ is the measurement vector of radiances, $\mathbf{x}$ is the state vector of parameters to be retrieved, $F(\mathbf{x})$ is the radiance calculated by the forward model and Sy is the error covariance matrix. $R(\mathbf{x})$ is some function of the state that returns a large amplitude for 'undesirable' solutions. Two choices for the regularisation are commonly used for atmospheric retrievals; these are the Phillips-Tikhonov (Hasekamp und Landgraf 2001) and Optimal Estimation (OE) methods (C. D. Rodgers 2000). In OE, the $R(\mathbf{x})$ term is derived from the application of Bayes' theorem. This states that the probability density function (PDF) of the state is proportional to the PDF of the measurement given the state, multiplied by the PDF of the state prior to the measurement. The measurement changes the likely outcomes for the state vector elements, since it provides extra information on top of that already available from prior information. When the PDFs are all Gaussian distributions, the most probable state (the Optimal Estimate) minimises the cost function Eq. 1 with the regularisation term: $R(\mathbf{x}) = (\mathbf{x}-\mathbf{x}_a)^{\mathbf{T}} S_a^{-1}(\mathbf{x}-\mathbf{x}_a)$. Here $\mathbf{x}_a$ is the a priori state vector and S_a the prior covariance matrix.

3.1.1.1 Iterations and convergence

The solution to equation 1 can be found by iteratively applying:

$$\mathbf{x}_{i+1} = \mathbf{x}_a + D_y \left[\mathbf{y}_m - \mathbf{y}_i - K_i (\mathbf{x}_a - \mathbf{x}_i) \right] \quad \text{with} \quad D_y = S_{i+1} K_i^T S_y^{-1} \quad \text{and}$$

$$S_{i+1} = \left(K_i^T S_y^{-1} K_i + S_a^{-1} \right)^{-1}$$

Eq. 3.2

where $K_i = (\partial F / \partial \mathbf{x})_i$ is the Jacobian at state $\mathbf{x}_i$; K^T the transpose of the Jacobian, $\mathbf{y}_i = F(\mathbf{x}_i)$ and $\mathbf{x}_{i+1}$ is the updated state vector. The matrix D_y is known as the matrix of contribution functions; the solution error covariance is given by S_{i+1}. The iteration starts with some initial estimate of the state, and terminates when convergence has been reached. In OPERA, two convergence criteria can be applied, according to (C. D. Rodgers 2000). The primary criterion is that the difference between the error-weighted lengths of two consecutive state vectors, i.e. $S_x^{-1/2}(x_i - x_{i-1})$, should be below a fixed threshold. Investigations have shown that a maximum difference of 1% in gives good results for all cases. The second convergence criterion to be met is that the change in the cost function between two consecutive iterations should be less than some predefined value (for example 1%). These two criteria combine convergence tests in both state space and measurement space. The final value of the solution error covariance matrix is the main source of diagnostic information for the retrieval.

3.1.2 Forward model

The forward model consists of a radiative transfer model (RTM) that computes the radiances at the entrance of the instrument, and a slit function convolution that simulates the level 1 radiance values. The RTM has two parts. The single-scattering component and its Jacobian are computed separately using high vertical resolution ozone profiles. The multiple scattering component is computed at lower vertical resolution using the radiative transfer model LIDORTA or LABOS. In the following we describe the atmospheric set-up for the RTM, followed by a description of the single scattering RTM and the LIDORTA RTM.

3.1.3 Atmospheric state input to the RTM

For input, the RTM requires the following: a pressure grid, atmospheric profiles and cross-sections of trace gases (ozone and interfering species such as NO2 and SO2), aerosol profiles and optical parameters, surface reflection parameters, cloud parameters, solar and viewing polar and azimuth angles, the wavelength grid and the solar irradiance at these wavelengths. The vertical grid is based on user input, but it defaults to a grid of 40 layers between 41 fixed pressure levels (currently from 1000 to 0.001 hPa), where the levels in between have a fixed ratio. The actual surface pressure replaces the nominal 1000 hPa level. For cloudy and partially cloudy scenes, the cloud-top pressure replaces the nearest pressure level.

3.1.4 Radiative Transfer Model (RTM)

Given the atmospheric profiles and the cross sections, a set of optical parameters is defined for each layer; this set constitutes the basic input to the radiative transfer model for a single wavelength. These optical parameters are: layer optical thickness and single scattering albedo, and a sufficient number of phase function expansion coefficients and the exact phase function

evaluated at the scattering angle for the single scattering contribution. The RTM further requires the solar irradiance at each wavelength to compute the earth radiance. The radiative transfer problem is solved using separate models for the single and multiple scattered components.

The single-scattered radiance at TOA and the associated Jacobian is computed using an analytic solution that includes the attenuation due to the spherical shell atmosphere along the photon path (Van Oss und .Spurr 2002). The phase function is specified to high accuracy by using its exact value at the scattering angle.

The LIDORTA (Van Oss und .Spurr 2002) discrete-ordinate RTM is used for the multiple scattering computations. In an atmosphere divided into a number of optically uniform adjacent layers, the radiative transfer equation (RTE) is first solved for each layer; this is followed by the application of boundary conditions to match the radiation field at layer interfaces.

3.1.5 Error description

A general description of error theory is given in section "Data and Error Characterization". In this section we provide the results from an error computation done on a test dataset.

3.1.5.1 Test data set: Input configuration
The error computation is performed for a number of cases that cover the full range of possible measurements. We have:
- two latitudes 15N and 45N
- two cloud fractions 0.0 and 1.0,
- two solar zenith angles q_0 (30°, 75°)
- two relative azimuth angles f (0°, 180°) and
- two viewing angles q (10°, 50°). °)
- two seasons: summer and winter (i.e.: to two different a-priori ozone profiles)

The following parameters are the same for all scenarios:
- surface albedo (0.05),
- cloud top albedo (0.8),
- cloud top pressure (700 hPa) and
- wavelength range (265 – 330 nm).

This constitutes a total of 64 scenarios. *A priori* ozone profiles are selected from the ozone climatology from McPeters, Labow and Logan 2007.

3.1.5.2 Error analysis results
The calculations are done on 40 layers, but these are aggregated to 12 layer intervals in the tables. The errors are RMS values for all scenarios combined. Systematic errors are computed by mapping the error in the spectrum to a profile error using the contribution function (gain matrix).

Table 3.1 gives the RMS of the apriori and the smoothing errors using the ozone climatology from (McPeters, Labow and Logan 2007) and (Fortuin and Kelder 1999).

Table 3.2 shows the resulting errors on the ozone profile as a result of several anticipated errors in the GOME-2 Level 1b Earthshine spectrum. These measurement errors are:
- A wavelength calibration error of 1/30th pixel, both for the short [270 – 300 nm] and the long wavelength region [300-330 nm]. (systematic)

- An offset error in the radiance with a magnitude of 2% of the radiance at 270 nm. (systematic)
- A multiplicative error of 1% in the radiance at all wavelengths. (systematic)

Table 3.3: Profile errors due to systematic model parameter errors. Errors are given in percent. The columns refer to layers bounded by the pressure levels indicated in the first row.
 shows the errors in the profile due to *systematic* errors in parameters of the Forward Model. We consider:

- An error in the Rayleigh cross section of 1% at all wavelengths
- An error in the ozone cross section of 1% at all wavelengths
- An error in the temperature of 5K at all layers
- An error in the cloud-top of 100 hPa

Table 3.4 gives the profile errors due to errors in the radiative transfer model:

- the 4- stream approximation in the LIDORTA model compared to the 6 stream model,
- neglect of Rotational Raman scattering (Ring effect), excluding effect of RRS on atmospheric absorption.
- neglect of polarisation

Figure 3.1 shows the apriori, total, noise and smoothing errors for two different solar zenith angles (30.0 and 75.0 degrees), and two surface albedo values (0.05 and 0.80). The other input parameters are fixed: a clear sky, summer season at 45N, LOS 10.0, relative azimuth 0.0 and, when not varied, the SZA 30.0 and surface albedo 0.05.

Table 3.1: List of apriori and smoothing errors for indicated layers. Errors are given in percent. The columns refer to layer intervals bounded by the pressure levels indicated in the first row.

	1000-700	700-500	500-300	300-200	200-100	100-70	70-30	30-10	10-5	5-1	1-0.3	0.3-0.0
Apriori error ML O3 clim	23.2	22.9	30.2	46.7	34.4	23.7	10.7	7.3	7.9	9.1	10.6	16.1
Apriori error FK O3 clim	28.4	24.4	35.3	49.9	44.8	28.9	13.9	10.9	13.9	13.9	13.8	14.9
Smoothing error ML O3 clim	19.2	17.4	21.5	30.2	21.1	12.6	5.2	3.3	3.0	2.4	5.2	12.1
Smoothing error FK O3 clim	24.5	19.2	24.8	31.3	25.5	14.2	6.3	4.1	3.9	4.0	5.8	9.77

Table 3.2: List of measurement errors for indicated layers. Errors are given in percent. All errors are regarded as systematic. The columns refer to layers bounded by the pressure levels indicated in the first row.

|	1000-700	700-500	500-300	300-200	200-100	100-70	70-30	30-10	10-5	5-1	1-0.3	0.3-0.0
λ-scale [270-300 nm] 1/30 pix	0.2	0.2	0.2	0.2	0.2	0.2	0.1	0.1	0.1	<0.1	<0.1	<0.1
λ-scale [300-330 nm] 1/30 pix	0.4	0.5	0.5	0.5	0.5	0.4	0.1	0.1	0.1	<0.1	<0.1	<0.1
Radiance offset 2% at 270 nm	<0.1	<0.1	0.1	0.2	0.2	0.2	<0.1	<0.1	<0.1	1.2	2.3	2.9
Radiance multiplicative 1%	6.1	6.5	6.4	6.3	2.3	1.7	1.2	0.6	1.0	1.5	1.3	1.2

Table 3.3: Profile errors due to systematic model parameter errors. Errors are given in percent. The columns refer to layers bounded by the pressure levels indicated in the first row.

	1000-700	700-500	500-300	300-200	200-100	100-70	70-30	30-10	10-5	5-1	1-0.3	0.3-0.0
Rayleigh Cross sect. 1%	2.8	2.8	2.6	2.5	1.3	1.3	0.6	0.5	1.0	1.5	1.3	1.2
Ozone Cross sect. 1%	0.8	1.0	1.6	2.6	2.5	2.5	1.3	0.8	0.9	1.0	0.9	0.8
Temperature 5K	9.4	10.4	11.2	10.4	7.1	8.7	3.3	1.5	1.4	0.6	0.2	0.2
Cloud-top 100 hPa	3.8	4.2	5.0	6.4	3.4	1.5	0.5	0.2	0.2	0.2	<0.1	<0.1

Table 3.4: Profile errors due to forward model errors. Errors are given in percent. All errors are regarded as systematic. The columns refer to layers bounded by the pressure levels indicated in the first row.

	1000-700	700-500	500-300	300-200	200-100	100-70	70-30	30-10	10-5	5-1	1-0.3	0.3-0.0
4-stream error	4.0	4.3	4.6	5.4	2.6	1.6	0.9	0.3	0.3	0.1	0.0	0.0
Neglect of Ring	3.4	3.7	3.4	4.6	5.5	6.0	2.0	0.8	0.4	0.3	0.3	0.2
Neglect of polarization	28.3	29.5	29.9	32.5	14.8	4.6	3.4	1.7	1.1	0.5	0.3	0.3
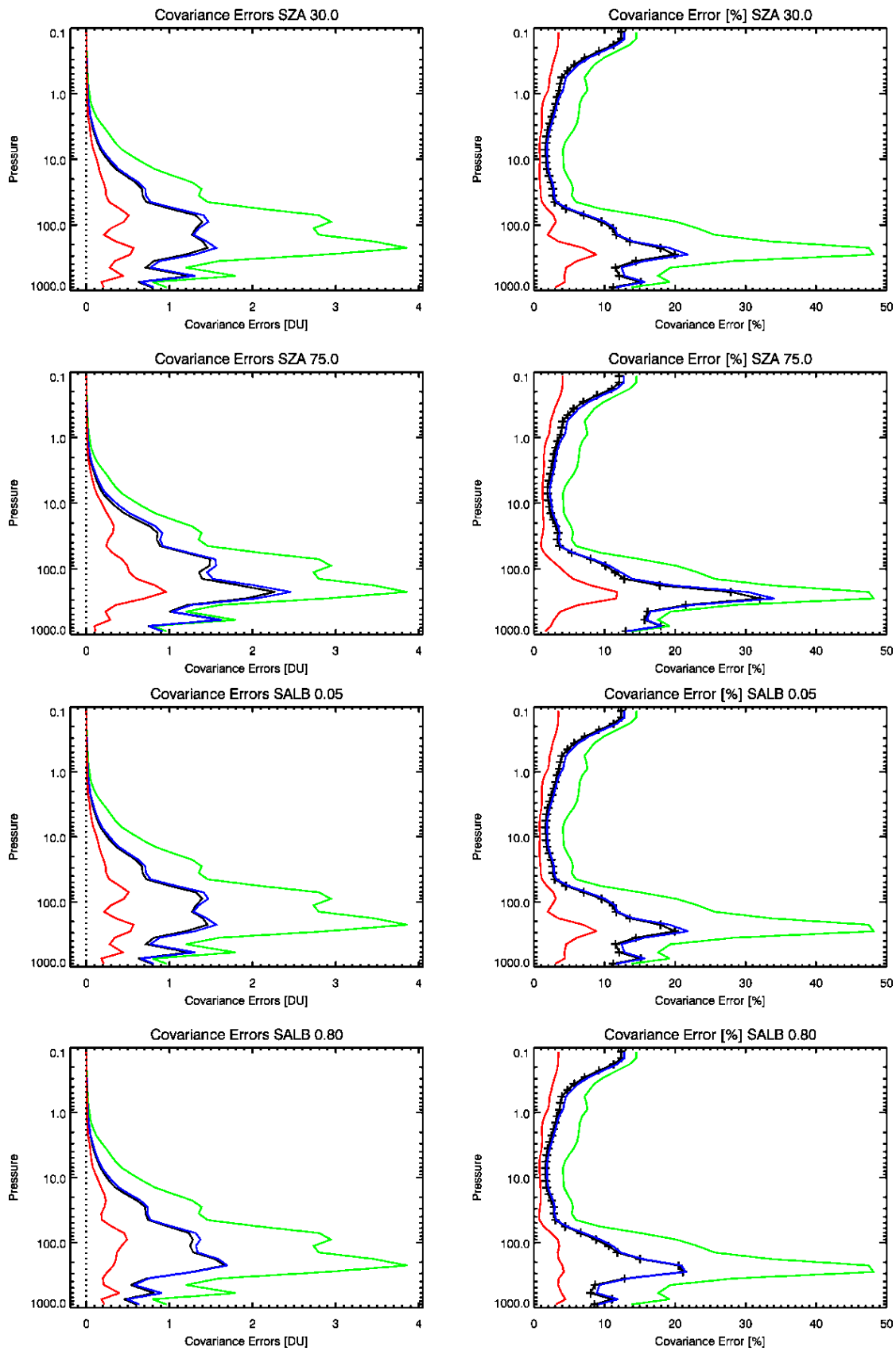
Figure 3.1: Covariance errors in DU and percent, for two SZA angles and two surface albedo values. Green: apriori error, blue: total error, black: smoothing error, red: noise error

The results indicate the following dominant error sources exceed the 5% level:

- Spectral calibration,
- Rayleigh cross section,
- Temperature
- Cloud top pressure
- 4-stream error,
- Neglect of Ring,
- Neglect of polarization.

Some of these error sources can be reduced by:

- Incorporating accurate data of optical properties in the atmospheric forward model.
- Using information on the temperature of the atmosphere from NWP models
- Using 6-streams instead of 4.
- The treatment of Raman scattering as follows. The detected radiance is separated into a contribution from elastic scattering only (Cabannes) and a contribution from radiation that has been Raman-inelastically scattered once or more. In turns out that the fraction that has been inelastically scattered twice or more is negligible for the relevant wavelength range. The consequence of this approach is that the RTM now has to run twice for every wavelength, a more exact treatment of Raman scattering would, however, cost much more.
- Using a lookup table containing polarisation errors

3.1.5.3   Output product description

Opera generates one or more output files per orbit: a full HDF5 product for offline distribution and a file containing limited information in BUFR format for Near Real Time (NRT).

The full product contains the retrieved profile (partial columns, in DU), the full error covariance matrix, the retrieval noise covariance matrix, the a-priori profile the averaging kernels and the retrieved auxiliary parameters, like surface or cloud albedo. Also included are: geolocation, spectral windows used and retrieval diagnostics, like number of iterations, spectral fit indicators.

3.2   RAL nadir profile ECV retrieval algorithms

The RAL profile scheme (Munro, et al. 1998), (Siddans 2003) scheme differs from OPERA in a number of important respects. The most significant difference is the treatment of the Huggins bands which are fitted to to a precision of better than 0.1% (close to the noise level) to allow the ozone absorption cross-section temperature dependence to be exploited for tropospheric information. This is achieved by fitting the differential absorption spectrum (log of sun-normalised radiance with polynomial subtracted) in the Huggins range rather than the absolution sun-normalised radiance, which it is necessary to fit in the Hartley band in order to obtain information at higher altitudes. This distinct treatment of the two spectral ranges leads to the formulation of the retrieval problem in 3 steps:

1) "B1 fit": Fit ozone profile to the sun-normalised radiance in the Harley band (in GOME Band 1) from 265-307nm.

2) "Albedo fit": Fit effective surface albedo for the Huggins bands GOMEfrom a narrow region (where ozone absorption is low) around 334nm (assuming the B1 ozone to be correct).

3) "B2 fit": Add information on ozone from the differential absorption spectrum in the Huggins bands. I.e. retrieve the ozone taking the B1 result to define the prior state and errors.

Methods to improve the characterisation of sub-pixel cloud in the GOME field-of-view using vis-near-ir imagery (ATSR and AVHRR) have been implemented in the RAL GOME scheme. The potential benefit of using co-located imagery in this way to improve the O3 ECV will be tested, providing a significant link to the cloud / aerosol ECV projects, which are planned to involve the application of the Oxford-RAL aerosol and cloud scheme to ATSR-2 and AATSR.

3.2.1 Basic retrieval equations

Each step of the RAL retrieval is performed using optimal estimation (C. D. Rodgers 2000). The standard equations apply.

However, the linear error analysis is somewhat complicated by the 3-step retrieval approach. Particularly as the ozone prior covariance used in step 3 is not identical to the solution covariance output from step 1. This is handled by linearizing each step and propagating the impact of perturbations in parameters affecting the measurements through to the final solution.

The following equations defined the averaging kernel, For the 3-step process, the averaging kernel is:

$$\mathbf{A} \;=\; \mathbf{D}_{y3}\mathbf{K}_3 + \mathbf{D}_{a3}(\mathbf{M}_1^3\mathbf{A}_1\mathbf{M}_1^{3t} + \mathbf{M}_2^3\mathbf{A}_2\mathbf{M}_2^{3t})$$

Eq. 3.3

Where the sub-scripts denote the matrices for each retrieval step and M is the matrix (consisting entirely of "0"s and "1"s) which maps the elements of the state vector at one step into the corresponding element of the state vector for a later step. Similarly, the impacts of perturbations in a forward model parameter are propagated via.

$$\Delta\hat{\mathbf{x}}_b \;=\; \mathbf{D}_{y3}\Delta\mathbf{b}_3 + \mathbf{D}_{a3}(\mathbf{M}_1^3(\mathbf{D}_{y1}\Delta\mathbf{b}_1)\mathbf{M}_1^{3t} + \mathbf{M}_2^3(\mathbf{D}_{y2}\Delta\mathbf{b}_2)\mathbf{M}_2^{3t})$$

Eq. 3.4

The estimated standard deviation of the final retrieval (ESD) is taken to be the square-root of the step-3 solution covariance (which includes the contribution from the other steps, in the step-3 a priori covariance).

3.2.2   Assumptions, grid and sequence of operations

3.2.2.1   Spectral ranges

In the region between 240 and 315 nm there is a relatively large spectral variation in optical depth and consequent uncertainty in the fractional polarisation, which can lead to errors of the order of a few percent in sun-normalised radiance. There is a trade-off between the improvement in ESD from including as much of this range as possible and the mapping of polarisation errors (also quasi-random due to the variability of the polarisation state introduced by cloud). These errors might be mitigated by including additional retrieval parameters, but the polarisation signature is likely to correlate to the broad absorption in this range. Similarly, the benefit of including channels towards the short wave end of the range is offset by increasing measurement errors, including noise and those due to imperfect modelling of dark-current and straylight. The range 265-307 nm is selected as the best compromise. From this range, the following sections are ignored to avoid strong Fraunhofer lines (particularly sensitive to errors in modelled leakage current, wavelength calibration and Ring effect) and the NO gamma-bands: 265-269, 278.2-280, 284-286.4, 287.2-288.8 nm.

In order to fit the Huggins bands to the required accuracy it is necessary to model the Ring effect and under-sampling. A pre-requisite of such a model is an accurate knowledge of the slit-function and the wavelength registration relative to the solar reference spectrum used in the model. For GOME-1 Pre-flight spectral calibration of the instrument was insufficient for this purpose and the scheme developed here attempts to derive the required parameters, together with a better estimate of the wavelength calibration in the region by fitting the GOME measured solar spectrum to a high-resolution solar reference spectrum.

The fitting region is restricted to 322.5 to 334nm: below this range the fit to the solar reference spectrum shows gross changes in spectral resolution and wavelength calibration. Fit residuals are also larger.

Since B2 is primarily of interest for the relatively fine-scale temperature dependent structure, the measurements in B2 are treated in a manner analogous to DOAS. The logarithm of the sun-normalised radiance is taken and a polynomial subtracted. This removes, to a large degree, independent information on the surface reflectance which modulates the mean layer photon-path profile. It is therefore important to specify (not retrieve) an accurate surface albedo as a forward model parameter in this retrieval step. This is obtained from a separate retrieval from measurements in the Huggins absorption minima between 335-340nm. It is assumed that this range is close enough in wavelength to the B2 range used for retrieval that the albedo is appropriate, while being sufficiently insensitive to absorption that the B1 fitted profile can be assumed for the Huggins band albedo fit.

After restricting the spectral range and adopting the quasi-DOAS approach above, systematic residuals remained at the 0.2% level (in sun-normalised radiance). For GOME-1 and SCIAMACHY, the mean residual over a single orbit was determined. The retrieval and FM were then modified to allow this pattern to be added to simulated measurements, scaled by a retrieved parameter. For GOME-2 a similar approach is applied, but this is currently being refined to further improve the fit.

The B1 and B2 retrievals both make use of the estimated random error on measurements provided by appropriate photon noise model. In both cases, is assumed diagonal. However, in both steps noise-floors (upper limits on the fitting precision) are imposed. The noise-floor values are arrived at empirically by inspection of fitting residuals and comparison of retrievals with climatology and validation data. In B1 the noise floor is set to 1% in sun-normalised radiance unit. In B2 the value varies with solar zenith angle, but is typically 0.05% (0.0005 in units of the natural log of the sun-normalised radiance).

Since the absolute sun-normalised radiance is used in the B1 fit, and this is subject to degradation over time (which varies from instrument to instrument). An empirical correction scheme is used to correct the L1 data in the B1 range used. This is based on modelling observed radiances based on climatological ozone distributions and fitting a polynomial in time (sufficient to capture seasonal variations) and wavelength (4th order over the band) which captures the deviations of the observations from the climatological predictions.

3.2.2.2 Vertical grid

Vertical grids are defined for the retrieval state vector and for the RTM finite-difference computational levels. To minimise changes in the scheme as it is applied globally, the same sets of levels are always used. The levels are defined in terms of pressure, so as to follow the meridional variation in tropopause height more closely than geometric altitude. They are referred to in terms of a scale-height in km, referred to as Z^*:

$$Z^*/\mathrm{km} \quad = 16(3.0 - \log_{10}(p/\mathrm{hPa}))$$

where p is pressure in hPa. This gives a value comparable to geometric height (within about 1km)

3.2.2.3 Ozone state vector

The state vector elements for ozone are the logarithm of the volume mixing ratio. Retrieval levels are defined to be 0, 6, 12 km, then at 4 km intervals up to 80 km (corresponding always to the same pressure levels of approximately 1000, 422, 177, 100.000, 56, 32, 18, 105.6, 3.2, 1.8, 1.0, 0.56, 0.32, 0.18, 0.10, 0.056, 0.032, 0.018, 0.01 hPa). These over-sample the resolution expected on the basis of averaging kernel analysis. The *a priori* covariance is used to constrain the profile shape.

An *a priori* correlation length of Δz_c=6 km is imposed for the Harley band fit (step1) I.e. the elements of S_a are given by:

$$(\mathbf{S}_a)_{ij} \quad = \quad \Delta x_{ai}\Delta x_{aj}\mathrm{e}^{-\left(\frac{z_j-z_i}{\Delta z_c}\right)^2}$$

Eq. 3.5

The values of the *a priori* and corresponding errors, Δx_{ai}, at each level i, at altitude z_i, are taken from the McPeters-Labouw or Fortuin climatology interpolated in altitude to the retrieval grid.

For the B2 fit, the *a priori* is taken from the B1A retrieval, on the same levels. Instability in the retrieval at UT/LS altitudes was encountered when the full solution covariance, from the B1A

retrieval was taken to define for the B2B retrieval. This instability was reduced by using a Gaussian *a priori* covariance with 8km correlation length and *a priori* standard deviation equal to B1A ESD.

The following deviations from the Fortuin climatology are imposed:
- At the surface and 6 km levels, the volume mixing ratio is set to the larger of the climatological value and a value corresponding to a number density of 10^{12} molec/cm3. In practice, both levels are always set to this valueexcept at very high latitude where the climatological value is greater on the 6 km level. I.e. there is no horizontal structure in the *a priori* at these levels. This approach is intended to minimise the appearance of spurious spatial/temporal patterns in retrievals at tropospheric altitudes due to *a priori* influence

- To avoid too tight an *a priori* constraint, and to avoid spurious effects in the retrieval due to the imperfect sampling of the tropospheric variance by the climatology, the relative *a priori* errors were set to the larger of the climatological standard deviation and the following:

  - 0-12km: 1 (in logarithmic units corresponding to 100% in fractional terms).

  - 6km: 0.3

  - 20-50km: 0.1

  - 56km: 0.5

  - 60-80km: 1

3.2.2.4 Other state vector elements: B1 fit

Leakage Current: A leakage current in binary units is fitted in B1, to correct for imperfect prediction of this at L1. A single parameter is fit for the band, unless the B1A/B1B boundary occurs below 307nm, in which case one parameter is fitted for each sub-band. The leakage current in BU is assumed constant with wavelength.

Lambertian effective surface albedo: A single, wavelength independent albedo is retrieved.

Ring effect: Two parameters are fitted, namely (i):
Scaling factor for the single-scattering Ring effect filling-in factor (as modelled via the approach of (Joiner, et al. 1995); (ii) Wavelength shift of the pattern relative to the nominal wavelength calibration.

Wavelength shift of the absorption cross-section: A single parameter represents a shift of the GOMETRAN modelled spectrum (before Ring effect or slit-function convolution are simulated), with respect to the measured sun-normalised radiance. The magnitude of the retrieved shift is such that it can be considered to pertain effectively to the trace-gas absorption cross sections, since the scattering coefficient varies relatively weakly with wavelength.

3.2.3 Other state vector elements: B2 fit

Ring effect: A single scaling parameter is fitted (to represent approximately the expected number of scattering events). No wavelength shift is fitted in this case; the mis-registration / under-sampling correction makes the shift of the filling-in spectrum redundant.

Wavelength shift of the absorption cross-section: The parameter has the same meaning as the corresponding B1A state-vector element. In this case a 2nd order polynomial fit to the wavelength shift is fitted across the measurement vector range.

Wavelength mis-registration between solar and back-scattered spectrum: Parameters in 3rd order polynomial expansion (as above) of the wavelength shift between the GOME solar irradiance and back-scattered spectra used to form the sun-normalised radiance.

Column amounts *of NO₂, formaldehyde* and *BrO*.
Residual scaling factor: A single scaling factor for the systematic residual.

3.2.3.1   Iterations and convergence
The standard Marquardt-Levenberg approach is used.

Convergence is judged to occur if (a) the cost function (absolute value, not normalised by the number of elements in the state vector) changes by <1 (b) at this point a Newtonian iteration (i.e. a step without applying the Marquardt-Levenberg damping) also results in a change in cost of <1. This 2nd criterion ensures retrievals do not appear to converge due to a high value of the Marquardt-Levenberg damping parameter.

3.2.3.2   Forward model

3.2.3.2.1   *Atmospheric state input to the RTM*
Temperature and pressure profiles and taken from meteorological analysis. Usually ECMWF profiles are used, though Met Office stratospheric analysis has been used in the past.

A background aerosol profile taken from MODTRAN is assumed.

Cloud may be ignored (in which case it is fitted via the retrieved surface albedos) or modelled according to information either from GOME (O_2 A-band retrieval) or co-located imagery (AATSR for GOME-1 and AVHRR for GOME-2).

3.2.3.2.2   *Radiative Transfer Model (RTM)*
The scheme uses a version of the GOMETRAN++ (Rozanov, Diebel, et al. 1997) but with a number of processing speed improvements implemented at RAL).

3.2.3.3   Error description
A quite complete study of the errors pertaining to the profile retrieval is reported in (Siddans 2003). This was based on performing retrieval simulations for a set of basic geo-physical scenario which had been defined for the GOME-2 Error Study (Kerridge 2002), which also contains a detailed error budget. For these conditions basic retrieval diagnostics such as averaging kernels (e.g. see Figure 3.2) and solution covariances were computed. A large number of additional error sources were also considered.

Figure 3.3 shows some results from (Siddans 2003). Following errors are considered:

- Aerosol: Errors in retrieved ozone introduced by deviations in the aerosol profile from the background case assumed in the FM are simulated by mapping measurement perturbations based on the following cases: [HIGH] represents a maximum boundary layer / troposphere optical depth case from the MODTRAN scenarios, with a moderate volcanic stratosphere. [BL10], [SUM] and [MODVOL] are close to the background case except in the boundary layer, troposphere and stratosphere respectively, where they are close to the [HIGH] scenario.

- [PRESSURE]: Effect of a 1% perturbation in surface pressure on scattering profile and hence retrieval (absorber number density not perturbed).

- [TEMP-2KM]: Effect of 1K error in assumed temperature profile on 2km grid. Both temperature errors are propagated through the absorption cross-section only (i.e. not via number density profile).

- [TEMP-10KM]: As, above but assuming a Gaussian correlation with 10km half-width. [TEMP-FCBKG]: As above, but taking the covariance matrix from a numerical weather prediction background error covariance matrix.

- [TEMP-IASI] As [TEMP-FCBKG], but using the estimated covariance after assimilation of IASI information.

- [MIRROR]: Errors due to the incidence angle dependence of the scan-mirror degradation.

- [POLERR-G1]: Estimated effect of error in polarisation correction given GOME-1 correction scheme (and PMD data).

- [RADCAL]: 2% Gain error. I.e. mapping of a 2% of the nominal back-scattered radiance is mapped as a systematic error, to represent radiometric calibration errors.

- The most important findings of the error assessment described here are summarised as follows:

- The retrieval provides useful information on the ozone profile below 50km.

- Retrieval precision, accounting for measurement noise and other quasi-random errors is expected to be generally in the few-percent range in the stratosphere increasing to a few 10s of percent in the lowest retrieval levels.

- Retrieved quantities should be interpreted as estimates of layer-averaged number density, taking into account the shape of the averaging kernels, and the influence of the a priori.

- The instrumental and RTM errors are generally relatively small, compared to the climatological variance and, in most cases, the ESD. Exceptions are radiometric gain errors including scan-mirror degradation (which has most impact above 40 km) and possibly imperfect knowledge of slit-function shape (expected to cause a significant negative bias in the troposphere, though the magnitude is difficult to quantify). These errors are currently addressed in the real scheme by the empirical degradation correction factor, but still represent a significant issue for long-term quality of the retrieved profiles.

- High perturbations in aerosol and errors in the assumed temperature profile give rise to retrieval errors in the troposphere of order 10-20%. (The temperature error is larger at high solar zenith angle.)

- Radiative transfer model approximations in the retrieval scheme are seen to be adequate.

- It was also noted that for GOME-1 a significant error source was lack of pre-flight measurement of the slit-function. Pre-flight characterisation of GOME-2 has much reduced uncertainties for that instrument at the beginning of life but in-orbit changes may mean this source of error is important for GOME-2 as well.
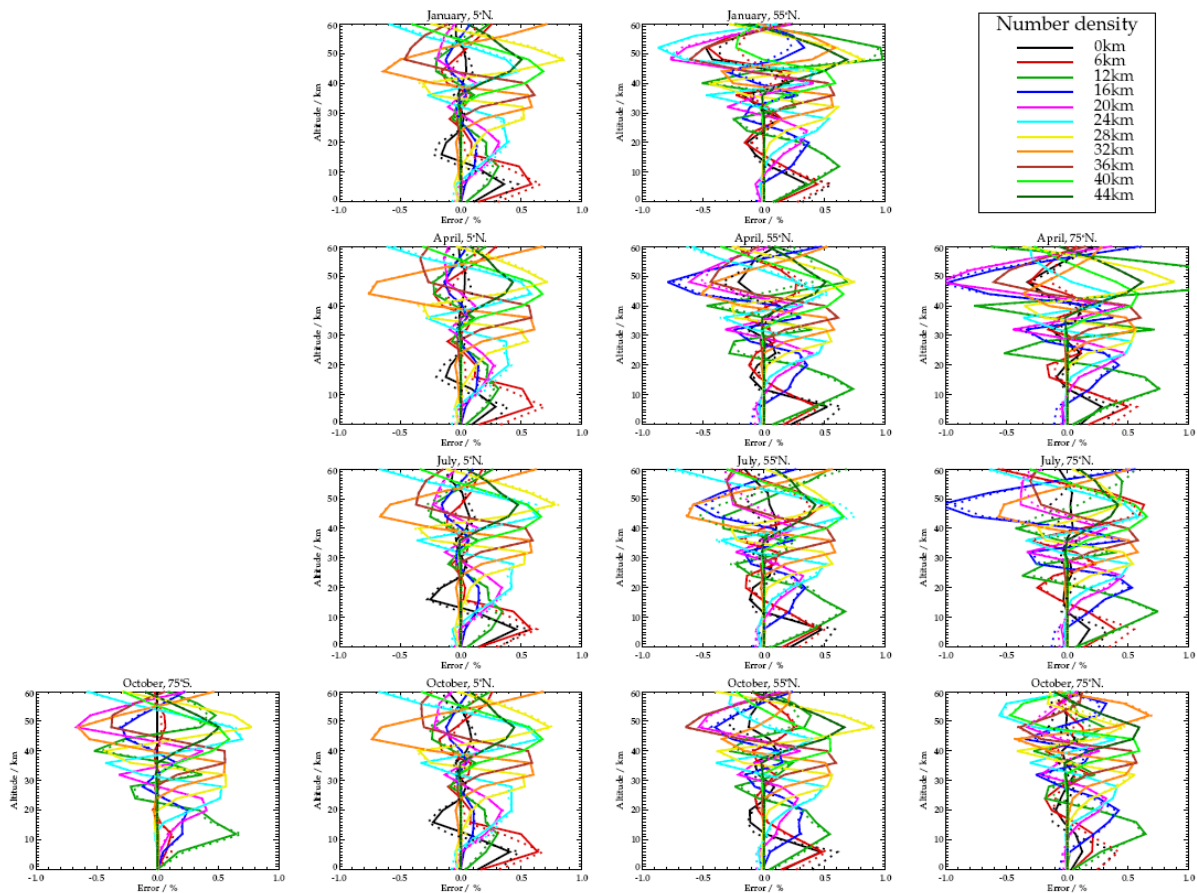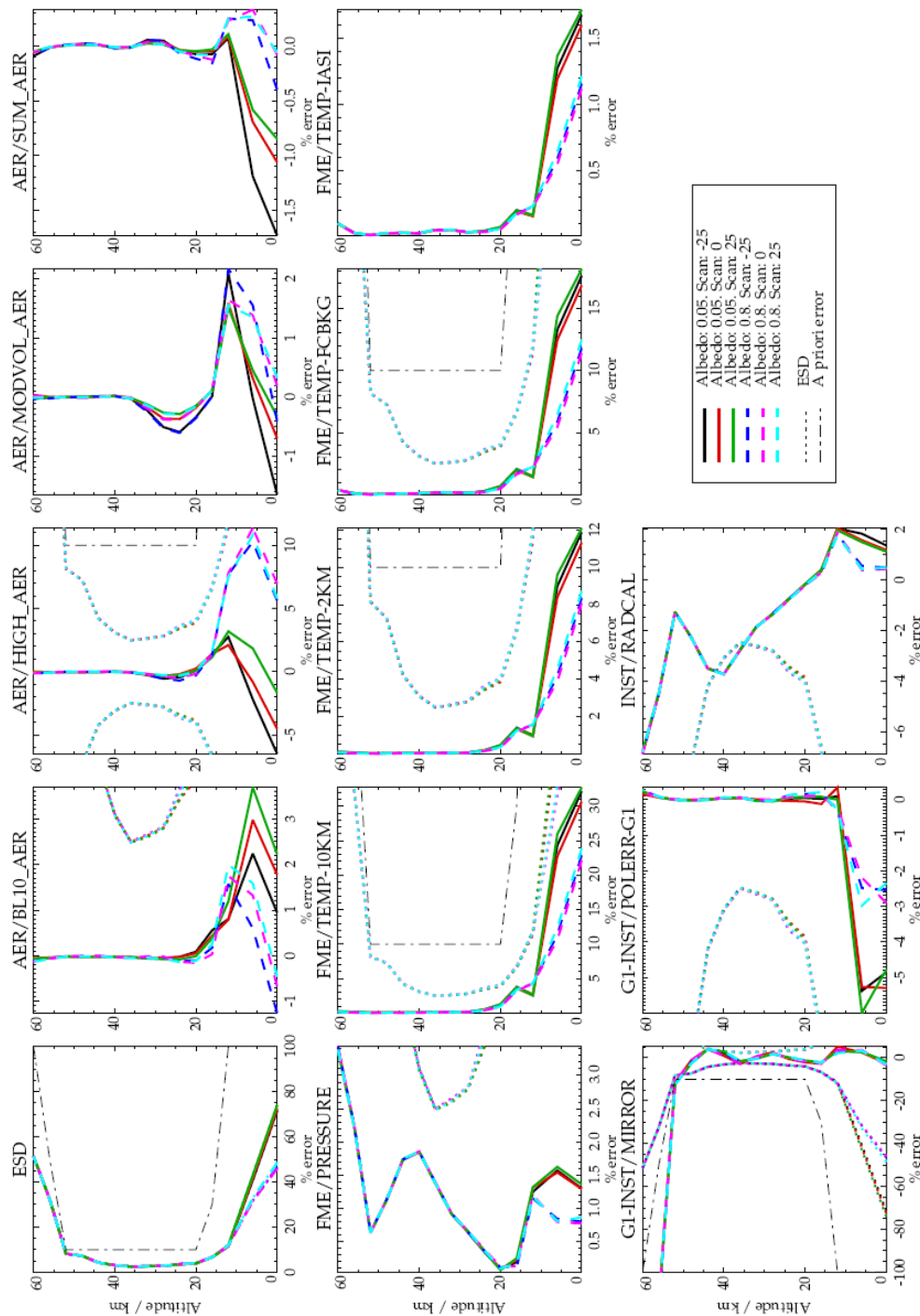

Figure 3.2: Averaging kernels (in units of retrieved number density / unit perturbation to true number density) for a range of geophysical conditions typical of given months (top to bottom) and latitudes (left to right). From (Siddans 2003).

Figure 3.3: Retrieval ESD and base-line mapped errors for GOME-1 and the April 55ºN scenario.
Dashed and solid lines refer to the 80% and 5% surface albedo cases respectively. Colours distinguish results for the 3 across-track ground pixels in B1 (the legend shows the pixel mean off-nadir angle in degrees; positive angle are East of nadir). Dotted lines in each panel other than the topleft show (for comparison) the ESD where the scale permits. The black dash-dot curve is the a priori error input to the B1 retrieval. (ESD and a priori are also plotted as negative values for comparison with negative mapped errors.)

3.2.3.4   Output product description

Retrieval results are output in ncdf format following CF convertions.

The product contains the retrieved profile (values on the retrieval levels), partial columns (integrated between retrieval levels), the full error covariance matrix, the retrieval noise covariance matrix, the a-priori profile the averaging kernels and the retrieved auxiliary parameters. Also included are: geolocation, spectral windows used and retrieval diagnostics, like number of iterations, spectral fit indicators. Each file contains results for a single orbit.

3.3   Combined nadir profile ECV retrieval algorithms

A third option for the main prototype ECV processor is the combination of both OPERA and RAL retrieval schemes. In this case OPERA would provides an initial ozone profile fitted from absolute sun-normalised radiance in the wavelength range up to 322 nm. The B2 step of the RAL algorithm would then be applied to fit the Huggins structure between 322-334 nm with the OPERA results as a-priori. This approach is to be tested during the RR exercise. Details of the resulting algorithm (if selected for further development) will be provided in ATBD v1.

3.3.1   Merged level 3 nadir profile ECV retrieval algorithms

Input: level two data from the merged ozone-cci retrieval algorithm

Output: 3D monthly mean ozone fields for all instruments. The mean field will be a weighted average based on the level-2 errors.

3.3.2   Merged level 4 nadir profile ECV retrieval algorithms: data assimilation

The data assimilation algorithm will take the level-2 data produced by the merged retrieval algorithm as input. Besides the profiles themselves, other important data that have to be provided in the level-2 product are the averaging kernel (AK) and the covariance matrices. The data are assimilated using the Kalman filter technique that is outlined in (Segers, et al. 2005). It is basically a form of optimal interpolation to find the weighted average between model results and measurements. Required for this approach are a model and it's associated uncertainties (covariance matrix) and the measurements with uncertainties and the averaging kernel. The used model is TM5 (Krol, et al. 2005).

3.3.2.1   Basic assimilation equations

The equations for the statevector $\mathbf{x}$ and the measurement vector $\mathbf{y}$ are given by:

$$\mathbf{x}_{i+1} = M\left(\mathbf{x}_i\right) + \mathbf{w}_i \quad , \quad \mathbf{w}_i \sim \mathcal{N}\left(\mathbf{0}, \mathbf{Q}_i\right)$$
$$\mathbf{y}_i = H\left(\mathbf{x}_i\right) + \mathbf{v}_i \quad , \quad \mathbf{v}_i \sim \mathcal{N}\left(\mathbf{0}, \mathbf{R}_i\right)$$

Eq. 3.6

where M is the model that propagates the statevector in time. It has an associated uncertainty $\mathbf{w}$, which is assumed to be normally distributed with zero mean and covariance matrix $\mathbf{Q}$. The observation operator H gives the relation between $\mathbf{x}$ and $\mathbf{y}$. The uncertainty is given by $\mathbf{v}$, which is also assumed to have zero mean and covariance matrix $\mathbf{R}$.   In   matrix   notation,   the propagation of the statevector and it's covariance matrix ($\mathbf{P}$) are given by:

Eq. 3.7

$$\mathbf{x}_{i+1}^{f} = \mathbf{M}\!\left(\mathbf{x}_{i}^{a}\right)$$

$$\mathbf{P}_{i+1}^{f} = \mathbf{M}\mathbf{P}_{i}^{a}\mathbf{M}^{T} + \mathbf{Q}_{i}$$

where $\mathbf{x}^{a}$ is the statevector at time t=i, after assimilation of the observations. The observations are assimilated according to:

$$\mathbf{x}_{i}^{a} = \mathbf{x}_{i}^{f} + \mathbf{K}_{i}\!\left(\mathbf{y}_{i} - \mathbf{H}_{i}\!\left[\mathbf{x}_{i}^{f}\right]\right)$$

$$\mathbf{P}_{i}^{a} = \left(\mathbf{I} - \mathbf{K}_{i}\mathbf{H}_{i}\right)\mathbf{P}_{i}^{f}$$

$$\mathbf{K}_{i} = \mathbf{P}_{i}^{f}\mathbf{H}_{i}^{T}\left(\mathbf{H}_{i}\mathbf{P}_{i}^{f}\mathbf{H}_{i}^{T} + \mathbf{R}_{i}\right)^{-1}$$

Eq. 3.8

where **K** is called the Kalman gain matrix.

The covariance matrix **P** is too large to handle, it's size is the number of elements in the state vector *squared*. For TM5 this amounts to nearly 226 billion elements. To reduce **P** to something more manageable it's parameterized into a time dependent standard deviation field and a constant correlation field.

We cannot apply the forecast equation for the covariance matrix directly because of two problems. First, because you have to add **Q**, the original parameterization is not conserved and **P** will 'fill up'. Eventually, **P** will become too large to handle. Second, errors in the ozone chemistry should also be taken into account. Therefore, the Kalman covariance propagation is replaced by an approach where we first apply the model's advection operator to the standard deviation field, and then model the error growth.

In the analysis equations, the number of elements in a ozone profile (40 for OPERA) is generally much larger than the degrees of freedom (about 5 to 6). We therefore reduce the number of datapoints per profile by taking the singular value decomposition of the AK, and transform the profiles accordingly. Since it is too costly to assimilate each OPERA pixel one by one, we assimilate a whole track at once. And finally, we use an eigenvalue decomposition to calculate the hph+r matrix inverse in the Kalman filter equation. We truncate it at a number of eigenvalues representing about 98% of the original trace.

3.3.2.2 Combining different instruments using data assimilation

Different instrument data can be assimilated at the same time with the current assimilation algorithm. Due to computational constraints it is not practical to assimilate all pixels, so a selection is made. In the future it will be considered to combine all L2 data in a model grid cell into so called 'super obeservations' which can subsequently be assimilated.

Assessment of URD implementation for nadir ozone dataTable 3.5 the assessment is made how well the nadir ozone profiles fulfill the requirements as give in Table 7 of the URD (O3_CCI-URD 2011) . The assessment is done for level 2 (L2, satellite retrievals), level 3 (L3, merged monthly mean), and level 4 (L4, assimilated) data sets. The data requirements as given in Table 8 of the URD will be fulfilled for the nadir ozone profiles, except for the data format of the L2 profiles, which will be HDF.
On the other hand the L3 and L4 profiles will be given in netCDF.

Table 3.5: Assessment of the product requirements implementation of nadir-based ozone profiles

	User Requirements as stated in URD				Compliance of the product with these requirements	
Quantity	**Driving Research topic**	**Height range**			**L2 and L3 profiles**	**L4 profiles**
		Tropo-sphere	**UT/LS**	**Middle Atmosphere**		
Horizontal resolution	Regional differences in evolution of the ozone layer and tropospheric ozone burden (radiative forcing); Seasonal cycle and interannual variability; Short-term variability*	100-200 km	100-200 km	100-200 km	This requirement is only fulfilled for the satellite instruments SCIAMACHY, OMI, and GOME-2. GOME has a resolution of 320x 80 km	Compliant
Vertical resolution	Height dependence of evolution of the ozone layer and the tropospheric ozone burden (radiative forcing); Seasonal cycle and interannual variability; Short-term variability*	6 km – Tropospheric column	3-6 km	3-10 km	Compliant, except maybe the UT/LS region	Compliant
Observation frequency	Evolution of the ozone layer and the tropospheric ozone burden (radiative forcing); Seasonal cycle and interannual variability; Short-term variability*	3 days	3 days	3 days	Only for GOME, OMI and GOME-2. The L3 profiles will be presented as monthly means and per definition do not fulfill this requirement.	Yes
Time period	Evolution of the ozone layer and tropospheric ozone burden	(1980-2010)-(1996-2010)	(1980-2010)-(1996-2010)	(1980-2010)-(1996-2010)	The period 1996-2010 is covered with the European	Depends on the L2 data

	(radiative forcing)				satellites. The period 1980-1996 might be partly covered by adding the US satellite SBUV	
Accuracy[6]	Evolution of the ozone layer and tropospheric ozone burden (radiative forcing)	10%	8%	8%	Probably only for the middle stratosphere (TBD)	Yes
Accuracy[7]	Seasonal cycle and interannual variability; Short-term variability*	20%	15%	15%	Yes	Yes
Stability	Evolution of the ozone layer and tropospheric ozone burden (radiative forcing); trends	1-3%/ decade	1-3% /decade	1-3%/ decade	Unknown yet	Depends on the L2 data

3.4 IASI FORLI Ozone profile retrieval algorithm

The IASI ozone profile data product is a new product of Ozone_cci Phase-II. It is based on the FORLI (Fast Optimal/Operational Retrieval on Layers for IASI) algorithm. FORLI is a line-by-line radiative transfer model capable of processing in near-real-time the numerous radiance measurements made by the high-spatial and high-spectral resolution IASI, with the objective to provide global concentration distributions of atmospheric trace gases.

This part describes the methods used for FORLI. Most is extracted from Hurtmans et al. (2012).

3.4.1 Basic retrieval equations

For the inversion step, it relies on a scheme based on the widely used Optimal Estimation theory (C. Rodgers, Inverse methods for atmospheric sounding: Theory and Practice, Series on Atmospheric, Oceanic and Planetary Physics - Vol. 2 2000).
The forward model equation can be written in a general way as:

$$\mathbf{y} = \mathbf{F}(\mathbf{x};\mathbf{b}) + \boldsymbol{\eta}$$

---

[6] In this context: the total error of the retrieval.
[7] idem

Eq. 3.9

where $\mathbf{y}$ is the measurement vector containing the measured radiance, $\mathbf{X}$ is the state vector containing the molecular concentrations to be retrieved, $\mathbf{b}$ represents all the other fixed parameters having an impact on the measurement (temperature, pressure, instrumental parameters...), $\boldsymbol{\eta}$ is the measurement noise and $\mathbf{F}$ is the forward radiative transfer function.

The goal of the inverse problem is to find a state vector $\mathbf{x}$, approximating the true state $\mathbf{X}$, which is most consistent with the measurement and with a certain prior knowledge of the atmospheric state. Specifically, the measured radiances $\mathbf{y}$ are combined with an *a priori* state $\mathbf{X}_a$, and both are weighted by covariance matrices representative of their statistical variations, $\mathbf{S}_\eta$ and $\mathbf{S}_a$

For a linear problem, the retrieved state, solution of the Optimal Estimation, is given by

$$\mathbf{x} = \mathbf{x}_a + (\mathbf{K}^T \mathbf{S}_\eta^{-1} \mathbf{K} + \mathbf{S}_a^{-1})^{-1} \mathbf{K}^T \mathbf{S}_\eta^{-1} (\mathbf{y} - \mathbf{K}\mathbf{x}_a)$$

Eq. 3.10

where $\mathbf{K}$ is the Jacobian of the forward model $\mathbf{F}$, the rows of which are the derivatives of the spectrum with respect to the retrieved variables.

3.4.2 Assumptions, grid and sequence of operations

3.4.2.1 Spectral ranges
FORLI-O_3 v20100815 uses the Level1C radiances disseminated by EumetCast. A subset of the spectral range, covering 1025–1075 cm^{-1}, is used for the O_3 retrieval. The spectral range used in the forward model is 960-1075 cm^{-1} and the spectral oversampling is 100.

3.4.2.2 Vertical grid
FORLI-O3 uses a vertical altitude grid in km.

3.4.2.3 Ozone state vector
The ozone product from FORLI is a profile retrieved on 39 1km-thick layers between surface and 39 km, with an extra layer from 39 to TOA.

The *a priori* profile $\mathbf{x_a}$ covariance matrix $\mathbf{S}_a$ are constructed from the McPeters/Labow/Logan climatology of ozone profiles (McPeters et al., 2007), which combines long term satellite limb measurements (from the Stratospheric Aerosol and Gas Experiment II and the Microwave Limb Sounder) and measurements from ozone sondes. The *a priori* profile $\mathbf{X}_a$ is the mean of the ensemble. Fig. 1 illustrates this *a priori* information: the *a priori* profile $\mathbf{X}_a$ has values slowly increasing from around 25 ppbv at the surface to 100 ppbv at 10km, reaching a maximum of 7.3 ppmv in the middle stratosphere. The variability (taken hereafter as the square root of the variance, i.e. of the diagonal elements of $\mathbf{S}_a$) is below 30% in the boundary layer and the free troposphere; it is maximum in the upper troposphere–lower stratosphere, between 10 and 20 km, where it is of the order of 60%. There is significant correlations between the concentrations in the layers 0–10, 10–25 and 25–40 km, but weak correlation between these three (Fig.8).

3.4.2.4 Other state vector elements
Besides the ozone profile, surface temperature and the water vapour column are retrieved.

3.4.2.5 Measurement covariance matrix

S_η is taken diagonal. The value of the noise is wavenumber dependent in the spectral range used for the retrieval, varying around 2 x 10^{-8} W/(cm^2 cm^{-1} sr).
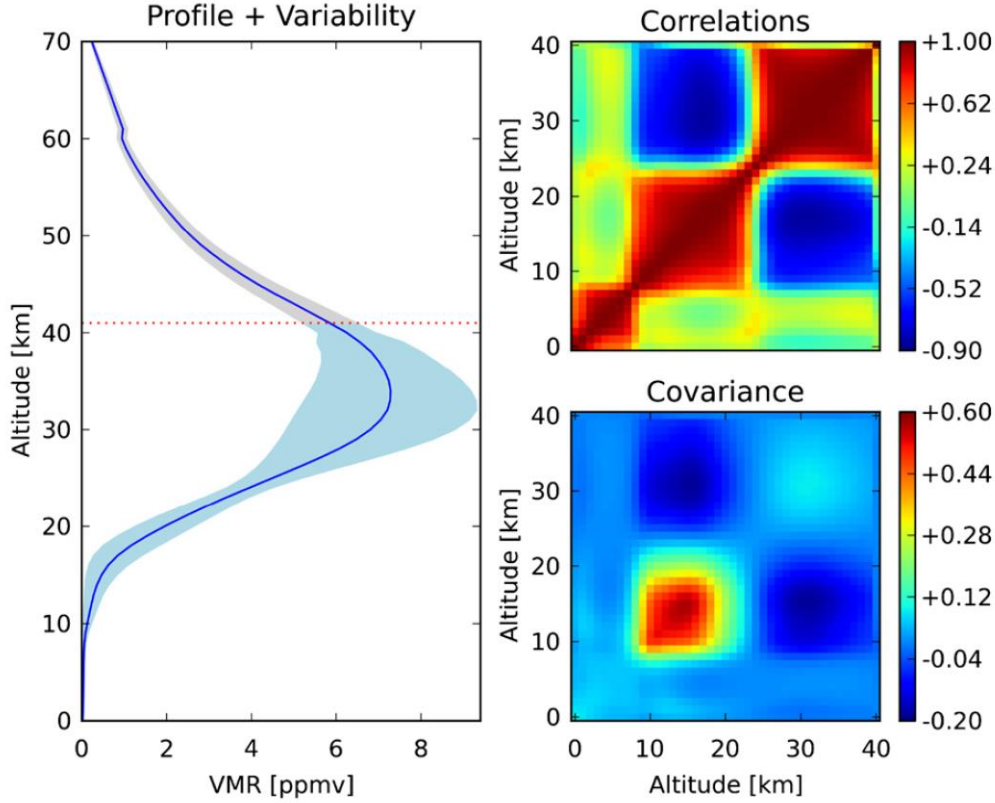

Figure 3.4: Left: *xa* (ppmv, blueline) and associated variance (shaded blue) for the FORLI-O3. The dashed red line indicates the top altitude of the last retrieved layer. Right: correlations and *Sa* variance–covariance matrices in unitless multiplicative factor. (from Hurtmans et al. 2012).

3.4.3 Iterations and convergence

We assume a moderately non-linear problem, where equation Eq. 3.11 is iteratively repeated using a Gauss-Newton method until convergence is achieved. For iteration j :

$$\mathbf{x}_{j+1} = \mathbf{x}_a + (\mathbf{K}_j^T \mathbf{S}_\eta^{-1} \mathbf{K}_j + \mathbf{S}_a^{-1})^{-1} \mathbf{K}_j^T \mathbf{S}_\eta^{-1} [\mathbf{y} - \mathbf{F}(\mathbf{x}_j) + \mathbf{K}(\mathbf{x}_j - \mathbf{x}_a)].$$ **Eq. 3.11**

The gain matrix $\mathbf{G}$ is the matrix whose rows are the derivatives of the retrieved state with respect to the spectral points. From equation Eq. 3.11, it can be shown that:

$$\mathbf{G} = (\mathbf{K}^T \mathbf{S}_\eta^{-1} \mathbf{K} + \mathbf{S}_a^{-1})^{-1} \mathbf{K}^T \mathbf{S}_\eta^{-1}.$$ **Eq. 3.12**

Convergence is achieved when

$$d_i^2 = [\mathbf{F}(\mathbf{x}_{i+1}) - \mathbf{F}(\mathbf{x}_i)]^T \mathbf{S}_{\delta\hat{y}}^{-1} [\mathbf{F}(\mathbf{x}_{i+1}) - \mathbf{F}(\mathbf{x}_i)] \ll m$$ **Eq. 3.13**

where $\mathbf{S}_{\delta\hat{y}} = \mathbf{S}_\delta (\hat{\mathbf{K}} \mathbf{S}_a \hat{\mathbf{K}}^T + \mathbf{S}_\delta)^{-1} \mathbf{S}_\delta$ and m is the degrees of freedom.
Eq. 3.11

3.4.4 Forward model

3.4.4.1 Atmospheric state input to the RTM

3.4.4.1.1 L1C radiances

FORLI-O_3 v20100815 uses the Level1C radiances disseminated by EumetCast. A subset of the spectral range, covering 1025–1075 cm $^{-1}$, is used for the O_3 retrieval.

3.4.4.1.2 Temperature and humidity profiles

Profiles of temperature and humidity are from the IASI L2 PPF (August et al., 2012). The atmospheric temperatures are kept fixed whereas the water profile is used as a priori and further adjusted.

3.4.4.1.3 Surface temperature

Surface temperatures (land and sea) are from the IASI L2 PPF. Surface temperature is part of the parameters to be retrieved.

3.4.4.1.4 Cloud fraction

v20100815 uses the cloud fraction from the IASI L2 PPF. All pixels with a cloud fraction equal to or lower than 13 % are processed.

3.4.4.1.5 CO_2 profile

A constant vertical profile at 380 ppm is assumed for CO_2.

3.4.4.1.6 Orography

Orography is from the GTOPO30 global digital elevation model and is integrated in the entire IASI FOV (http://eros.usgs.gov/#/Find_Data/Products_and_Data_Available/gtopo30_info).

3.4.4.1.7 Emissivity

A wavenumber-dependent surface emissivity above continental surfaces is used while for ocean a single standard emissivity is considered. For continental surfaces it relies on the climatology of Zhou et al. (2011). In cases of missing values in the Zhou et al. climatology, the MODIS climatology of Wan (2008) is used. It is available on a finer 0.05° × 0.05° grid but is restricted to only 12 channels in the IASI spectral range. In order to deal with this, the spectrally resolved mean emissivity of the Zhou climatology is scaled to match as closely as possible the values in these 12 channels and it is this resulting emissivity that is considered. Finally, when there is no correspondence between the IASI FOV and either climatologies, then the mean emissivity of the Zhou climatology is used.

3.4.4.1.8 Lookup-tables

Tabulated absorption cross-sections at various pressures and temperatures are used to speed up the radiative transfer calculation. The spectral range for the LUTs used in v20100815 is 960-1075 cm^{-1} and the spectral oversampling is 100. The absorption cross-sections are computed on a logarithmic grid for pressure from 4.5×10^{-5} to 1 atm with a grid step of 0.2 for the logarithm of pressure, and on a linear grid for temperature (162.8–322.6 K with a grid step of 5K). Relative humidity is also introduced in the LUT, varying linearly between 0 and 100%, by steps of 10%.

3.4.4.1.9 Spectroscopy

Line integrated absorption cross section, air broadening, self-broadening, line shifting and absorption cross section data are taken from the widely used HITRAN spectroscopic database version 2008 (Rothman et al., 2009). Continuum formulations are taken from MT-CKD (Clough et al., 2005).

3.4.4.2 Radiative Transfer Model (RTM)

3.4.4.2.1 General formulation

3.4.4.2.1.1 Ray tracing for upward flux

The Ray-tracing defines for off-nadir geometries the path s versus the altitude z. This path depends on the zenith angle of the beam (θ) as seen from the surface, which, under the approximation of a flat atmosphere, is equal to $\sec(\theta)$. Although the plane-parallel approximation could reasonably be applied for IASI at near-nadir, it is not adapted at larger viewing angles. The spherical shape of the Earth is explicitly accounted for in FORLI by including a local radius of curvature for the Earth $R_{\oplus}$ and the index of refraction of air. The elementary path is then written as

$$ds = \frac{n(z)(z + R_{\oplus})dz}{\sqrt{n^2(z)(z + R_{\oplus})^2 - R_{\oplus}^2 n^2(z_G)\sin(\theta)}} \qquad \textbf{Eq. 3.14}$$

where $n(z)$ is the index of refraction of air at altitude z. The altitude dependency is expressed through the variation of temperature, pressure and humidity and is modelled using the Birch and Downs formulation (Birch and Downs, 1994). The index of refraction is considered constant in the IASI spectral range. In order to calculate the path along the line of sight, Eq. 3.14 is integrated using a numerical method, as no analytical closed form exists.

3.4.4.2.1.2 Radiative transfer

Local thermodynamic equilibrium is assumed. The monochromatic upwelling radiance at TOA is then calculated as

$$L^{\uparrow}(\tilde{v};\theta,z) = L^{\uparrow}(\tilde{v};\theta,0)\tau(\tilde{v};\theta,0,z) + \int_0^z J(\tilde{v},\Omega,z')\frac{\partial}{\partial z'}\tau(\tilde{v};\theta,z',z)dz' \qquad \textbf{Eq. 3.15}$$

where $L^{\uparrow}(\tilde{v};\theta,0)$ is the radiance at the start of the light path (i.e. that of the emitting surface) at wavenumber $\tilde{v}$ with a ground zenith angle of θ, $\tau(\tilde{v};\theta,z',z)$ is the transmittance from altitudes z' to z, and $J(\tilde{v},\Omega,z')$ is the atmospheric source term which depends on both thermal emission and scattering.

For FORLI, only clear or almost-clear scenes (cloud fraction in the field--of--view (FOV) lower than typically 20%; see specific documents for CO, O$_3$ and HNO$_3$ for threshold values) are analyzed and the atmosphere is therefore considered as a non-scattering medium. In that case J becomes independent on geometric angle, thus simplifying to the black-body emission function $B(\tilde{v},T)$.

The transmittance $\tau(\tilde{v};\theta,z',z)$ in equation 3.13 is related to the absorption coefficient κ by:

$$\tau(\tilde{v};\theta,z',z) = \exp\left[-\int_{z'}^z \sum_j \kappa_j(\tilde{v};z'')\rho_j(z'')\frac{\partial s(\theta,z'')}{\partial z''}dz''\right] \qquad \textbf{Eq. 3.16}$$

where j refers to a given gaseous species, $\rho_j(z'')$ is the molecular density of that species at altitude z'', and $s(\theta,z'')$ is the curvilinear path determined by the ray tracing. The absorption coefficient κ contains absorption features described by single spectral lines; regions affected by absorption of heavier species (where cross-sections would need to be used) are avoided. Also absorption continua are explicitly considered in the calculation of κ.

A precise calculation of the Earth's source function $L^{\uparrow}(\tilde{v};\theta,0)$ in Eq.3.15 has to be achieved to properly model the spectrum recorded at TOA. That term is basically governed by the black-body emission of the ground surface, modified, however, by the emissivity and reflectivity of that surface. Considering a surface of emissivity $\grave{o}(\tilde{v})$:

$$L^{\uparrow}(\tilde{v};\theta,0) = \grave{o}(\tilde{v})B(T_{skin}) + (1-\grave{o}(\tilde{v}))L_0^{\downarrow\dagger}(\tilde{v}) + \alpha(\tilde{v})L_0^{\downarrow\mathring{a}}(\tilde{v})$$

Eq. 3.17

where $B(T_{skin})$ is the ground black-body Planck function at the ground temperature T_{skin} ;

$$L_0^{\downarrow\dagger}(\tilde{v}) = \frac{1}{\pi}\int_0^{2\pi}d\phi\int_0^{\pi/2}d\theta \ L_0^{\downarrow}(\tilde{v};\theta)\sin(\theta)\cos(\theta)$$

Eq. 3.18

is the mean radiance associated to the total downward flux reaching the surface, integrated upon all the geometries considering a Lambertian surface; $\alpha(\tilde{v})L_0^{\downarrow\mathring{a}}(\tilde{v})$ is the fraction of sun light that is retro-reflected in the direction of the sounding beam, which depends on the sun azimuthal angle and the surface effective *reflectivity* $\alpha(\tilde{v})$. In FORLI both contribution from Lambertian and specular reflections are explicitly taken into account, following:

$$\alpha(\tilde{v}) = ((1-\grave{o}(\tilde{v}))\mu_{\delta0} + \rho\mu_{glint})6.7995 \times 10^{-5}$$

Eq. 3.19

With

$$\mu_{\delta0} = \frac{\cos\theta^{\mathring{a}}}{\pi}$$

Eq. 3.20

$$\mu_{glint} = \frac{\cos\theta + \cos\theta^{\mathring{a}}}{\sqrt{2[1+\sin\theta^{\mathring{a}}\sin\theta\cos(\phi-\phi^{\mathring{a}})-\cos\theta\cos\theta^{\mathring{a}}]}}$$

Eq. 3.21

where θ , $\theta^{\mathring{a}}$, ϕ and $\phi^{\mathring{a}}$ are the sun and satellite zenith and azimuth angles respectively, and where ρ in equation 3.19 is the effective reflectivity for specular reflection; the last factor on the right hand side of that equation is the sun solid angle. Note that $L_0^{\downarrow\mathring{a}}(\tilde{v})$ in equation 3.17 is modelled by a Planck blackbody function at 5700 K, without including spectral lines.

3.4.4.2.2 *Numerical approximations*
In order to perform the radiative transfer calculation, a discretized layered atmosphere has to be considered. Typically, a 1 km-layered atmosphere is assumed. The convention adopted here is to label the levels from O to N for altitudes starting from ground to the TOA, with an atmospheric layer bounded by two levels. The layer index is then ranging from 1 to N . For each layer, average parameters $(e.g. \ \bar{T}_i, \bar{P}_i, \ldots)$ are computed.

3.4.4.2.2.1 **Ray tracing**
Equation 3.12 is integrated for each layer using a Gauss-Kronrod quadrature scheme. For each layer, the partial column of each molecule j is also computed using

$$PC_{i,j} = \int_{z_i}^{z_i+1}\rho_j(z)\frac{ds(z)}{dz}dz$$

Eq. 3.22

where $\rho_j(z)$ is the molecular density (in molecule/cm^3).

3.4.4.2.2.2 **Radiative transfer**

Assuming clear sky, equation 3.15 is discretized using a recursive representation evaluated successively for each layer $i = 1 \ldots N$:

$$L_i^\uparrow = \overline{B_i} + (L_{i-1}^\uparrow - \overline{B_i})\tilde{\tau}_i \qquad \textbf{Eq. 3.23}$$

where $\overline{B_i}$ is the average constant Planck function for layer i computed at the average temperature $\overline{T_i}$ of that layer and $\tilde{\tau}_i = \tau(\tilde{v}; z_i, z_{i-1})$ is the effective transmittance of that layer. $L_0^\uparrow$ is evaluated using successively two recursions similar to equation 3.17, the first being to approximate the downward flux $L_0^{\downarrow\dagger}(\tilde{v})$. The evaluation of this equivalent downward flux integral in equation 3.18 is simplified by computing an effective downward radiance with an zenith angle of 53.5°, which approximates the integral within a few percent for 0.9% (Elsasser, 1942; Turner, 2004). Accordingly, the computational cost gain is made at a minor error cost in most situations.

Effective transmittances are computed for each layer using a formulation close to the analytical form equation 3.17, but using the average parameters:

$$\tilde{\tau}_i = \exp\left[-\sum_j PC_{i,j}\sum_l \kappa_{j,l}(\tilde{v};\overline{T_i},\overline{P_i})\right] \qquad \textbf{Eq. 3.24}$$

where i refers to the layer; j, to the molecular species; and l, to the spectral line when relevant. For water vapour, the water concentration enters in the line shapes definition, and we should rigorously write $\kappa_{j,l}(\tilde{v};\overline{T_i},\overline{P_i},\mathrm{VMR}_{j,i})$.

A special feature of FORLI is to work with unit less multiplying factors $M_{i,j}$ instead of the partial columns $PC_{i,j}$ themselves. The multiplying factors are calculated with respect to the *a priori* profiles, except for water vapour for which the level 2 first guess retrieved at EUMETSAT CAF (August et al., 2012) is used instead. Therefore equation 3.24 becomes:

$$\tilde{\tau}_i = \exp\left[-\sum_{j=\text{fitted}} M_{i,j}PC_{i,j}\sum_l \kappa_{j,l}(\tilde{v};\overline{T_i},\overline{P_i}) - \sum_{j=\text{fixed}} PC_{i,j}\sum_l \kappa_{j,l}(\tilde{v};\overline{T_i},\overline{P_i})\right] \qquad \textbf{Eq. 3.25}$$

where the sum runs over the fitted molecules and the j --fixed molecules.

The total state vector ends up to be all the multiplying factors $M_{i,j}$ and all the non-molecular parameters (ground temperature T_{skin}, emissivity or spectral/radiometric calibration parameters) that have to be adjusted. Specifically in FORLI, only $M_{i,j}$ (the trace gas profile and the water vapour column) and T_{skin} are retrieved.

3.4.5 Error description

The fitted variance-covariance matrix $\hat{\mathbf{S}}$, representing the total statistical error after the retrieval, is written:

$$\hat{\mathbf{S}} = (\mathbf{K}^T \mathbf{S}_\eta^{-1} \mathbf{K} + \mathbf{S}_a^{-1})^{-1}. \qquad \textbf{Eq. 3.26}$$

It includes the contribution from the smoothing error and the measurement error, which can be decomposed according to Rodgers (2000).

Averaging kernels are calculated as:

$$\mathbf{A} = \mathbf{GK}$$

<div align="right">**Eq.3.27**</div>

where $\mathbf{G} = (\mathbf{K}^T \mathbf{S}_\eta^{-1} \mathbf{K} + \mathbf{S}_a^{-1})^{-1} \mathbf{K}^T \mathbf{S}_\eta^{-1}$.

<div align="right">**Eq. 3.28**</div>

Typical averaging kernels are represented in Figure 9.

3.4.6   Output product description

3.4.6.1   Formats
The FORLI-O_3 retrieval results will be delivered in NetCDF.

3.4.6.2   Ozone profile and characterization
The ozone product from FORLI is a profile retrieved on 39 layers between surface and 39 km, with an extra layer from 39 to TOA. It is provided along with averaging kernels and relative total error profile, on the same vertical grid.

3.4.7   Retrievals and Quality flags

Quality input flags:
-Missing T, Q, Cloud input values
-Negative surface altitudes
-Unrealistic skin temperature
Quality processing flags:

-Overall Convergence was reached (indicates successful retrieval)
-Convergence not reached after maximum number of iterations
-Too high values for Chi Square
-No retrieval done! (due to incorrect inputs or other reasons).
-Residuals "biased" or "sloped" or large RMS values
-Fit diverged
-Unrealistic averaging kernels
-Total error covariance matrix ill conditioned
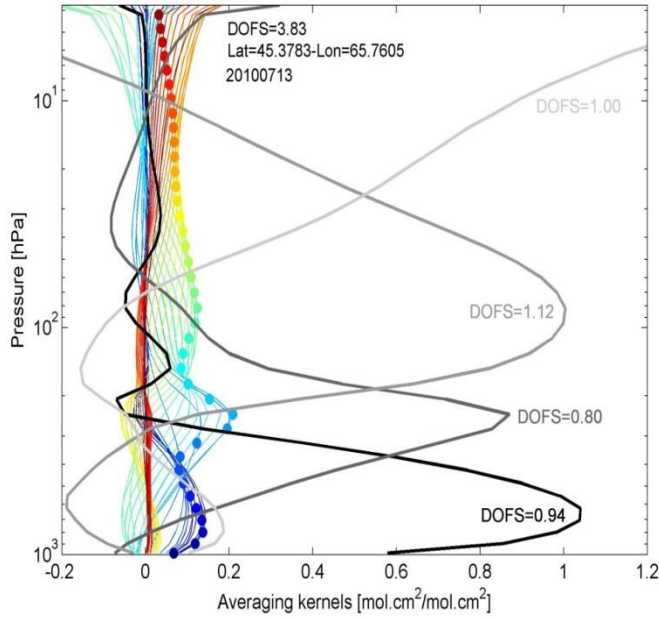
Figure 3.5: Example of averaging kernels for FORLI-O3 retrievals.

4 Limb profile ECV retrieval algorithms

4.1 MIPAS IMK-Scientific (KIT)

The MIPAS retrieval baseline has been selected in a Round-Robin exercise (Laeng et al., 2014). It is based on the IMK/IAA algorithm. The IMK/IAA Scientific Processor design description figures in more than 50 peer-reviewed publications. More details about description below can be found in (von Clarmann, Glatthor, et al. 2003), (von Clarmann, Hoepfner, et al. 2009) and (Glatthor, et al. 2006).

4.1.1 Basic Retrieval Equations

In the retrievals performed with the IMK-IAA data processor, MIPAS level-1B spectra are inverted to vertical profiles of atmospheric state parameters.
After linearization of the radiative transfer problem and after writing the solution into the context of Newtonian iteration in order to take nonlinearity into account, the estimation of state parameters is performed iteratively as following:

$$\mathbf{x}_{i+1} = \mathbf{x}_i + \left(\mathbf{K}_i^T \mathbf{S}_y^{-1} \mathbf{K}_i + \mathbf{R} + \lambda \mathbf{I}\right)^{-1} \left(\mathbf{K}_i^T \mathbf{S}_y^{-1} \left[\mathbf{y}_{meas} - \mathbf{y}(\mathbf{x}_i)\right] - \mathbf{R}(\mathbf{x}_i - \mathbf{x}_a)\right).$$

Eq. 4.1

The retrieval is performed by constrained non-linear least squares fitting of modelled to measured spectra (C. D. Rodgers 2000) by minimising the objective function

$$\chi^2 = (\mathbf{x} - \mathbf{x}_a)^T \mathbf{R}(\mathbf{x} - \mathbf{x}_a) + (\mathbf{y} - \mathbf{f}(\mathbf{x}))^T \mathbf{S}_y^{-1}(\mathbf{y} - \mathbf{f}(\mathbf{x}))$$

Eq. 4.2

Here:

- $\mathbf{x_i}$ is the n_{max}-dimensional vector of unknown parameters estimated on *i*-th iteration

- $\mathbf{y}$ and $\mathbf{f(x_i)}$ are the measured and the modelled spectral radiances,

- $\mathbf{K_i}$ is the m_{max} x n_{max} Jacobian, containing the partial derivatives of all m_{max} simulated measurements $\mathbf{y}$ under consideration with respect to all unknown parameters $\mathbf{x}$

- $\mathbf{K_i}^T$ denotes the transposed matrix $\mathbf{K_i}$,

- $\mathbf{S_y}$ is m_{max} x m_{max} covariance matrix of measurement noise,

- $\mathbf{R}$ is n_{max} x n_{max} regularization matrix (see Section 4.1.5)

- $\mathbf{x_a}$ is the related a priori information (see Section 4.1.5)

- $\mathbf{y_{meas}}$ is the m_{max}-dimensional vector of measurements under consideration,

- $\lambda \mathbf{I}$ is n_{max} x n_{max} Levenberg-Marquardt term (see Section 4.1.6)

4.1.2   Diagnostics

IMK-IAA MIPAS results are characterized by error estimates, as well as vertical and horizontal averaging kernels. The latter two are used to estimate the spatial resolution of the retrievals.

The gain function is calculated as follows:

$$\mathbf{G} = (\mathbf{K}^T \mathbf{S}_y^{-1} \mathbf{K} + \mathbf{R})^{-1} \mathbf{K}^T \mathbf{S}_y^{-1}$$

Eq. 4.3

The covariance matrices of the state vector and of the measurement are linked by

$$\mathbf{S}_x = \mathbf{G} \mathbf{S}_y \mathbf{G}^T$$

Eq. 4.4

The averaging kernel matrix, reflecting the sensitivity of the retrieved profile to the change of state parameters is

$$\mathbf{A} = \mathbf{G} \mathbf{K} = (\mathbf{K}^T \mathbf{S}_y^{-1} \mathbf{K} + \mathbf{R})^{-1} \mathbf{K}^T \mathbf{S}_y^{-1} \mathbf{K}$$

Eq. 4.5

In addition, the horizontal smoothing information is calculated for sample cases on the basis of the 2-dimensional averaging kernel $\mathbf{A_{2D}} = \mathbf{G} \mathbf{K_{2D}}$ where $\mathbf{K}$ is the 2-dimensional Jacobian. The random error covariance matrix $\mathbf{S}_{random}$ of the retrieved quantity $\mathbf{x}$ is calculated as

$$\mathbf{S}_{random} = (\mathbf{K}^T \mathbf{S}_\mathbf{y}^{-1} \mathbf{K} + \mathbf{R})^{-1} \mathbf{K}^T \mathbf{S}_\mathbf{y}^{-1} \mathbf{K} (\mathbf{K}^T \mathbf{S}_\mathbf{y}^{-1} \mathbf{K} + \mathbf{R})^{-1}$$

Eq. 4.6

and the linear mapping $\Delta \mathbf{x}_j$ of the uncertainty Δb_j of parameter b_j is

$$\Delta \mathbf{x}_j = \left(\mathbf{K}^T \mathbf{S}_y^{-1} \mathbf{K} + \mathbf{R} \right)^{-1} \mathbf{K}^T \mathbf{S}_y^{-1} \times \left[\mathbf{y}(\mathbf{x}, b_j + \Delta b_j) - \mathbf{y}(\mathbf{x}, b_j) \right]$$

Eq. 4.7

Two additional criteria are usually applied to the retrieved data in order to evaluate the quality of the profile:

1) results where the diagonal value of averaging kernel is less (in absolute value) than 0.03 are considered non-trustful.

2) results related to parts of the atmosphere non-sensed by MIPAS (i.e. below the lowermost used tangent altitude) are considered non-trustful.

4.1.3   Assumptions, grid and discretization

IMK/IAA Scientific Processor retrieves the stratospheric Ozone Profiles from MIPAS/ENVISAT limb emission spectra. The retrieval strategy is based on constrained inverse modelling of limb radiances. In stratospheric/tropospheric retrievals, local thermodynamic equilibrium (LTE) is assumed.

The retrieval is performed on a discrete altitude grid (1-km grid width from 4–44 km altitude, 2-km gridwidth from 44–70 km, 5-km gridwidth from 70–120 km, with some additional levels for temperature and H_2O). This grid is a compromise between accuracy and efficiency and has been developed during numerous test retrievals. The retrieval quantity is ozone volume mixing ratio (vmr). Ozone mixing ratio is assumed horizontally homogenous, while temperature is assumed not to be so. Considering the horizontal temperature gradients generally diminish the total error of the retrieval, by reducing the number of convergence failures, particularly near the polar vortex boundary.

4.1.4   Sequence of operations

The processor is designed so that the major contributors to the infrared spectrum are the first to be retrieved, before the gases with tiny spectral features.

First, the spectral shift of the measurements is determined. Then, temperatures and altitude pointing information (i.e. the elevation angle of the line of sight of the instrument) are jointly retrieved. The sequence of retrieval operations is: H_2O, O_3 and then other trace gases. As a general rule, results of preceding steps are used as input for the subsequent retrieval steps, i.e. the H_2O retrieval uses retrieved temperatures and pointing information, and the subsequent O_3 retrieval uses retrieved H_2O abundances, etc. Beside each target species, microwindow-dependent continuum radiation profiles and microwindow-dependent, but height-independent zero level calibration corrections are jointly fitted. H_2O is retrieved in the *log* domain.

4.1.5 Regularization

The IMK-IAA processor performs regularized retrievals on an altitude grid (spacing of 1 km up to 44 km and of 2 km between 44 and 70 km), which is finer than the spacing of MIPAS tangent altitudes which is 3-km for reduced resolution measurements. This implies that stable solutions can only be obtained by regularization. The processor uses a smoothing constraint, which operates by weighted minimization of the squared first order finite differences of adjacent profile values, using a Tikhonov (1963) formalism. The intent of this choice is to make the resulting profiles less dependent on the a priori profiles.

The first order difference operator $\mathbf{L_1}$ applied to profile is looks like

$$\begin{pmatrix} -1 & 1 & 0 & \cdots & 0 & 0 \\ 0 & -1 & 1 & \cdots & 0 & 0 \\ & & & \ddots & & \\ 0 & 0 & 0 & \cdots & -1 & 1 \end{pmatrix} \mathbf{x} = \mathbf{L}_1 \mathbf{x}$$

To run the least square method, we extend the cost function by component of

$$\mathbf{x}^T \mathbf{L}_1^T \mathbf{L}_1 \mathbf{x} = \mathbf{x}^T \begin{pmatrix} 1 & -1 & 0 & 0 & \cdots & 0 & 0 & 0 \\ -1 & 2 & -1 & 0 & \cdots & 0 & 0 & 0 \\ 0 & -1 & 2 & -1 & \cdots & 0 & 0 & 0 \\ & & & & \ddots & & & \\ 0 & 0 & 0 & 0 & \cdots & -1 & 2 & -1 \\ 0 & 0 & 0 & 0 & \cdots & 0 & -1 & 1 \end{pmatrix} \mathbf{x},$$

The goal is to minimize the cost function

$$\chi^2 = (\mathbf{y} - \mathbf{f}(\mathbf{x}))^T \mathbf{S}_y^{-1} (\mathbf{y} - \mathbf{f}(\mathbf{x})) + \gamma \mathbf{x}^T \mathbf{L}_1^T \mathbf{L}_1 \mathbf{x}$$

Eq. 4.8

which is achieved when

$$\hat{\mathbf{x}} = \mathbf{x}_0 + \left(\mathbf{K}^T \mathbf{S}_y^{-1} \mathbf{K} + \gamma \mathbf{L}_1^T \mathbf{L}_1 \right)^{-1} \mathbf{K}^T \mathbf{S}_y^{-1} (\mathbf{y} - \mathbf{f}(\mathbf{x}_0))$$

Eq. 4.9

The regularization term in the IMK/IAA MIPAS retrieval thus is

$$\mathbf{R} = \gamma \mathbf{L^T_1 L} \ .$$

As a priori in ozone processing we use $\mathbf{x_a}$=0, which means that the retrieved profile can be seen as a smoothed version of the true profile.

All trace gases are regularized against an altitude-constant a priori profile. Its actual value is meaningless, since in this case the smoothing regularization applied affects only the shape of the profile and not the actual values. The altitude-constant choice of the a priori profile avoids artefacts when the altitude of a stratospheric peak or a sharp bend near the tropopause is located at a different altitude in the a priori data compared to the true atmosphere. This approach implies that the resulting profile is, apart from deviations due to measurement, parameter or model errors, a smoothed version of the true profile without bias or further distortion. The only variables regularized by maximum a posteriori approach are the elevation of the lines of sight (von Clarmann, Glatthor, et al. 2003) and the horizontal temperature gradients. The latter (but

not the temperatures themselves!) are constrained with a zero order ECMWF Tikhonov-type regularization towards data, which is equivalent to a maximum a posteriori formalism (C. D. Rodgers 2000) with a diagonal ad hoc a priori covariance matrix. The latter was set such that for high altitudes, where ECMWF analysis data are thought to be less reliable, the information on the horizontal temperature gradients is extracted mainly from the measurements, while for lower altitudes, where a single limb scan contains little information on the horizontal temperature distribution but where ECMWF analyses are more reliable, the retrieval is strongly constrained towards the a priori.

4.1.6   Iterations and convergence

The minimization of the cost function is done with Newtonian iteration scheme where the Jacobian $\mathbf{K}_i$ and modelled spectra $\mathbf{f}(\mathbf{x_i})$ are updated within each iteration i. In order to avoid divergence due to $(\mathbf{x_{i+1}} - \mathbf{x_i})$ being so large that the region where the linearization of $\mathbf{f(x)}$ is valid is left, the Levenberg-Marquardt method is used (Levenberg 1944), (Marquardt 1963). Namely, the optional term $\lambda\mathbf{I}$ (tuning scalar times unity) damps the step width $(\mathbf{x_{i+1}} - \mathbf{x_i})$, bends its direction toward the direction of the steepest descent of the cost function in the parameter space and prevents a single iteration from causing a jump of parameters $\mathbf{x}$ beyond the linear domain around the current guess $\mathbf{x_i}$ (Levenberg-Marquardt scheme). Usually λ is set to zero and the Levenberg-Marquardt term is activated only if otherwise the retrieval tends to diverge.

The iteration is considered converged if each of the following criteria is fullfilled:
1. Linearity: spectral convergence is achieved in two subsequent iterations according to the criterion below:

$$\frac{|\,\mathbf{f}(\mathbf{x}_i)+\mathbf{K}(\mathbf{x}_{i+1}-\mathbf{x}_i)-\mathbf{f}(\mathbf{x}_{i+1})\,|}{|\,\mathbf{f}(\mathbf{x}_i)+\mathbf{K}(\mathbf{x}_{i+1}-\mathbf{x}_i)+\mathbf{f}(\mathbf{x}_{i+1})\,|} < \varepsilon_{linear_{1,2}}$$

Eq. 4.10

with two different thresholds ε_{linear} in two subsequent iterations must hold for all $\mathbf{y}$

2. Parameter convergence:

   for all n, $|\mathbf{x}_{n,i} - \mathbf{x}_{n,i-1}| < \varepsilon_{converged}$

3. Penalty function convergence:

   $\chi_i^2 < 1.02 * \chi_{i-1}^2$

4. Levenberg-Marquardt term is desactivated:

   $\lambda = 0$

4.1.6.1   Microwindows

Microwindows are narrow spectral intervals suited for retrieval of temperature or species abundances profiles. Their optimal boundaries are found by minimization of the estimated total error (von Clarmann, T; Echle, G. 1998) The altitude-dependent selection of microwindows is stored in so-called occupation matrices (OMs). Starting from a set of automatically generated

microwindows (Echle, et al. 2000) the microwindow selection used here was modified in order to better remove impact of non-LTE which might have been underestimated in the initial microwindow selection, reduce the impact of further interfering species not yet considered then, and avoid spectral lines whose spectroscopic data prove inconsistent with those of the majority of lines.

Table 4.1: Microwindows for MIPAS IMK/IAA ozone retrieval.

Microwindow cm^{-1}	Altitude coverage 6–68 km
	00111222333344566
	69258147036927208
741.675–741.825	====T====TTTTTTT=
744.950–745.125	=TTTTTTTTTTTTTTTT
757.900–758.000	==TTTTTTTTTTT===T
759.225–761.650	TTTT==TTTTTTTTTTT
764.800–764.950	T==TTTTTT==TT=TTT
798.450–798.650	===TTTTTTTTTTTTTT
1062.325–1062.475	====T=========TTT
1081.500–1081.600	TTTTT=TTTTTTTTTTT
1090.350–1090.475	TTTTT=TTTTTTTTTTT
1108.000–1108.350	TTT=T===TT=T=====

4.1.6.2 Error budget

This section is based on (Steck 2007).
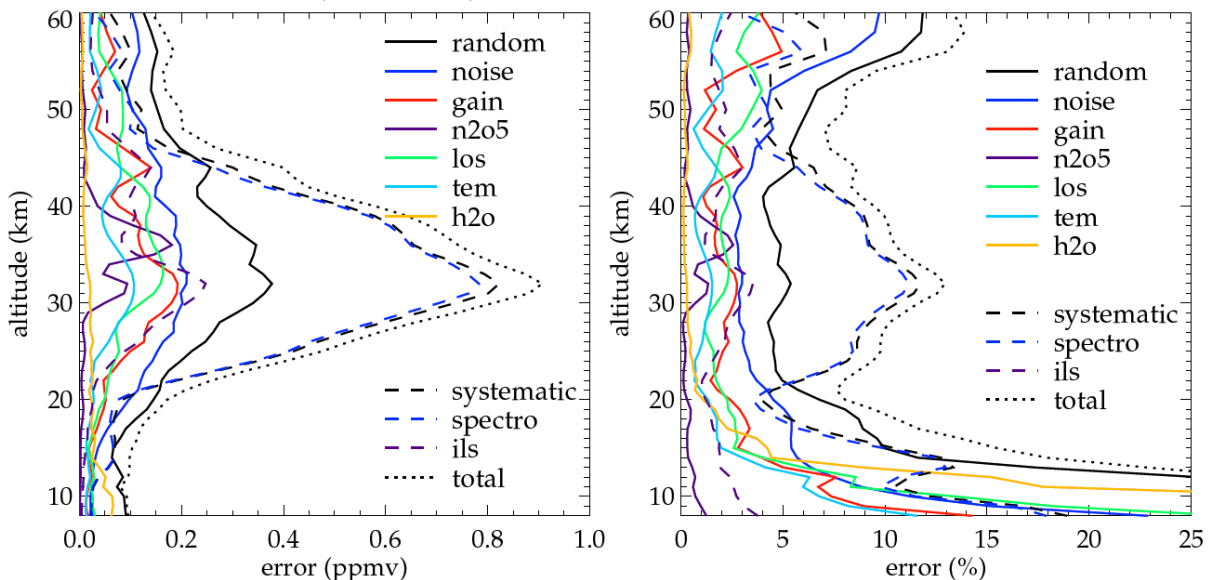
Figure 4.1: Estimated ozone error budget of MIPAS averaged over selected locations (4 seasons, 5 latitude bands, night and day). Left: absolute, right: percentage errors.

Error! Reference source not found. shows the MIPAS ozone error budget averaged over selected locations (4 seasons, 5 latitude bands, night and day). The estimated total random error (**Error! Reference source not found.**, right, solid black) varies between 4 and 7% between 20 and 52 km corresponding to values in volume mixing ratios (**Error! Reference source not**

found.10, left, solid black) of 0.15 parts per million by volume (ppmv) and 0.35 ppmv in this altitude region. The percentage errors are slightly increasing towards 60 km (12%) and down to 15 km (10%). Below 15 km the percentage errors are rapidly increasing to values in the order of 25% for polar and midlatitude conditions or more than 50% for tropical conditions, where the vmr is small. The error in vmr remains below 0.1 ppmv. The estimated random error is dominated by the instrumental noise above 14 km (**Error! Reference source not found.**10, left, solid blue). Below 14 km, the error due to uncertain water vapor concentration becomes dominant (**Error! Reference source not found.**, left, solid beige). The reason for that is the exponentially increasing water vapor with decreasing altitude which leads to a dominant water vapor signal in MIPAS spectra. These strong water vapor lines are slightly interfering with ozone lines leading to a dependence of the retrieved ozone on the pre-retrieved water vapor amount. Also errors due to uncertain gain calibration, N2O5, line-of-sight (LOS) pointing, and temperature contribute noticeably. The estimated total systematic error (**Error! Reference source not found.**, right, dashed black) is mainly between 4 and 14% (corresponding to 0.1 and 0.8 ppmv, **Error! Reference source not found.**, left, dashed black) with maxima near the ozone maximum and in the lowermost stratosphere and below.

The error is dominated by uncertainties in spectroscopic data (**Error! Reference source not found.**10, right, dashed blue). The altitude-dependence of errors due to spectroscopic data is due to the fact that the microwindows used in the retrieval are varying with altitude. Errors caused by uncertainties in the ILS (instrumental line shape) are in the order of 1 to 4% and thus nearly negligible compared to spectroscopic uncertainties.

4.2 SCIAMACHY IUP V3.5 (IUP Bremen)

4.2.1 IUP SCIATRAN Retrieval

The IUP-scientific retrieval processor is based on the software package SCIATRAN Version 3.1 (Rozanov, et al. 2002) (Rozanov, et al. 2014). The ozone profile retrieval is done using the Optimal Estimation (OE) approach (C. D. Rodgers, Inverse Methods for Atmospheric Sounding: Theory and Practice 2000) with first order Tikhonov constraints. The following equation has to be solved by this method:

$$\hat{y} = Kx + \varepsilon \qquad\qquad \textbf{Eq. 4.11}$$

where $\hat{y}$ is defined as follows:

$$\hat{y} = y - y_0 \qquad\qquad \textbf{Eq. 4.12}$$

and is the difference between the logarithms of measured and simulated retrieval vectors, which are determined from the limb-radiance profiles as described in section 4.1. The linearization is achieved by forward model operator K where the weighting functions are the elements of the matrix K. The state vector $\hat{x}$ is the difference between the a priori and retrieved vertical distributions of ozone concentration:

$$x' = x - x_0 \qquad\qquad \textbf{Eq. 4.13}$$

with the errors denoted as ε. The calculation is done in terms of Eq. 4.11 in the retrieval. The unknown parameter or profile x can be retrieved using the OE method of inversion:

$$x = x_0 + SK^T S_y^{-1}(y-y_0) \qquad \textbf{Eq. 4.14}$$

where S is the solution covariance matrix and S_y is the noise covariance matrix. The solution covariance matrix can be calculated as follows:

$$S = (K^T S_y^{-1} K + S_a^{-1})^{-1} \qquad \textbf{Eq. 4.15}$$

where S_a is the a priori covariance matrix. The theoretical precision of the retrieval is then defined as the square root of the diagonal elements of the matrix S. The vertical resolution of the retrieved profiles can be quantified using the FWHM of the averaging kernels, i.e. columns of the averaging kernel matrix A. A is given by the following expression:

$$A = SK^T S_y^{-1} K \qquad \textbf{Eq. 4.16}$$

By using the equations (4.11), (4.12) and (4.16) we can simplify equation (4.14) into the following:

$$x_{ret} = A \cdot x_{true} + (E-A)x_0 + AK^{-1}\varepsilon \qquad \textbf{Eq. 4.17}$$

From this equation it is trivial to see that the retrieval vector equals the true profile if the averaging kernel matrix A equals the identity matrix E with zero noise $\varepsilon=0$. An example of averaging kernels for SCIAMACHY is plotted in Figure 11 a with corresponding FWHM of AKs (**Error! Reference source not found.**) for averaging kernels between 14−48 km.
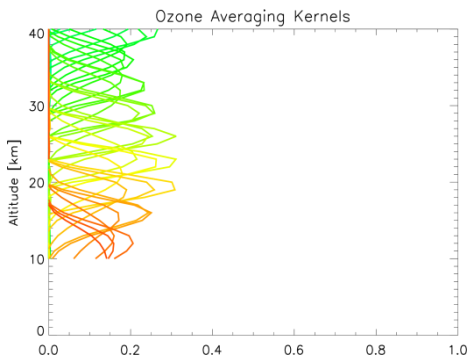

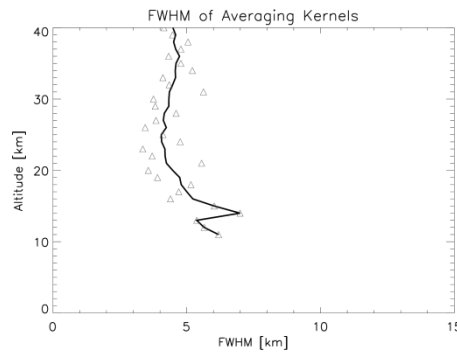**Figure 4.2: Example of SCIAMACHY O3 Averaging Kernels.**

Figure 4.3: SCIAMACHY FWHMs for the altitude range of 14 - 48 km.

4.2.2 Discrete Wavelength Method in V2.X

In order to retrieve ozone concentration profiles from limb scatter observations the discrete wavelength method has been used (Flittner, Bhartia und Herman 2000) (von Savigny, et al. 2005) (Sonkaew, et al. 2009). In the first step the normalized limb radiance profiles $I_N\lambda,TH)$ are calculated for each wavelength, by dividing the limb radiances at tangent height TH by the limb radiance at a reference tangent height TH_{ref} (See Table 11). For the Chappuis band normalized radiance profiles at three different wavelengths are selected and combined. The three

wavelengths are: $(\lambda_1 \lambda_2 \lambda_3)$= (525 nm, 590 nm, 675 nm). These wavelengths are combined to the Chappuis retrieval vector y_c as follows:

$$y_c=\ln[\ I(\lambda_2,TH)/\text{Square Root}\ (I(\lambda_1,TH)\ I(\lambda_3,TH)] \qquad \textbf{Eq. 4.18}$$

In addition to the Chappuis wavelengths the normalized limb radiance profiles at 8 UV wavelengths are used in the retrieval. Table shows the wavelengths, tangent height entries and the assumed signal-to-noise-ratios (SNR). The tangent height entries (18-24) correspond to 50-70 km for the 264 nm and 8-40 km (5-15) for the 675 nm wavelength in 3 km steps respectively.

Table 11: The wavelengths used with corresponding lowest THlow and reference THref tangent height entries and SNR.

λ [nm]	264	267.5	273.5	283	286	288	290	305	525	590	675
TH_{low}	18	18	18	16	16	16	16	13	5	5	5
TH_{ref}	24	24	24	23	22	22	21	19	15	15	15
SNR	15	15	15	30	30	30	30	50	140	140	140

The final measurement retrieval vector y contains the natural logarithms of the normalized UV limb radiance profiles as well as the Chappuis retrieval vector. The cloud optical thickness and cloud extinction coefficient have the strongest effect on the retrieved ozone profiles (Sonkaew et al., 2009). The retrieval is rather insensitive to changes in cloud water droplets size, solar azimuth angle (SAA), cloud geometrical thickness and cloud top height for constant cloud optical thickness.

The following changes of the IUP Bremen Limb Ozone (STRATOZONE for version 2.1) as reported (Mieruch, et al. 2012) have been implemented:

- Version 2.2: add Albedo data base (Matthews 1983)
- Version 2.3: use ECSTRA Aerosol data base has been added (Fussen und Bingen 1999)
- Version 2.4: Level 1 V 7.03-7.04 scia data instead of Level 1 V 6.03
- Version 2.5: Four State (horizontally)/Limb measurements, instead of an average over all states
- Version 2.9: Level 1 V7.04 consolidation grade W

4.2.3   Polynomial Approach in V 3.X

A new algorithm has been developed for limb measurements in order to solve issues, mainly to address the drift, bias, and insufficient quality of ozone in the UTLS region, present in the limb ozone V2.9.

The new approach is using the spectral information from Hartley, Huggins and short-wave wing of the Chappuis band.

The spectral information used to establish the measurement vector is dependent on the altitude of interest. For example, at the altitudes level of 61 and 58 km, the spectral interval of 264 – 273.8 nm has been used by excluding the two windows of 265 – 266.5 nm and 267.5 – 272.5 nm, with no polynomial subtraction

This stepwise selection of the spectral intervals is proceeded to build up the total measurement vector from which the different altitudes of the ozone profile is then retrieved. An overview of the spectral intervals of the logarithm of the normalized radiances with k-th order of polynomials subtraction, normalization scheme, and retrieved albedo is shown in Table 12.

Table 12: Retrieval scheme for different spectral intervals, by using the polynomial approach in SCIAMACHY IUP V3.5.

Altitudes [km]	TH_ref. [km]	Spectral interval [nm]	Excluded interval [nm]	Kth-Order of Polynomial	Normalization	Albedo
58 – 61	68	264 – 273.8	265-266.5 & 267.5-272.5	-	Tangent Height	-
51 - 55	64	276.5 – 284	278 – 282.5	0th	Tangent Height	-
38 - 55	58	289 – 309.5	-	0th	Tangent Height	-
32 - 38	-	325.5 - 331	-	1st	Solar	Surface
9 - 32	-	495 - 576		2nd	Solar	Surface

The retrieved ozone concentrations are retrieved at measurement tangent heights, with the surface albedo in the UV and visible range along with auxiliary parameters of NO_2 number densities at measurement tangent heights, and O_4 total column. Clouds and strongly increased aerosol in the field of view, by using the SCODA algorithm (Eichmann et al., 2016), can be detected. Measurements at these tangent heights, and below, are rejected.

4.2.4 Iterative approach

An iterative approach is applied to account for the non-linearity of the inverse problem. The iteration is stopped when the convergence criterion is reached. A Gauss-Newton iterative scheme is used to find a solution (C. D. Rodgers, Inverse Methods for Atmospheric Sounding: Theory and Practice 2000):

$$x_{i+1} = x_0 + S K_i^T S_y^{-1} (y - y_i + K_i(x_i - x_0)) \qquad \textbf{Eq. 4.19}$$

The iterative process, which is limited to a maximum of 40 steps, is stopped after one of the following convergence criteria is reached. The first criterion is that the relative change of the root mean square (RMS) of the fit residual $RMS_{i+1}/RMS_i - 1$ is lower than 10^{-4}. The second criterion is the relative change of the retrieved parameters with a threshold of 0.01, which is defined as the maximum change in the number densities between 10 km and 40 km. A spectral point is considered as an outlier if the remaining residual is larger than six times the RMS.

4.2.5 Regularization

For the regularization procedure two covariance matrices are important: the measurement covariance matrix S_y and the a priori covariance matrix S_a. The values for the elements of the a priori covariance matrix are set as relative variances. The diagonal elements of the measurement covariance matrix are determined as $1/SNR^2$. The diagonal elements of the a priori covariance matrix, S_a, are defined as variances with typical values of $1 - 10$. The pre-defined SNR for the eleven wavelength segments are used (see Table 11) for all altitudes. The off-diagonal elements of the a priori covariance matrix are defined as follows:

$$S_a{}^{i,j} = \sigma^2 \cdot e^{-|zi-zj|/rc}$$

Eq. 4.20

where σ is the variance, z_i and z_j are the altitudes corresponding to the element (i,j) of the covariance matrix, and $r_c \approx 1.5$ km is the correlation radius. The smoothing of the retrieved profiles is done by applying the Tikhonov regularization scheme.

The Tikhonov matrix is added to the a priori covariance matrix S_a and the new solution covariance matrix $S*$ is then calculated as follows:

$$S* = (K^T S_y{}^{-1} K + S_a{}^{-1} + S_t{}^T S_t)^{-1}$$

Eq. 4.21

where S_t is a first order derivative matrix weighted by an appropriate Tikhonov parameter which linearly increases with altitude from 3 at 7 km to 9 at 75 km.

4.2.6 Auxilliary Data

The temperature and pressure profiles for the location, date and time at each limb measurement are taken from the ECMWF operational data base (ECMWF). The ground albedo distribution is extracted from the seasonal albedo data base (Matthews 1983). High precision integrated Albedo data of resolution of $1° \times 1°$ are available for different seasons.

The aerosol extinction profile has been taken from the ECSTRA (Extinction Coefficient for STRatospheric Aerosol) model which depends on altitude, latitude and wavelength parameters and can be used as input in the retrieval procedure (Fussen und Bingen 1999). This empirical model of aerosol extinction profiles is based on SAGE II solar occultation measurements.

4.2.7 Error Characterization

A detailed account of the error budget for V 2.9 can be found in (Rahpoe, et al. 2013). A full error budget estimation of V3.5 is not available yet, and has to be characterized in the near future. The random error (ex-ante) for the V3.5 ozone is in the range of 2-5 %.

4.3 GOMOS ESA IPF v6 and ALGOM2S v1.0 (FMI)

The GOMOS (Global Ozone Monitoring by Occultation of Stars) instrument UV-VIS-IR spectrometers for monitoring of ozone and other trace gases in the atmosphere (Bertaux, et al. 2010; Kyrölä et al., 2010). Ozone is retrieved from UV-VIS measurements. The night-time

measurements will be used in the Ozone-CCI project. The GOMOS IPF v.6 processing is described in detail in (Kyrölä et al., 2010); the new feature of v.6 processing (compared to the previous versions), the "full-covariance-matrix" inversion, is presented in (Sofieva et al., 2010). Below we present the brief summary of GOMOS retrieval algorithm and data characterization.

4.3.1   GOMOS retrieval strategy

The GOMOS processing starts with various instrumental corrections, which are described in detail in (Kyrölä et al., 2010). First, the mean dark current is subtracted from the recorded spectra S_{obs}. Second, the reference star spectrum is averaged from sufficiently many measurements above the atmosphere, thus giving an accurate estimate of the star spectrum S_{star}. Then the spectrum observed through the atmosphere is divided by the reference spectrum, yielding the atmospheric transmission function:

$$T_{atm} = \frac{S_{obs}}{S_{star}}.$$

Eq.   4.23

The component due to refractive effects is estimated and removed from the transmission data:

$$T_{ext} = \frac{T_{atm}}{T_{ref}}.$$

Eq.   4.24

The component T_{ref} includes estimates of both regular refractive effects (refractive attenuation, or dilution) and scintillations (Dalaudier et al., 2001), (Sofieva et al., 2009). The transmission spectra T_{ext} provide the basis for retrieval of atmospheric constituent densities. The collection of transmission spectra at different tangent altitudes constitutes the GOMOS measurements written in matrix form as **Y**. The transmission spectra can be modelled by using the well-known Lambert-Beer law:

$$T_{ext} = e^{-\tau},$$

Eq.   4.25

where the optical depth τ is given by:

$$\tau(\lambda) = \sum_{j} \int \sigma_j(\lambda, \mathrm{T}(\overline{r}(s))) \rho_j(\overline{r}(s)) ds.$$

Eq.   4.26

Here the ρ_j's are constituent densities depending on the position $\overline{r}$ and the σ_j's are the temperature-dependent absorption or scattering cross sections (λ being wavelength). The integration is performed along the optical path joining the instrument and the source.

Ozone, NO_2, NO_3 and aerosol optical depth are retrieved from the UV-VIS spectrometer measurements. Since aerosol extinction spectrum is not known a priori, a second-degree polynomial model is used for the description of the aerosol extinction. The aerosol number density and two parameters that determine the wavelength dependence of aerosol extinction spectra are retrieved from GOMOS data. Due to non-orthogonality of cross-sections of Rayleigh scattering by air with the considered polynomial model of aerosol extinction, the air

density is not retrieved from UV-VIS measurements by GOMOS. It is taken from ECMWF analysis data corresponding to occultation locations.

The GOMOS inversion from UV-VIS spectral measurements is split into two steps (Kyrölä et al., 1993; Kyrölä et al., 2010). First, atmospheric transmission spectra are inverted into horizontal column densities N for gases and optical thickness for aerosols, for every ray perigee (tangent) altitude h (spectral inversion). Then, for every constituent, the collection of the horizontal column densities at successive tangent heights is inverted to vertical density profiles (vertical inversion). The use of the effective cross sections (Sihvola, 1994; Kyrölä et al., 2010) allows the separation of the inversion problem into two parts. The two parts are, however, coupled together by the unknown effective cross sections. In order to take into account the coupling effect, the processing makes use of an iterative loop over spectral and vertical inversions.

4.3.2 Spectral inversion

The GOMOS spectral inversion problem can be written in the form:

$$\boldsymbol{T}_{ext} = \exp(-\Sigma N) + \varepsilon \ ,$$

<div align="right">Eq. 4.27</div>

where $\boldsymbol{T}_{ext}$ are measured transmittances after the correction of refractive effects at altitude h ($\boldsymbol{T}_{ext}$ are the columns of the measurements matrix $\mathbf{Y}$), N are horizontal column densities at this altitude, Σ is the matrix of effective cross-sections, and ε represents the error term (noise and modeling errors). The spectral inversion is performed for each tangent altitude separately (i.e., independently of other tangent altitudes). It relies on the standard maximum likelihood method, which is equivalent to minimization of the χ^2 statistics under the assumption of a Gaussian distribution of the measurement errors:

$$\chi^2 = \left(\boldsymbol{T}_{ext} - \boldsymbol{T}_{mod}(\boldsymbol{N})\right)^T \mathbf{C}^{-1}\left(\boldsymbol{T}_{ext} - \boldsymbol{T}_{mod}(\boldsymbol{N})\right),$$

<div align="right">Eq. 4.28</div>

where $\boldsymbol{T}_{ext}$ is a vector of observed transmission spectra, $\boldsymbol{T}_{mod}$ is a vector of modeled transmittances, and $\mathbf{C}$ is the covariance matrix of transmission errors. The minimization of χ^2 is performed using the Levenberg-Marquardt algorithm (Press, 1992), which provides both horizontal column densities N and a covariance matrix of their uncertainties $\mathbf{C}_N$. In χ^2 presentation, the covariance matrix of the transmission errors $\mathbf{C}$ is presented as a sum of two matrices:

$$\mathbf{C} = \mathbf{C}_{noise} + \mathbf{C}_{mod},$$

<div align="right">Eq. 4.29</div>

where the diagonal matrix $\mathbf{C}_{noise}$ corresponds to the measurement noise and $\mathbf{C}_{mod}$ corresponds to the modeling error. The incomplete scintillation correction is the dominating source of modeling errors in the stratosphere. The scintillation correction errors are not correlated at different tangent altitudes, thus allowing the splitting of $\mathbf{C}$ into $\mathbf{C}_{noise}$ and $\mathbf{C}_{mod}$. They result in wavelength-dependent perturbations in the transmission spectra, therefore $\mathbf{C}_{mod}$ is essentially non-diagonal, its parameterization is presented in (Sofieva et al., 2009). The efficient numerical solution of the problem to minimize the χ^2 with the modelling error included is presented in (Sofieva et al., 2010). It has been shown that the normalized χ^2-values are close to unity (Sofieva

et al., 2010). This ensures that the applied parameterization of scintillation correction errors adequately describes the main source of modeling errors for altitudes ~20-50 km. At the same time, this allows us to expect that the uncertainties of retrieved profiles are characterized properly.

4.3.3 Vertical inversion

The vertical inversion aims to determine a vertical profile $x(z)$ that fulfils the equation:

$$N(z) = \int x(z(s))ds \,,$$

Eq. 4.30

where N is any of the horizontal column densities inverted in the spectral inversion and the integration is performed along the ray path. The problem is discretized by dividing the atmosphere into layers (the number of layers is set equal to the number of measurements in the occultation processed) and assuming the local densities to be linear functions of altitude between two successive GOMOS measurements. The vertical inversion in the matrix form can be written as

$$\mathbf{N} = \mathbf{K}\mathbf{x} + \boldsymbol{\varepsilon}_N \,,$$

Eq. 4.31

where $\mathbf{K}$ is the forward model (kernel) matrix, $\mathbf{N}$ is a vector of measurements (horizontal column densities), $\mathbf{x}$ is a vector of unknowns (profile) and $\boldsymbol{\varepsilon}_N$ is a vector of horizontal column densities uncertainties. The vertical inversion is stabilized by Tikhonov-type regularization according to the target resolution (Sofieva et al., 2004; Tamminen et al., 2004; Kyrölä, Tamminen, et al. 2010), which makes the vertical resolution practically independent of angles between the orbital plane and the direction to the star.

The target-resolution Tikhonov solution of $\mathbf{N} = \mathbf{K}\mathbf{x} + \boldsymbol{\varepsilon}_N$ is given by:

$$\hat{\mathbf{x}} = (\mathbf{K}^T\mathbf{K} + \alpha\mathbf{H}^T\mathbf{H})^{-1}\mathbf{K}^T\mathbf{N},$$

Eq. 4.32

where the regularization matrix $\mathbf{H}$ is:

$$\mathbf{H} = \mathrm{diag}\left[\frac{1}{h_i^2}\right]\begin{bmatrix} 0 & 0 & 0 & ... & 0 \\ 1 & -2 & 1 & ... & 0 \\ ... & ... & ... & ... & ... \\ ... & ... & 1 & -2 & 1 \\ 0 & 0 & 0 & ... & 0 \end{bmatrix}.$$

Eq. 4.33

Here $\left[\frac{1}{h_i^2}\right]$ is shorthand to dividing all matrix elements by the square of the local altitude difference. The regularization parameter α has been selected in such a way that the retrieved profiles have the desired target resolution. For ozone, the target resolution is 2 km below 30 km and 3 km above 40 km (with smooth transition between 30 and 40 km).

Since the vertical inversion is linear, the uncertainty of the retrieved profile $\hat{x}$ is estimated through the standard error propagation.

4.3.4   GOMOS Level 2 ozone profiles and their characterization

The Level 2 GOMOS files provide ozone number density profiles on tangent-altitude grid. This grid depends of obliquity of occultation: the larger obliquity, the denser grid. The actual vertical resolution of GOMOS ozone profiles is the same in all occultations: 2 km below 30 km and 3 km above 40 km. Exemplary averaging kernels are shown in Figure 4.4. Difficulties in retrievals (absence of convergence etc) are indicated by flags (zero when the data are valid). The quality of the retrievals is indicated also by the normalized χ^2-statistics and residuals written in the „Residual extinction" products.
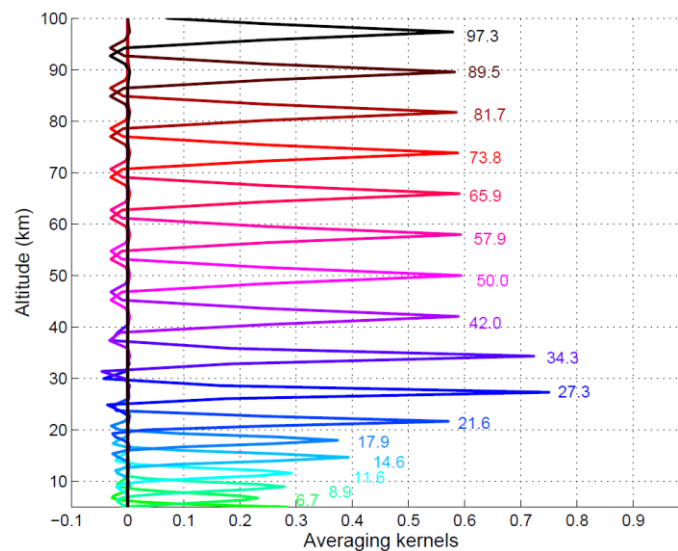.

Figure 4.4: Examples of averaging kernels for ozone. The averaging kernels peak at the altitude they correspond (given in the figure in km). Note that only every 5th averaging kernel is plotted.

4.3.5   Error characterization

The error estimates (square roots of the diagonal elements of the covariance matrix) are provided in the Level 2 files and the part of the covariance matrix (7 off-diagonal elements). The covariance matrix of retrieved profiles uncertainties is obtained via Gaussian error propagation through the GOMOS inversion (see (Tamminen et al., 2010) for details). As indicated above, both noise and the dominating random modelling error are taken into account on GOMOS inversion. Thus, error estimates provided in Level 2 files, represent the total precision estimates. The precision of GOMOS ozone profiles depends on stellar brightness, spectral class and obliquity of occultation. Typical values of ozone precision values based on real GOMOS data are presented in Figure 4.5.
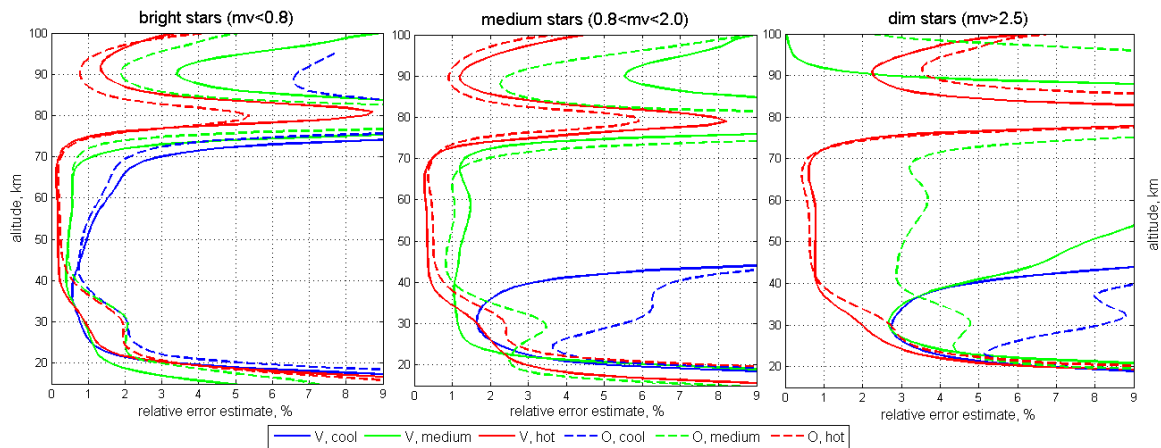
Figure 4.5: GOMOS precision estimates of ozone for representative cases: bright star (first column), typical star (middle column) and dim star (last column). The dashed lines correspond to oblique occultations (O) and the solid lines to vertical (in orbit).

Other sources of systematic errors are imperfect modelling of the aerosol extinction, uncertainties in the absorption cross sections and temperature. Uncertainties of air density profile, ray tracing and potentially missing constituents have a negligible impact on ozone retrievals. The characteristics of GOMOS ozone profiles together with the random and the systematic errors are summarized in Table 16.

Table 16: GOMOS ozone profiles characteristics and error budget

Altitude range	15-100 km
Vertical resolution	2 km below 30 km, 3 km above 40 km
Random errors: measurement noise and scintillations	0.4-4% stratosphere, 2-10 % MLT, ~10% at 15 km
Systematic errors: Uncertainty in cross-sections Aerosol model selection Temperature uncertainty Air density uncertainty	~1 % ~20% below 20 km, 1-5% at 20-25 km, <1% above 25 km <0.5% at 30-60 km, negligible elsewhere <1% below 20 km, negligible elsewhere

4.3.6   GOMOS ALGOM2s v1.0 processor

The ALGOM2s v1.0 processor (Sofieva et al., 2017a) is developed at FMI in the framework of ESA project ALGOM (GOMOS Level 2 evolution studies). The ALGOM2s processing algorithm is optimized in the UTLS and uses IPF V6 advantages in the middle atmosphere. The ozone retrievals in the whole altitude range from the troposphere to the lower thermosphere are performed in two steps, as in the operational algorithm: spectral inversion followed by the vertical inversion. The spectral inversion is enhanced by using a DOAS-type method at visible wavelengths for the UTLS region. This method uses minimal assumptions about the atmospheric profiles. The vertical inversion is performed as in IPF v6 with the Tikhonov-type regularization according to the target resolution.

The GOMOS ALGOM2s dataset not only has improved data quality in the UTLS compared to IPF v6, but it is also expected to be more stable in the whole atmosphere due to an advanced screening of unreliable data (Sofieva et al., 2017a).

4.4 OSIRIS/ODIN 5.01 (University of Saskatchewan)

The Level 2 Odin/OSIRIS 5.01 processor retrieves ozone number density profiles from Level 1 limb scattered sunlight as measured by the Canadian built OSIRIS instrument aboard the Swedish spacecraft Odin. Data is available from November 2001 to present and details concerning the processor may be found in (Degenstein 2009).

4.4.1 Basic Retrieval Equations

The processor employs the SaskMART iterative solution outlined in detail in (Degenstein 2009). This algorithm finds the *i+1* estimate of the state parameter from the previous estimate following the equation:

$$x_{i+1,j} = x_{i,j} \sum_{m,l} W_{m,j,l} \frac{\tilde{y}_{m,l}}{\tilde{f}_{m,l}(\boldsymbol{x_i}, \boldsymbol{u})}$$

Eq. 4.34

Here:

- $x_{i,j}$ is the jth element of a vector of unknown parameters estimated on *i*-th iteration

- $\tilde{y}_{m,l}$, is the lth element of the mth vector of dimensionless observation parameters defined below. Each vector is constructed from the OSIRIS radiances at a specific set of wavelengths meant to be sensitive to the state parameter at different altitudes.

- $\tilde{f}_{m,l}(\boldsymbol{x_i}, \boldsymbol{u})$, is the lth element of the mth vector of simulated dimensionless observation parameters obtained through the forward model SASKTRAN.

- $W_{m,j,l}$ is an element of the mth weighting matrix defining the influence of the lth element of the mth observation vector on the jth element of the state parameter.

The initial estimate of *x* is taken from a standard climatology. The retrieval vector, and simulated retrieval vector produced by the forward model can be calculated with the following equations:

$$\tilde{y}_{m,l} = \sum_{\lambda} \alpha_{m,\lambda} \log(y_{l,\lambda}/y_{ref,\lambda})$$

$$\tilde{f}_{m,l}(\boldsymbol{x}, \boldsymbol{u}) = \sum_{\lambda} \alpha_{m,\lambda} \log(f_{l,\lambda}(\boldsymbol{x}, \boldsymbol{u})/f_{ref,\lambda}(\boldsymbol{x}, \boldsymbol{u}))$$

Eq. 4.35

Here:

- $\alpha_{m,\lambda}$ is a coefficient corresponding to a wavelength that contributes to the m$^{\text{th}}$ vector where $\sum_{\lambda} \alpha_{m,\lambda} = 0$

- $y_{l,\lambda}$, is the lth element of the OSIRIS radiances at a wavelength λ

- $f_{l,\lambda}$, is the lth element of the simulated radiances produced by SASKTRAN at a wavelength λ

- $y_{ref,\lambda}$ and $f_{ref,\lambda}$ are the radiance values at a reference altitude.

4.4.2 Diagnostics

The Level 2 Odin/OSIRIS 5.01 ozone data product is currently not accompanied by error characterization. However, the error due to measurement noise is being generated and will be included in version 5.0x slated for release in 2011. It is anticipated that the details of this error characterization will be published shortly and they are summarized below.

A covariance matrix for each retrieval vector, $\boldsymbol{S}_{ym}$, is calculated from the OSIRIS measurement noise using standard error propagation techniques, resulting in a set of diagonal matrices.

A kernel matrix $\mathbf{K}_m$ serves to map the error in the state parameter to the error in the mth observation vector. This is approximated by perturbing the retrieved state parameter by a small amount (δx) and using it as a forward model input. Each element of a kernel matrix is defined as:

$$K_{m,j,l} = \frac{\partial \tilde{y}_{m,j}}{\partial x_l} \qquad \text{Eq. 4.36}$$

$$K_{m,j,l} \approx \frac{\tilde{f}_{m,j}(x+\delta x_{(l)},u)-\tilde{f}_{m,j}(x,u)}{\delta x} \qquad \text{Eq. 4.37}$$

Where we define a perturbation array as

$$\delta \boldsymbol{x}_{(l)} = \begin{cases} \delta x & at\ l \\ 0 & otherwise \end{cases}$$

The inverse of a kernel matrix then will map the mth observation vector's covariance to a covariance in x attributed to y_m:

$$S_{xm} = K_m^{-1} S_{ym} [K_m^{-1}]^T \qquad \text{Eq. 4.38}$$

The covariance contributions from each vector are combined using the weighting matrices following the equation:

$$S_{x,j,l} = \sum_{m,k} (W_{m,j,k})^2 S_{xm,k,l} \qquad \text{Eq. 4.39}$$

In addition to this error characterization, version 5.0x of the Odin/OSIRIS data products will flag and remove profiles where circumstances are likely to invalidate the retrieval. For example, profiles are flagged where radiation hits were detected on relevant pixels of the OSIRIS CCD, where high altitude clouds seem to be interfering with the retrieval, and where unphysical values have been retrieved.

Errors due to modelling parameters like neutral density and temperature are all on the order of a few percent. Because Odin was designed to serve as an astronomy experiment as well the pointing is quite good and with the latest corrections from the Swedish Space Corporation the largest pointing errors are likely a couple hundred metres. As described below NO_2 and albedo are model parameters for the ozone retrieval, but these are themselves retrieved and pose little concern.

Version 5.0x, for release in 2011, will also have an improved estimate of the OSIRIS spectral point spread function, decreasing its associated parameter error. Future versions of the Odin/OSIRIS ozone data products will also make use of more accurate scattering properties of ice crystals and sulphate aerosols. This will improve retrievals where high altitude cirrus, volcanic activity, or other issues may be affecting aerosols in the UTLS region.

4.4.3   Assumptions, grid and discretization

The Odin/OSIRIS 5.01 processor retrieves ozone profiles from Odin/OSIRIS limb scattered spectra. The retrieval algorithm is based on forward modelling of limb radiances.

The forward model, SASKTRAN, constructs an atmosphere of spherical shells of variable thickness, typically with 1km vertical spacing, from 0 to 100km in altitude. Ozone is retrieved between 10 km, or the altitude of the cloud top if this is higher, to 60km. The retrieval quantity is ozone number density (nd).

SASKTRAN uses successive orders of scattering propagating rays in discrete directions from a set of points distributed throughout the atmosphere. The resolutions of all of these discretization are customizable and in the Odin/OSIRIS 5.01 processor the resolutions are all sufficiently high such that increasing the resolution does not produce significant changes in either the simulated OSIRIS observations or the retrieved ozone profiles.

4.4.4   Sequence of operations

Interfering variables are first retrieved to remove their influence. These include sulphate aerosol, effective albedo, and NO_2. Each set of retrieved parameters is used in subsequent parameter retrievals for a given scan. The sulphate aerosol profile is available as an Odin/OSIRIS Level 2 data product and the retrieved albedo is included with both ozone and sulphate aerosol data as ancillary information.

4.4.5   Regularization

The Odin/OSIRIS 5.01 retrieval processor imposes no smoothness or regularization criteria during the retrieval.

4.4.6   Iterations and convergence

The SaskMART retrieval algorithm is iterated 15 times and has no convergence criteria. It has been observed that for well behaved data SaskMART easily achieves convergence by then as demonstrated in (Roth, et al. 2007).

4.4.7   Ozone Retrieval Vector Definitions

The ozone retrieval uses sets of 2 or 3 OSIRIS pixels to construct the retrieval vectors, using the Chappuis band at low altitudes and Huggins band higher. These vectors are sensitive at

various altitudes and are applied at different altitudes. The wavelengths corresponding to the pixels in use at varying altitudes are shown in the table below:

Table 17: wavelengths corresponding to OSIRIS pixels in use at different altitudes.

	$\tilde{y}_1$	$\tilde{y}_2$	$\tilde{y}_3$	$\tilde{y}_4$	$\tilde{y}_5$	$\tilde{y}_6$	$\tilde{y}_7$	$\tilde{y}_8$
Definition	Triplet	Pair	Pair	Pair	Pair	Pair	Pair	Pair
Absorbing Wavelength [nm]	602.39	292.43	302.17	306.06	310.7	315.82	322.00	331.09
Reference Wavelength 1 [nm]	543.84	350.31	350.31	350.31	350.31	350.31	350.31	350.31
Reference Wavelength 2 [nm]	678.85	-	-	-	-	-	-	-
Minimum Altitude [km]	1	47	42	40	37	31	24	18
Maximum Altitude [km]	28	57	53	49	46	44	40	37
Normalization Altitude	29	58	54	50	47	45	41	38

4.4.8   Explicit Error Budget

To estimate the OSIRIS ozone error budget a random sampling of scans were chosen and the ozone was repeatedly retrieved with randomly perturbed inputs. The inputs were adjusted by a random factor chosen from a normal distribution of values with a 3σ of 10%. This was performed in turn for the aerosol profile, albedo, neutral density profile, and NO_2 profile. For the altitude registration a 3σ of 300m was used. The precision was calculated using a method described by Dr. A.E. Bourassa in a forthcoming JGR paper using the uncertainty in the OSIRIS radiance measurements. The total error shown in the figure above is calculated using a sum in quadrature of the error components.

Error! Reference source not found. illustrates the dominance of the precision over the total error budget, which peaks around 7% at approximately 15km. This is followed by contributions from potential errors in altitude registration, which provides about 2% uncertainty above 35km and below 20km. Errors in the neutral density potentially contribute up to 2% uncertainty at the lowest bounds of the retrieval and are negligible above 30km. Errors from the other sources are much less than 1% at all altitudes.
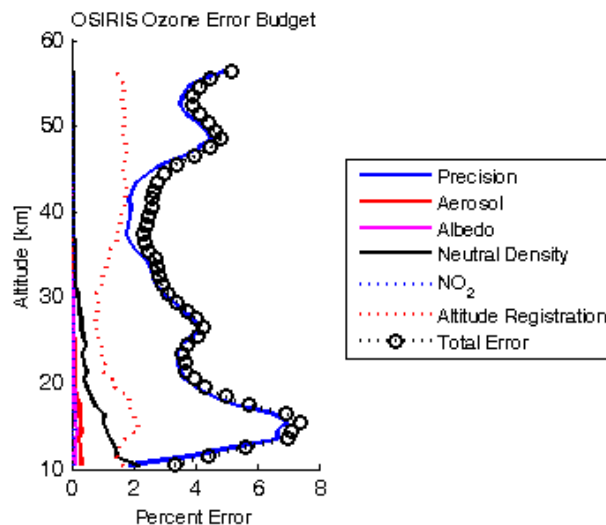
Figure 4.6: Dominance of the precision over the total error budget of OSIRIS.

4.5   SMR/ODIN (U. Chalmers)

4.5.1   Ground segment processing

The Sub-Millimetre Radiometer (SMR) on board the Swedish-led Odin satellite makes vertically resolved ozone measurements since 2001 (Murtagh, et al. 2002). The instrument and technique is described by (Frisk, et al. 2003). Calibrated spectra (level-1b) are produced from the SMR raw data and the reconstructed attitude data of the satellite (level-0) at the Onsala Space Observatory of the Chalmers University of Technology (Gothenburg, Sweden). Detailed information on level-1 data processing is given by (Olberg, et al. 2003). The Chalmers University of Technology (Gothenburg, Sweden) is also in charge of the operational retrieval of vertical profiles from the spectral measurements of a limb scan (level-2 processing) (Urban, Lautié, et al. 2005) (Urban, Murtagh, et al. 2006). Odin/SMR level-2 data are made available to the user at http://odin.rss.chalmers.se.

4.5.2   Forward and retrieval models

Vertical profiles are retrieved from the spectral measurements of a limb scan by inverting the radiative transfer equation for a non-scattering atmosphere. Retrieval algorithms based on the Optimal Estimation Method (OEM) (C. Rodgers 1976), a linear inversion method using statistical a priori knowledge of the retrieved parameters for regularization, were developed for the ground segment of Odin/SMR (Urban, Baron, et al. 2004) (Eriksson, Jiménez und Buehler 2005)

The Swedish level 1b to level-2 processor Qsmr is aiming at fast operational data analysis. The employed retrieval model Qpack (Eriksson, Jiménez und Buehler 2005) is built around the Atmospheric Radiative Transfer Simulator (ARTS), developed conjointly at the Chalmers University of Technology (Gothenburg, Sweden) and the University of Bremen (Germany) (Buehler, et al. 2005). The forward model includes modules for spectroscopy (line-by-line calculation, water vapor and dry air continua) and radiative transfer (including refraction). It also allows the computation of differential weighting functions (Jacobians) needed for the inversions. Sensor characteristics (antenna, sideband, spectrometer) are taken into account by a separate module following the forward calculations (Eriksson, Ekström, et al. 2006). The forward model, the sensor model, and an inversion module based on the Optimal Estimation Method are implemented within a Newton Levenberg-Marquardt iteration scheme.

In addition to Qpack/ARTS, the Qsmr level-2 processor includes also the modular 1-d forward and retrieval code for the millimeter and sub-millimeter wavelengths range MOLIERE-5 (Microwave Observation LIne Estimation and REtrieval, version 5, (Urban, Baron, et al. 2004)) which is based on the same methods and principles as Qpack/ARTS. A systematic comparison of the forward models ARTS and MOLIERE-5 used within the Odin/SMR level-2 processors resulted in an excellent agreement of the different modules for spectroscopy, radiative transfer and instrument modeling (Melsheimer, et al. 2005).

4.6   ACE-FTS V3.5 (U. Toronto)

The retrieval methods used for the Atmospheric Chemistry Experiment Fourier-Transform Spectrometer are explained in detail by (Boone et al., 2005). Retrieval methods relating to the

version 3.0 ozone profiles have been described by (Boone et al., 2013). ACE-FTS version 3.0 ozone profiles were restricted to dates between March 2004 and September 2010 due to problems with the *a priori* pressure and temperature. This is also discussed by (Boone et al., 2013) along with the plans for the version 3.5 reprocessing.

4.6.1 Retrieval

The ACE-FTS v3.5 temperature and VMR retrievals are described in detail by Boone et al. (2005; 2013]). The following description is taken from those papers. For ACE-FTS processing, CO_2 is analyzed to determine pressure. A crucial aspect of the pressure and temperature retrieval process is pointing knowledge. No information from sensors onboard the satellite (other than a clock) is used in the computation of tangent altitudes. The current approach treats tangent altitudes as unknown parameters in the pressure/temperature retrievals. Rather than fitting the entire spectrum, we analyze microwindows that contain spectral features from a molecule of interest with minimal spectral interference from other molecules. For some molecules it is not possible to find a comprehensive set of microwindows free from significant interferences. Thus the VMR retrieval software allows for retrieval of multiple molecules simultaneously. All retrievals employ a modified global fit approach (Carlotti, 1989), in which all parameters are determined simultaneously with the Levenberg–Marquardt (Press et al., 1992) nonlinear least-squares method. The wavenumber calibration for the ACE-FTS is not reliable, and cross-correlation is used to align the measured and calculated spectra. Without a strong spectral feature to guide the cross-correlation process, spectral features near the noise limit can end up being aligned with a strong noise feature. Where no strong interfering line was available for microwindows containing weak spectral features of the target molecule, the wavenumber shifts at the highest altitudes within the micro window were constrained to match the wavenumber shifts determined at lower altitudes within that same micro window, where the signal from the target molecule was stronger, thereby allowing an accurate determination of wavenumber shift via cross correlation.

4.6.2 Spectral analysis

Calculating spectra (for least-squares fitting) must invoke a parameterized model of the Earth's atmosphere. For the effective sea level as a function of latitude we adopt the ellipsoid model from the World Geodetic System 1984 (WGS 84; WGS 84 (1998)). The acceleration due to gravity at sea level as a function of latitude is derived from the WGS 84 model. In order to keep calculations analytical (including derivatives for the least-squares process), the variation in acceleration due to gravity with altitude is approximated as a linear function, accurate to within a tenth of a percent in the altitude range of interest. By virtue of its long atmospheric lifetime, CO_2 is well-mixed and has a nearly constant VMR over much of the middle atmosphere. At high altitudes, photodissociation and diffusion reduce the VMR. The altitude above which the CO_2 VMR drops off varies with season and location, typically 80–90 km but extending below 60 km during the polar winter at extreme latitudes. To account for the increase in CO_2 VMR as a function of time, we adopt the equation used by the Halogen Occultation Experiment (HALOE):

$$CO_2 \text{ VMR (ppm)} = 326.909 + 1.50155(t - t_0), \quad t_0 = 1 \text{ Jan 1977,} \qquad \text{Eq. 4.40}$$

in which $t - t_0$ is time in years. No provisions are made for variations with location or season. At high altitudes the CO_2 VMR cannot be readily determined from a priori information. However, there are no features (such as significant refraction or optically thick clouds) that affect instrument pointing in this altitude region, and so tangent heights can be reliably calculated from geometry, from knowledge of the relative positions of the Sun, Earth, and satellite. This requires an accurate characterization of the satellite's orbit and an accurate measure of time. Note that there is a known systematic problem with ACE-FTS measurement times. The absolute values for time stamps are not considered reliable, but differences between time stamps are presumed accurate. As a consequence, only the spacing between calculated tangent heights is reliable. Absolute tangent heights in this altitude region are determined through the registration procedure described below.

A crossover measurement is taken as the third measurement greater than 43 km and is typically around 50 km. An analysis extends from the crossover to as high as 120 km. For each measurement there are four potential variables (P, T, VMR, and tangent height z) that must be either fixed or fitted. The data support at most two unknowns per measurement for least-squares fitting (two because there is information from both the absolute and relative intensities of the lines). In the high-altitude region the set of fitting parameters includes $1/T$ for each measurement. However, the region requires only one parameter for pressure: P_c, the pressure at the crossover measurement. From this single parameter (and values for tangent height and temperature at each measurement) the pressures for all other measurements in this region are calculated by integrating upward from the crossover measurement, using:

$$P(z') = P_3 \exp\left[-\frac{g_0}{k}\int_{z_3}^{z'} m_a(z)\left(1 - \frac{2z}{R_e}\right)\left(\frac{(z-z_2)(z-z_3)}{(z_1-z_2)(z_1-z_3)}\frac{1}{T_1}\right.\right.$$
$$\left.\left. + \frac{(z-z_1)(z-z_3)}{(z_2-z_1)(z_2-z_3)}\frac{1}{T_2} + \frac{(z-z_1)(z-z_2)}{(z_3-z_1)(z_3-z_2)}\frac{1}{T_3}\right)dz\right]$$

Eq. 4.41

where g_0 is acceleration due to gravity at sea level, k is Boltzmann's constant, $m_a(z)$ is the atomic mass of air, and R_e is the effective radius of the Earth at a given latitude (determined from the WGS 84 model). In the altitude range between the crossover and ~70 km the CO_2 VMR is fixed. Above this the CO_2 VMR is fitted. CO_2 VMR for the highest analyzed measurement is determined by using a least-squares fitting with P and T fixed to NRL-MSISE-00 (Picone et al., 2002) values. With the expectation that CO_2 VMR at high altitudes does not exhibit sharp structure, an empirical function is used to reduce the number of fitting parameters:

$$CO_2\ VMR(z) = \frac{VMR_{strat} + a(z-z_0) + b(z-z_0)^2 + c(z-z_0)^3}{1 + d(z-z_0) + e(z-z_0)^2},$$

Eq. 4.42

where VMR_{strat} is the assumed stratospheric value for CO_2 and z_0 is taken as the highest tangent height for which CO_2 VMR is assumed constant. The CO_2 VMR is assumed constant as high as 75 km for latitudes less than 60° and 65 km for latitudes greater than 60°. A Padé approximant form (the ratio of two polynomials) is used in Eq. 4.42 because it requires fewer parameters

than a straight polynomial, and the extrapolation beyond the fitting region is better. CO_2 VMR at the first measurement below the crossover is also included as a fitting point in the least-squares analysis, in order to ensure the slope near the crossover is at least roughly correct, generating a smooth transition between the fixed portion and the retrieved portion of the CO_2 VMR profile. The portion of the CO_2 VMR profile above the highest analyzed measurement (i.e., between ~125 and 150 km) is fixed to a constant, to the value calculated from the empirical function in the tangent layer of the highest analyzed measurement.

4.6.3   Retrieval grid

The calculation grid adopted for the ACE-FTS analysis is divided into 150 layers of 1 km thickness. Each layer is assumed to have a constant temperature, pressure, and VMR for a given molecule with no consideration of horizontal gradients within a layer. Diurnal corrections are not currently applied, although diurnal effects are likely to be significant for photosensitive molecules such as NO_2. The raw wavenumber spacing for the ACE-FTS spectra is 0.02 cm^{-1}. To achieve accurate results for the narrow lines found at high tangent altitudes, forward model calculations are performed on a much finer grid, with a wavenumber spacing reduced by a factor of 16. The forward model for ACE-FTS is the same radiative-transfer model used for ATMOS with some notable exceptions: (1) ACE-FTS forward model calculations employ the HITRAN 2004 line list and cross sections (with updates noted in Boone et al. (2013)). (2) Partition functions for the ACE-FTS forward model are calculated from the total internal partition sums (TIPS) approach (Fischer et al., 2003). (3) The Voigt line-shape function is calculated from the Humlicek algorithm (Kuntz, 1997; Ruyten, 2004) rather than from a lookup table. (4) No apodization is used for the ACE-FTS instrumental line shape (ILS). (5) The ILS for the ACE-FTS requires an empirical adjustment to account for self-apodization effects beyond the normal field of view contribution.

The finite scan time of an FTS imposes a lower limit on the width of spectral features measured by the instrument. The instrument line shape (ILS) of an FTS is primarily governed by this finite scan time but will also include the effects of any deviations from an ideal instrument, such as off-axis rays from a finite field of view or changes in the modulation efficiency of the FTS mirrors as a function of optical path difference (Davis et al., 2001). The ILS is defined as the Fourier transform of the modulation function (MF), which can be written as follows:

$$MF(\nu, x) = F_{clip}(x)\eta(\nu, x)\frac{\sin\left(\frac{1}{2}\pi r^2 \nu x\right)}{\frac{1}{2}\pi r^2 \nu x},$$ **Eq. 4.43**

where x is optical path difference in cm, ν is wavenumbers in cm^{-1}, and r is the radius in radians of the instrument's circular field of view. The term F_{clip} is a rectangular function associated with the finite scan time of the instrument. It is 1 for x between $\pm$ 25 cm (the maximum optical path difference for the ACE-FTS) and 0 otherwise. The third term in Eq. 4.43, with the form sinx/x, represents the effect of a finite field of view, accounting for the broadening of spectral lines that arise from off-axis rays in the instrument. The middle term in Eq. 4.43, η, represents any apodization applied to the measurements (other than the sinx/x term associated with off-axis rays). The finite scan time imparts a "ringing" effect to spectral features measured by the FTS, generating side-lobes when the width of a spectral feature is less than the width of the ILS.

Apodization is a process that reduces the abruptness of the transition near ± 25 cm in F_{clip}, which decreases the amplitude of the side lobes at the expense of a broader ILS. There are also inherent instrumental effects that can cause the modulation function to vary with optical path difference. This is known as self-apodization.

The ACE-FTS suffers from major self-apodization of unknown origin. It is necessary to include an empirical function in η in the equation above in order to properly reproduce the ACE-FTS ILS. Otherwise, it is impossible to derive accurate information on the atmosphere from the ACE-FTS measurements. For this data version, a study of the ACE-FTS ILS determined that a particular shape of the empirical function for self-apodization provided a significant improvement in fitting residuals: a gradual decrease in the modulation function with increasing $|x|$ (i.e., increase in the absolute value of optical path difference), combined with a sharp decrease of the modulation function for optical path difference near maximum path difference (± 25 cm). An expression was selected that reproduced this behaviour with a minimum number of parameters:

$$\exp(1) \times \exp\left[-exp\left(\frac{ax^{10}}{1+bx^{10}}\right)\right]\left(1 - c\frac{x}{25}\right). \qquad \textbf{Eq. 4.44}$$

There is nothing intrinsic about the form of Eq. 4.44; it is simply the form that gave the best residuals in the analysis of ACE-FTS spectra.

The ACE-FTS instrument has two detectors, a mercury cadmium telluride (MCT) detector that measures from 750–1810 cm^{-1}, and an Indium Antimonide (InSb) detector that measures from 1810–4400 cm^{-1}. These two detector regions were treated separately. Variation of the self-apodization effects with wavenumber was treated by using an effective field-of-view rather than true, physical internal field-of-view for the instrument (6.25 mrad diameter). The values of the empirical parameters were determined by performing a non-linear least-squares fitting using a set of microwindows that spanned as much of the wavenumber range as possible and were restricted to high altitude (above about 40 km), where the spectral features were narrow enough that the shapes of the measured lines were close to the ILS. The fitting was performed for more than 400 occultations, and average values were then calculated. For the MCT detector, the parameters were $a = 4.403 \times 10^{-16}$, $b = -9.9165 \times 10^{-15}$, $c = 0.03853$, and an effective field of view of 7.591 mrad diameter. For the InSb detector, the parameters were $a = 2.762 \times 10^{-16}$, b = -1.009×10^{-14}, c = 0.0956, and an effective field of view of 7.865 mrad diameter.

4.6.4   Ozone profiles

Ozone profiles are retrieved between altitudes of 5 and 95 km using 33 microwindows between 1027 and 1169 cm^{-1} (Hughes et al., 2014). Additional microwindows at 829, 923, 1105, 2149 and 2566 to 2673 cm^{-1} have been included to improve results for several interfering species and isotopologues below 25-45 km (Hughes et al., 2014). The tables below list the microwindows used for both ozone and the interfering species in ACE-FTS version 3.5.

Table 4.2: Microwindow list for O₃

Centre Frequency (cm⁻¹)	Microwindow Width (cm⁻¹)	Lower Altitude (km)	Upper Altitude (km)
829.03 [1]	0.50	5	21
923.16 [2]	0.80	5	25
1027.00	0.60	60	95
1028.62	1.20	60	95
1029.98	0.50	55	95
1030.75	0.80	55	95
1032.10	0.80	60	95
1033.15	0.60	60	95
1034.55	0.80	60	95
1049.38	0.80	55	95
1050.30	0.60	70	95
1051.20	1.00	60	95
1053.25	1.20	55	95
1054.15	0.60	70	95
1054.92	0.50	45	95
1056.75	0.50	45	60
1057.75	0.50	45	55
1058.12	1.20	55	95
1058.56	0.30	45	55
1059.58	0.60	45	60
1063.05	0.50	45	60
1063.90	0.45	40	60
1093.20	0.90	5	45
1097.58	0.85	5	45
1103.85	0.95	5	45
1105.20 [3]	1.22	8	20
1113.70	0.60	5	45
1123.00	0.60	5	40
1124.93	0.85	5	50
1125.80	0.80	45	55
1128.44	0.35	5	40
1129.10	1.00	35	55
1139.00	1.00	5	50
1142.17	0.70	5	50
1145.34	0.90	10	50
1168.35	0.50	5	45
2149.75 [4]	0.60	5	15
2566.22 [5]	0.26	12	21
2623.95 [6]	0.65	5	21
2672.6 [7]	0.40	12	21

[1] *Included to improve results for interferer HCFC-22 (CHF₂Cl)*

[2] *Included to improve results for interferer CFC-12 (CCl₂F₂)*

[3] *Included to improve results for interferer HCOOH*

[4] *Included to improve results for interferer N₂O isotopologues 1,2 & 3 (N₂O, N¹⁵NO & ¹⁵NNO)*

[5] *Included to improve results for interferer N₂O isotopologue 2 (N¹⁵NO)*

[6] *Included to improve results for interferer CO₂ isotopologue 3 (OC¹⁸O)*

[7] *Included to improve results for interferer H_2O isotopologue 4 (HDO)*

Table 4.3: Interfering Molecule(s) for O_3

Molecule	Isotopologue No. (Molecular Formula)	Lower Altitude Limit (km)	Upper Altitude Limit (km)
CCl_2F_2	0 (CCl_2F_2)	5	25
CHF_2Cl	0 (CHF_2Cl)	5	21
CCl_3F	0 (CCl_3F)	5	25
N_2O	1 (N_2O)	5	40
CH_4	3 (CH_3D)	5	25
CH_4	1 (CH_4)	5	35
N_2O	4 ($N_2{}^{18}O$)	5	21
N_2O	3 (^{15}NNO)	5	22
N_2O	2 ($N^{15}NO$)	5	21
HCOOH	0 (HCOOH)	5	20
H_2O	4 (HDO)	5	21
CO_2	3 ($OC^{18}O$)	5	21
CO_2	1 (CO_2)	5	45
O_3	2 ($O_2{}^{18}O$)	5	35
O_3	3 ($O^{18}OO$)	5	30

4.7   GOMOS Bright Limb V1.2 (FMI)

The GOMOS bright limb (GBL) ozone profiles are derived from the daytime measurements of scattered solar light by the GOMOS instrument on Envisat. The currect GBL Level 2 version 1.2. The data covers the years 2002-2012. Details about the retrieval method and the data quality can be found in Tukiainen et al., 2011 and Tukiainen et al., 2015.

4.7.1   Retrieval strategy

The vertical profile is retrieved using the onion peeling principle. The model atmosphere is discretized so that each GOMOS radiance measurement (at the current tangent point) corresponds to the center of a layer. Then, the spectral measurements are normalized with the first measurement below 47 km. These ratios are modeled with

$$T_i = \frac{I_{ss}}{I_m} \times R$$

Eq. 4.45

where R_i is the total scattering to single scattering ratio (from look-up table) at layer i, I_{ss} is the

single scattering radiance, and I_{ref} is the modeled reference spectrum. The ratio R_i depends only weakly on the trace gas concentrations allowing us to keep it fixed in the retrieval process. The same is assumed for I_{ref}. Thus, the modeled ratio T_i depends only on the trace gased in the single scattering term, the unknowns in the inverse problem. In the GBL retrieval, the fitted parameters are the number densities of ozone, aerosols and air. The single scattering term is calculated using a straightforward numerical intergration of the radiative transfer equation. For the calculation of I_{ref}, we use ECMWF air density and climatological values for the trace gases.

The multiple to single scattering look-up table is calculated using the Monte Carlo radiative transfer model Siro. The look-up table is a function of solar zenith and azimuth angles, wavelength, altitude, albedo, and latitude (tropics, mid-latitudes winter/summer, Arctic, Antarctic). Linear interpolation is used.

At each layer we minimize the chi square:

$$c^2 = [M_i - T_i]^T C^{-1}[M_i - T_i]$$

Eq. 4.46

Where M_i is the measured and normalized spectrum, and T_i is the corresponding modeled spectrum as explained above. The measurement error covariance C is assumed diagonal (see details in Tukiainen et al., 2011). The resulting weighted lest-squares problem is solved using the iterative Levenberg-Marquardt method. The GBL ozone profile is retrieved between 18 and 60 km using the radiances from the lower band (there are three bands in GOMOS: Central band that also measures the star signal, and one band below/above the central band).

4.7.2 Saturation and stray light

GOMOS daytime radiances are heavily affected by saturation and stray light issues. Saturation corrups significant proportion of the GOMOS pixels at altitudes below 25 km. Saturated pixels are not used in the retrieval, but if they are not correctly detected in the Level 1, they may affect the retrieved profile at the few lowermost altitudes.

Stray light is even larger problem than saturation in the GBL data. Currently, we estimate the stray light using the mean spectrum from above 100 km and subtract it from the rest of the spectra. This operation is done individually for each scan. The high-altitude estimate sufficiently removes the stray light from the visible wavelengths but it will not correct the UV band which is also affected by the stray light. We have no good understanding of the UV stray light in GOMOS, and hence we try to avoid using mostly corrupted pixels in the retrieval (see details in Tukiainen et al., 2015). However, this leads to small discontinuity in the ozone profile at around 40 km where the information about the ozone concentration gradually changes from the UV to the visible band.

4.7.3   Error characteristics

The errors of the retrieved profiles are estimated from the spectral fit. The error covariance of the retrieved gases is estimated with:

$$C_r = (J'J)^{-1}\frac{c^2}{n-p}$$

<div align="right">Eq. 4.47</div>

where J is the Jacobian at the optimum, n is the number of pixels in the spectral fit, and p is the number of fitted parameters. The term on the right hand side is the reduced chi square, correcting the error bars to be more realistic (ideally, the reduced chi square is unity). The error estimates of the trace gases are the square roots of the diagonal terms of C_r.
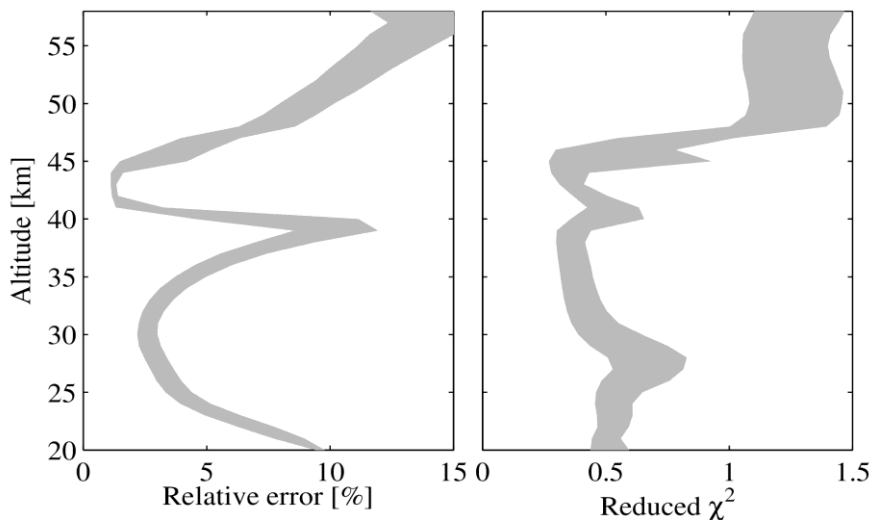
Figure 4.7: Example of the mean relative error in the GBL profiles (left) and the mean reduced chi square (right).

The vertical resolution of the GBL ozone profiles is approximately 2-3 km. The averaging kernels are not provided currently.

4.7.4   Regularization

The GBL profile retrieval does not apply any regularization, and uninformative prior is assumed for the profiles in the retrieval. Thus, the retrieved point estimator is the maximum likelihood.

4.8   U.S. Sensors

In addition to limb/occultation sensors involved in the first phase of ozone cci, four additional satellite based measurements are added, i.e., MLS on Aura, SAGE on ERBS, SABER on

TIMED, and HALOE on UARS. We give a short description of the filtering process applied before harmonization. The retrieval methods are

4.8.1 MLS V4.2

For harmonization the current MLS V 4.2 is used from L2GP at JPL. Current filtering method is used for HARMOZ_MLS profiles as recommended by the data provider:

- Only using positive precision data

- Only using data with Status= even number
- Only using data with Quality > Threshold=0.6
- Only using data with Convergence > Threshold=1.18

Because of the drift in the GPH, the calculation of the ozone number density and the geometrical grid has been performed by using the ECMWF pressure grid and temperature profiles to convert the VMR into number densities for HARMOZ_MLS. Therefore the current temperature profiles and geometrical altitude in the HARMOZ_MLS are not derived from original MLS data.

The original retrieval method with the documentation can be found by using the following link:

MLS PRODUCT

with the documentation:

Document MLS V4.2

4.8.2 SABER V2.0

For harmonization the current SABER V2.0 (Level 2A customized O3/Temperature) is used from GATTS at NASA. No filtering method have been applied for HARMOZ_SABER, except of aposteriori screening of large ozone and temperature values. Only profiles from Channel 96 micron have been used with the lowest geometrical altitude of 20 km.

The original retrieval method with the documentation can be found by using the following link:

SABER PRODUCT

with the documentation:

Document SABER

4.8.3   SAGE II V7

For harmonization the current SAGE II V 7 is used from L2GP at NASA. Current filtering method is used for HARMOZ_SAGE profiles as recommended by the data provider:

- Exclusion of all data points at altitude and below the occurrence of an aerosol extinction (386 nm and 452 nm) value of greater than 0.006 km^-1.

- Exclusion of all data points at altitude and below the occurrence of both the 525nm aerosol extinction values exceeding 0.001 km^-1 and the 525/1020 extinction ratio falling below 1.4.
- Exclusion of all data points below 35km with 200% or larger uncertainty estimate.
- Exclusion of all profiles with an uncertainty greater than 10% between 30 and 50 km

Exclusion of all data points with an uncertainty estimate of 300% or greater.

The original retrieval method with the documentation can be found by using the following link:

SAGE II website

Overview:

 SAGE II V7 document

4.8.4   HALOE V19

For harmonization the current HALOE V 19 is used from HALOE-GATS. No filtering method applied.

The original retrieval method with the documentation can be found by using the following link:

PRODUCT HALOE

The documentation with potential problems in profiles:

HALOE Document

5 Limb and occultation ozone data merging

The following ECV datasets using limb and occultation measurements have been created:

- HARMonized dataset of OZone profiles, HARMOZ (Level 2)
- Monthly zonal mean data from individual instruments (Level 3)
- Merged monthly zonal mean data (Level 3)
- Monthly mean dataset with resolved longitudinal structure (Level 3).

In addition, special UTLS and mesospheric datasets have been created.
An overview of the datasets and the methods for their creating is presented below.

5.1.1 HARMonized dataset of OZone profiles (HARMOZ)

The HARMonized dataset of OZone profiles (HARMOZ) is based on limb and occultation measurements from Envisat (GOMOS, MIPAS and SCIAMACHY), Odin (OSIRIS, SMR) and SCISAT (ACE-FTS) satellite instruments. HARMOZ consists of original retrieved ozone profiles from each instrument, which are screened for invalid data by the instrument teams. While the original ozone profiles are presented in different units and on different vertical grids, the harmonized dataset is given on a common vertical grid in netcdf-4 format. The Ozone_cci pressure grid corresponds to vertical sampling of ~1 km below 20 km and 2-3 km above 20 km. The vertical range of the ozone profiles is specific for each instrument, thus all information contained in the original data is preserved. Provided altitude and temperature profiles allow the representation of ozone profiles in number density or mixing ratio on a pressure or altitude vertical grids. Geolocation, uncertainty estimates and vertical resolution are provided for each profile. For each instrument, optional parameters, which are related to the data quality, are also included.

For convenience of users, tables of biases between each pair of instruments for each month, as well as bias uncertainties, are provided. These tables characterize the data

consistency and can be used in various bias and drift analyses, which are needed, for instance, for combining several datasets to obtain a long-term climate dataset.

The detailed description of the HARMOZ data can be found in (Sofieva, Rahpoe, et al. 2013). The dataset is available at http://dx.doi.org/10.5270/esa-ozone_cci-limb_occultation_profiles-2001_2012-v_1-201308.

The information about the datasets included in the original version of the HARMOZ (2013) is collected in Table 5.1.

Table 5.1 Information about the original (2013) HARMOZ dataset (pressure-gridded).

Instrument/ satellite	Level 2 processor	Years	Vertical range
MIPAS/Envisat	KIT/IAA V5R_O3_220/221	2005-2012	400 – 0.05 hPa
SCIAMACHY/Envisat	UBr v2.9	2002-2012	250 – 0.05 hPa
GOMOS/Envisat	IPF v6	2002-2011	250 – 10^{-4} hPa
OSIRIS/Odin	USask v5.7	2001-2013	450 – 0.1 hPa
SMR/Odin	Chalm. v2.1	2001-2013	300 – 0.05 hPa
ACE-FTS/SCISAT	UoT v3.5	2004-2013	450 – $2 \cdot 10^{-4}$ hPa

In phase 2, In Phase 2, the new version of HARMOZ is available: altitude-gridded (HARMOZ_ALT) and pressure-gridded (HARMOZ_PRS) ozone concentration datasets. The new HARMOZ dataset contains the new reprocessed data from the abovementioned instruments. In addition, OMPS/SuomiNPP data and GOMOS bright limb data are included in the HARMOZ_ALT and HARMOZ_PRS datasets. Also HARMOZ datasets for MLS/Aura, SABER/Timed, SAGE II/ERBS, HALOE/UARS are created, they can be provided on request. The information about the new datasets is collected in Table 5.2.

Table 5.2 Information about the HARMOZ_ALT and HARMOZ_PRS dataset

Instrument/ satellite	Level 2 processor	Years	Vertical range	Retrieval vertical coordinate
MIPAS/Envisat	KIT/IAA V7R_O3_240	2002-2012	6-70 km/400- 0.05 hPa	altitude
SCIAMACHY/Envisat	UBr v3.5	2002-2012	5-65 km/250 – 0.05 hPa	altitude
GOMOS/Envisat	ALGOM2s v1	2002-2011	10-105 km/250- 10^{-4} hPa	altitude
GOMOS bright limb/ Envisat	GBL v1.2	2002-2011	10-59 km/70 – 0.2 hPa	altitude
OSIRIS/Odin	USask v5.10	2001-2017	10-59 km/450 – 0.1 hPa	altitude
ACE-FTS/SCISAT	UoT v3.5/3.6	2004-2017	6-94 km/450- $2 \cdot 10^{-4}$ hPa	altitude
OMPS-LP/Suomi-NPP	USask 2D v1.0.2	2012-2016	6-59 km/	altitude

5.1.2   Monthly zonal mean data from individual instruments (MZM)

For creating monthly zonal mean data from the individual instruments, 10° latitude bands from 90°S to 90°N are used. For all sensors, the monthly zonal average is computed as the mean of ozone profiles $x_k(z)$:

$$\rho(z) = \frac{1}{N} \sum x_k(z) \,,$$ **Eq. 5.1**

where N is the number of measurements ($N>10$). The uncertainty of the monthly mean σ_ρ^2 can be estimated as the standard error of the mean:

$$\sigma_\rho^2 = \frac{s^2}{N} \,,$$ **Eq. 5.2**

where $s^2 = \left\langle (x_k - \rho)^2 \right\rangle$ is the sample variance. Eq. (5.2) is valid for random samples of uncorrelated data. As shown by Toohey and von Clarmann (2013), some deviations of the real standard error of the mean from that calculated using Eq. (5.2) can be observed for satellite observations. In our study, Eq. (5.2) is used as an approximate estimate of the standard error of the mean, since no estimates considering the impact of the correlations caused by the orbital sampling are currently available. In Eq. (5.2), we used a robust estimator for the sample variance: $s = 0.5 \cdot (P_{84} - P_{16})$, where P_{84} and P_{16} are the 84th and 16th percentiles of the distribution, respectively. Monthly zonal mean, sample variability s and standard error of the mean from 15 to 50 km altitude in January 2008 are shown for the Ozone_cci instruments in Figure 5.1. The ozone distributions shown in Figure 5.1 are very similar for all datasets. Due to large number of data available for averaging, the standard error of the mean is usually less than 1% in the stratosphere.
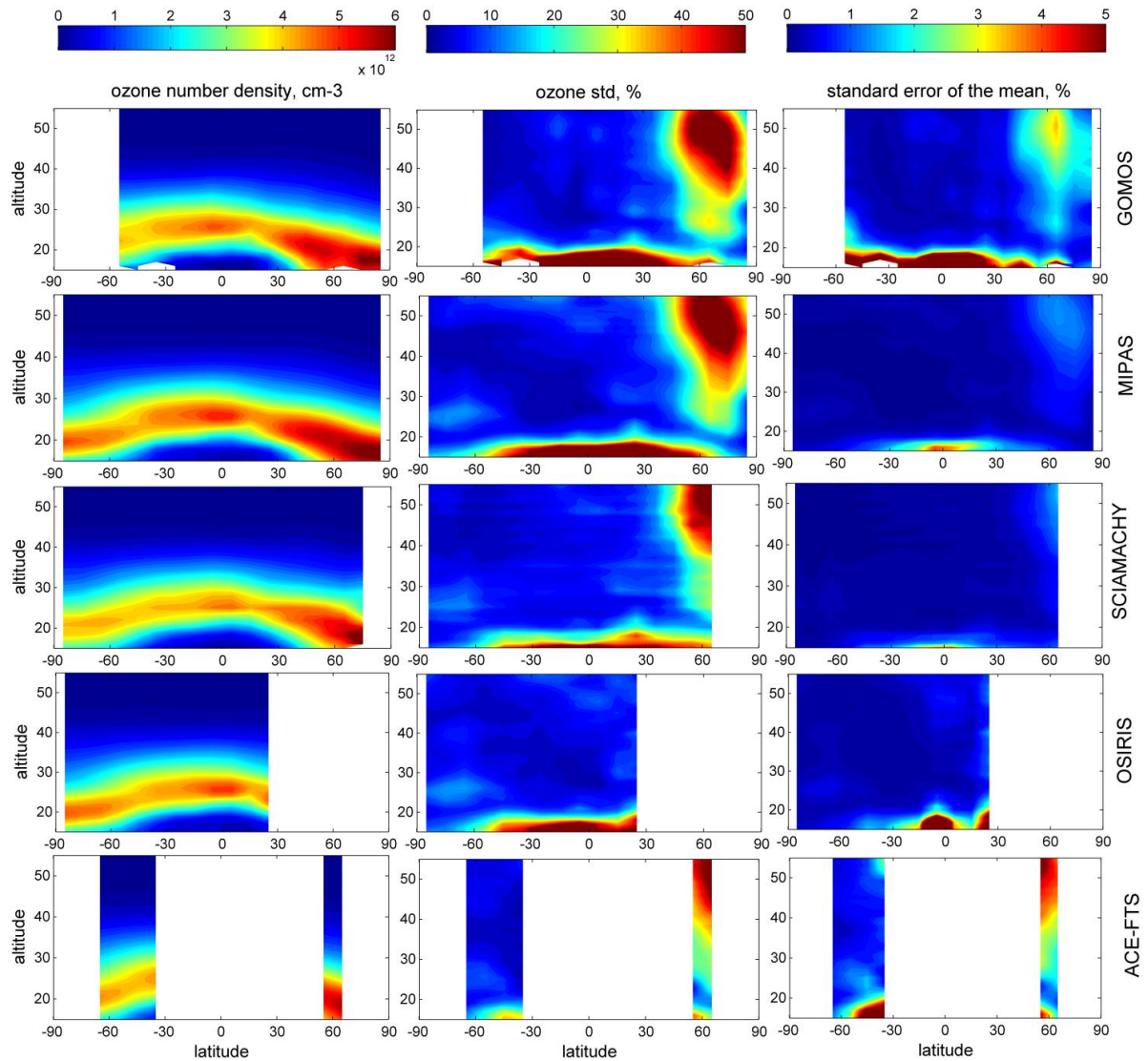
Figure 5.1: Left: monthly zonal mean ozone profiles for January 2008 for Ozone_cci instruments, center: sample variability in %, right: standard error of the mean calculated using Eq. (5.2).

Satellite measurements sample a continuous ozone field at some locations and times. To characterize the non-uniformity of sampling, we computed inhomogeneity measures in latitude, H_{lat}, and in time, H_{time} (Sofieva et al., 2014a). Each inhomogeneity measure H is the linear combination of two classical inhomogeneity measures, asymmetry A and entropy E (for definition of these parameters, see Sofieva et al., 2014a):

$$H = \tfrac{1}{2}(A + (1-E)).$$ **Eq. 5.3**

The inhomogeneity measure H ranges from 0 to 1 (the more homogeneous, the smaller H). For dense samplers (MIPAS, SCIAMACHY, OMPS), the inhomogeneity is close to zero for nearly all latitude bins. For other instruments, inhomogeneity measure can be large for some latitude-time bins.

The mean of individual error estimates e_k:

$$\bar{e} = \frac{1}{N}\sum e_k,$$ **Eq. 5.4**

are also provided in the MZM data files.

The monthly zonal mean data are structured into yearly netcdf files, for each instrument separately. The self-explaining name indicates the instrument and the year.

5.1.3 Merged monthly zonal mean data (MMZM)

The merged monthly zonal mean dataset of ozone profiles, which is also referred to as the SAGE-CCI-OMPS dataset, is created using the data from several satellite instruments: SAGE II on ERBS, GOMOS, SCIAMACHY and MIPAS on Envisat, OSIRIS on Odin, ACE-FTS on SCISAT, and OMPS on Suomi-NPP. The merged dataset is created with the aim of analyzing stratospheric ozone trends. The information about the used individual datasets is collected in Table 5.3.

Table 5.3. Information about the datasets used in the merged dataset

Instrument/ satellite	Processor, data source	Time period	Local time	Vertical resolution	Estimated precision	Profiles per day
SAGE II/ ERBS	NASA v7.0, original files	Oct 1984 – Aug 2005	sunrise, sunset	~1 km	0.5-5%	14-30
OSIRIS/ Odin	USask v 5.10, HARMOZ_ALT	Nov 2011 – July 2016	6 a.m., 6 p.m.	2-3 km	2-10%	~250
GOMOS/ Envisat	ALGOM2s v 1.0, HARMOZ_ALT	Aug 2002 – Aug 2011	10 p.m.	2-3 km	0.5–5 %	~110
MIPAS/ Envisat	KIT/IAA V7R_O3_240, HARMOZ_ALT	Jan 2005 – Apr 2012	10 p.m., 10 a.m.	3-5 km	1–4%	~1000
SCIAMACHY/ Envisat	UBr v3.5, HARMOZ_ALT	Aug 2003- Apr 2012	10 a.m.	3-4 km	1-7%	~1300
ACE-FTS/ SCISAT	v3.5/3.6, HARMOZ_ALT	Feb 2004 – Dec 2016	sunrise, sunset	~3 km	1-3%	14-30
OMPS/ Suomi NPP	USask 2D, v1.0.2, HARMOZ_ALT	Apr 2012- Aug 2016	1:30 p.m.	~1 km	2-10%	~1600

Monthly zonal mean data from individual instruments, which are described above, are used as an input for creating the merged monthly zonal mean data.

For each instrument, latitude band and altitude level, the deseasonalized anomalies are computed as:

$$\Delta(t_i) = \frac{\rho(t_i) - \rho_m}{\rho_m}, \qquad\qquad \textbf{Eq.5.5}$$

where $\rho(t_i)$ is the monthly mean value at a certain altitude and latitude band corresponding to time t_i and ρ_m is the mean value for the corresponding month m, i.e., $\rho_m = \frac{1}{N_m}\sum_{j=1}^{N_m}\rho_j$, N_m being the number of monthly mean values ρ_j in a given month m available from all years. The uncertainty of the seasonal cycle value σ_m for each month m is evaluated from uncertainties of individual monthly mean values $\sigma_{\rho,j}$:

$$\sigma_m^2 = \frac{1}{N_m^2} \sum_{j=1}^{N_m} \sigma_{\rho,j}^2 \qquad \textbf{Eq. 5.6}$$

It describes the propagation of the random uncertainties to the mean value.

For the Ozone_cci instruments, the seasonal cycle is evaluated using the overlapping period 2005-2011. The seasonal cycle for SAGE II is computed using years 1985-2004 and for OMPS using the years 2012-2016. In computation of deseasonalized anomalies, we ignored data from those latitude-time bins with the mean inhomogeneity $H_{tot} = 0.5(H_{lat} + H_{time}) > 0.8$ (for all considered satellite instruments, longitudinal inhomogeneity is negligible, Sofieva et al., 2014a).

After the removal of the seasonal cycle, the SAGE II deseasonalized anomalies are offset to the Ozone_cci mean anomalies in the years 2002-2005. The OMPS deseasonalized anomalies are offset to the mean Ozone_cci anomalies (which are based on OSIRIS and ACE-FTS measurements in this period) in the years 2012-2016.

Before merging, the deseasonalized anomalies of the individual instruments have been extensively inter-compared with each other by computing and visualizing the time series of difference of individual anomalies from the median anomaly. This method turns out to be a sensitive method for detecting an unusual timeseries behavior of the individual data records. In particular, it was found that SCIAMACHY anomalies are larger in the beginning of the mission, for nearly all latitude bands and many altitude levels (Sofieva et al., 2017b, Supplement). This might be attributed to possible pointing problems in the beginning of the mission; therefore we decided not to use the SCIAMACHY data before August 2003 in the merged dataset. Similarly, OMPS anomalies are lower in the first three months of the mission (Sofieva et al., 2017b, Supplement); this might be related to relatively coarse sampling of OMPS in the first three months of the mission and possible problems with pointing. Therefore, OMPS data were included in the merged dataset starting from April 2012, when the instrument operated in its full capacity.

We computed the merged anomaly as the median of the individual instruments anomalies, for each altitude level z and for each latitude band θ and month t:

$$\Delta_{merged}(\theta, z, t) = \text{median}(\Delta_k(\theta, z, t)), \qquad \textbf{Eq. 5.7}$$

where Δ_k indicates the individual instrument anomaly. Figure 5.2 illustrates the data merging: the upper panel shows the monthly zonal mean data, while the bottom panel shows individual anomalies and the merged (median) anomaly.

As observed in Figure 5.2, the biases between the individual data records are removed by computing the deseasonalized anomalies. In the merging, we filtered out individual anomaly values (locally for each latitude band and altitude level), which differ from the median anomaly more than 10% at latitudes 40°S-40°N and more than 20% in other latitude bands. This filtering does not affect the absolute majority of cases; it removes only a few exceptional anomalies from GOMOS and ACE-FTS, which are due to lower sampling.
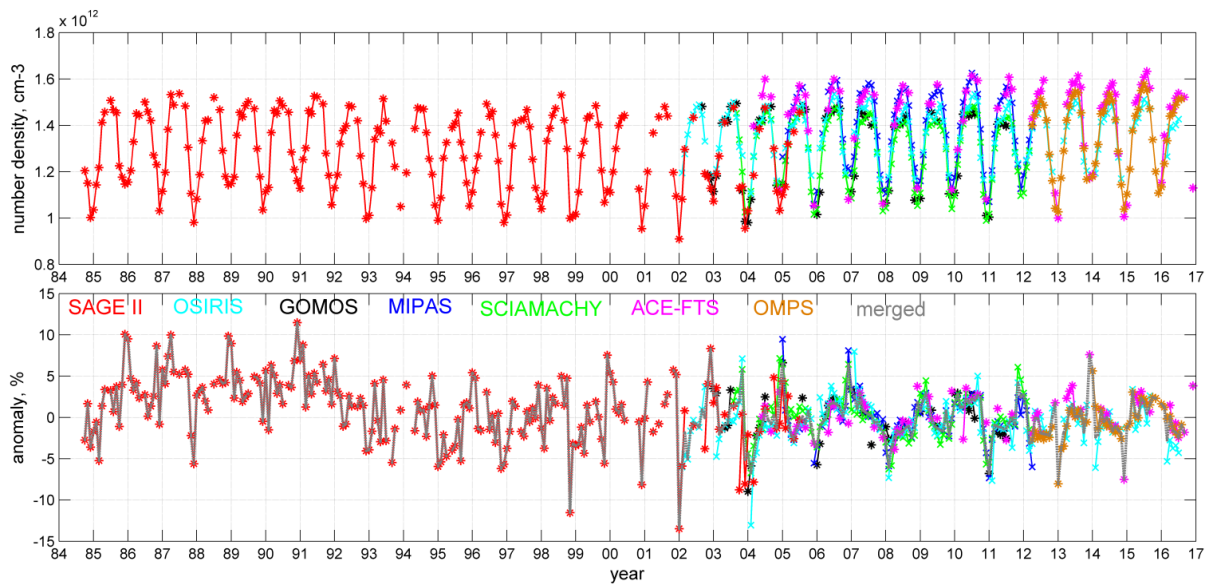
Figure 5.2: Top: monthly zonal mean ozone at 35 km in the latitude band 40°-50°N. Bottom: individual deseasonalized anomalies and the merged anomaly (grey dashed line).
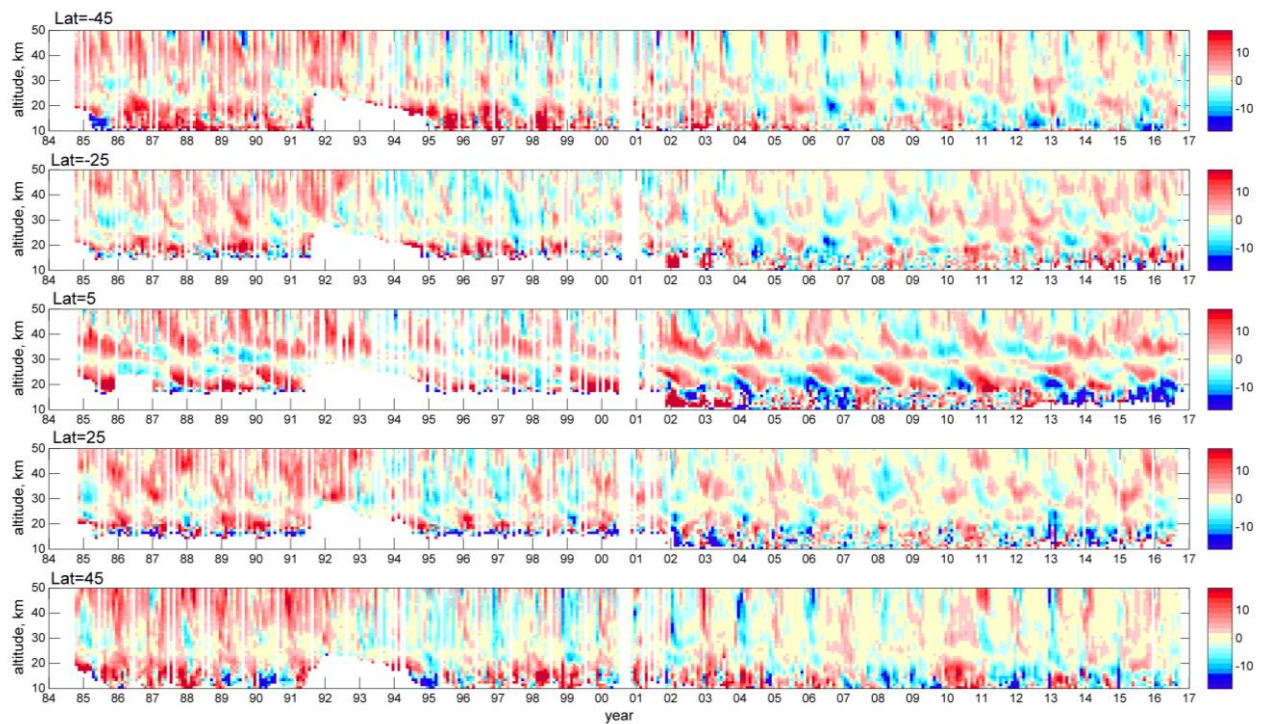

Figure 5.3 Examples of merged deseasonalized anomalies (color: %), for several 10° latitude bands, centers of which are specified in the legend.

Examples of merged deseasonalized anomalies for several latitude bands are shown in Figure 5.3. In the upper stratosphere at mid-latitudes a decrease from 1984 to 1995-1999 is observed, and then a gradual increase to the present. In the tropics, quasi-biennial oscillation (QBO) is observed.

The uncertainty of individual deseasonalized normalized anomalies (for each month) and each latitude-altitude bin $\sigma_{\Delta i}$ can be estimated as

$$\sigma_{\Delta i} = \frac{1}{\rho_m} \sqrt{\sigma_{\rho,i}^2 + \sigma_m^2}, \qquad \qquad \textbf{Eq. 5.8}$$

where $\sigma_{\rho,i}$ is the uncertainty of the monthly zonal mean value Eq. 5-1, and σ_m is uncertainty of the seasonal cycle from Eq. 5-6. We estimated the uncertainties of the merged deseasonalized anomalies (which correspond to median values) as

$$\sigma_{\Delta,merged} = \min\left(\sigma_{\Delta,j_{med}}, \sqrt{\frac{1}{N}\sum_{j=1}^{N}\sigma_{\Delta,j}^2 + \frac{1}{N^2}\sum_{j=1}^{N}\left(\Delta_j - \Delta_{merged}\right)^2} \right), \qquad \textbf{Eq. 5.9}$$

where $\sigma_{\Delta,j_{med}}$ is the uncertainty of the anomaly of the instrument corresponding to the median value. An explanation and discussion of Eq. 5.9 can be found in (Sofieva et al., 2017b).

The uncertainty of the merged dataset is illustrated in Figure 5.4 for the same latitude bands as shown in Figure 5.3. As expected, the uncertainties in the time period when only SAGE II data were available are larger than uncertainties for time periods when several instruments have contributed. The average uncertainty is usually less than 4% before 2001 and below 1% for the years 2002-2017. In the UTLS, uncertainties are larger than in the stratosphere and are in the range of 3-9 %. At mid-latitudes, uncertainties are larger in winter than in summer due to larger ozone variability during winter; this is observed clearly in the period before 2001.
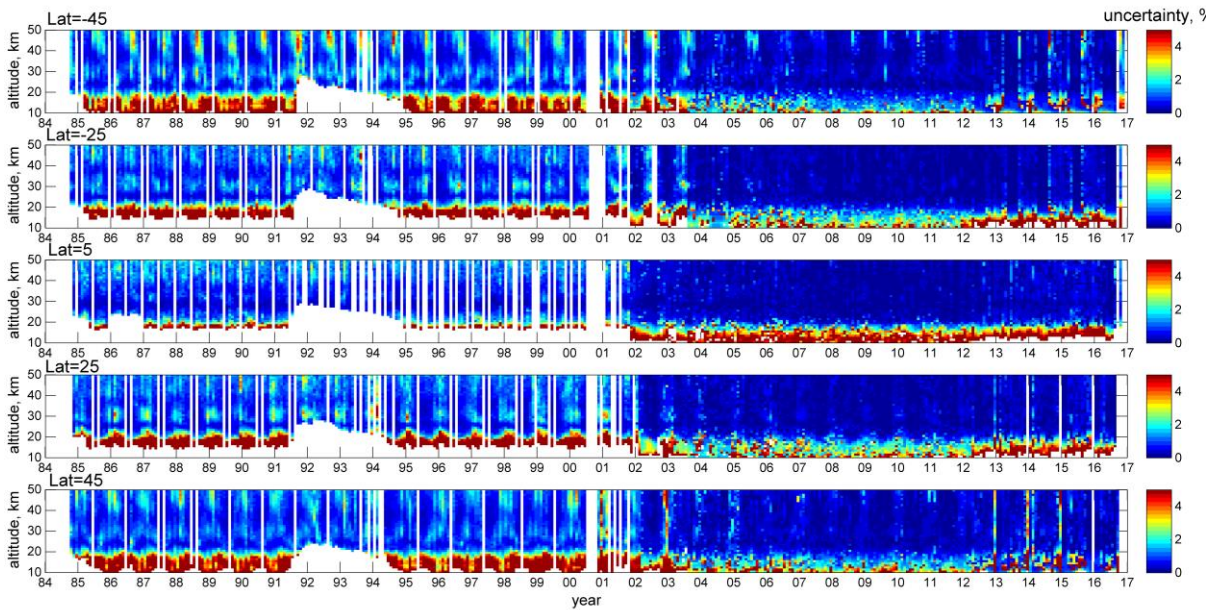
Figure 5.4: Uncertainties of the merged deseasonalized anomalies in %, Eq.**Error! Reference source not found.**, for several 10° latitude bands, centers of which are specified in the legend.
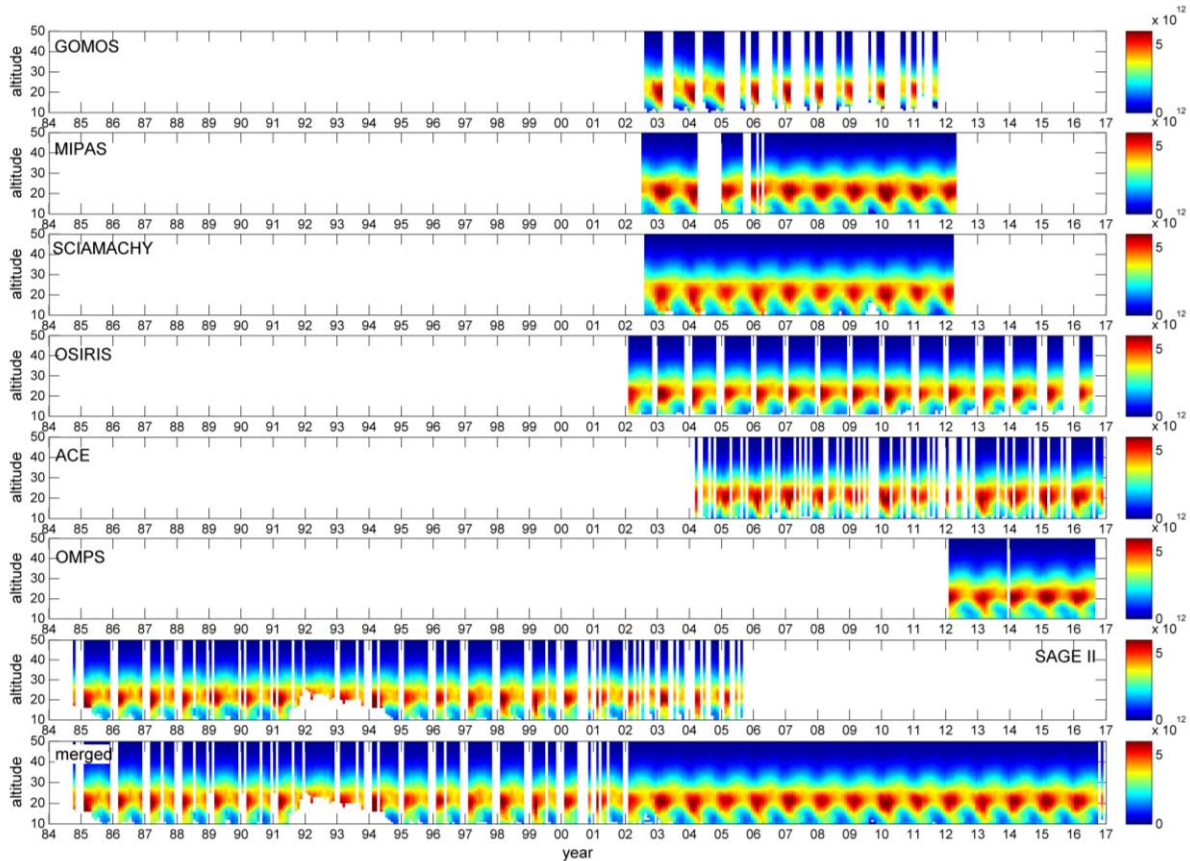
The merged SAGE-CCI-OMPS dataset consists of deseasonalized anomalies of ozone in 10° latitude bands from 90°S to 90°N and from 10 to 50 km in steps of 1 km covering the period from October 1984 to July 2016.

For trend analyses, it is recommended using the deseasonalized anomalies. According to the merging principle, the best quality of the merged dataset is in the stratosphere below 60° latitude. For the purpose of other applications (e.g., comparisons with models), we presented

also merged ozone concentration profiles. The details of computing merged number density profiles from the merged deseasonalized anomalies are presented in [*Sofieva et al.*, 2017b]. An example of merged SAGE-CCI-OMPS number density profiles is presented in Figure 5.5

Figure 5.5: Ozone number density (color: cm^{-3}), for individual datasets and the merged SAGE-CCI-OMPS dataset, for the latitude band 50°-60° N.

All data are included into one netcdf4 file, which includes both merged data and the data from individual instruments.

5.1.4 Monthly mean ozone profiles with resolved longitudinal structure

The monthly zonal mean gridded ozone profile dataset is provided in the altitude range from 10 km to 50 km. It covers the time period from late 2001 until now. The data are gridded monthly in the 10° latitude x 20° longitude zones. Since the sampling of solar occultation measurements is rather low, they are not included. The gridded ozone profiles are presented for GOMOS, MIPAS, SCIAMACHY and OSIRIS separately and also merged into one dataset. The information about the individual datasets can be found in **Error! Reference source not found.**. The principle of creating the Level 3 gridded data for individual datasets, as well as data merging is the same as for the monthly zonal mean dataset (see Section 5.1.3).

5.1.5   Merged mesospheric Ozone_cci dataset

5.1.5.1   Dataset description

The merged dataset of mesospheric timeseries and anomalies, for daytime and night-time, is created out of daytime and night-time ozone profiles from the following instrument: MIPAS instrument in nominal mode (MIPAS NOM), MIPAS instrument special modes (MIPAS SM), SCIAMACHY and GOMOS instruments. Day dataset is obtained by merging MIPAS SM day, MIPAS NOM day, and SCIAMACHY, where MIPAS day measurements are MIPAS measurements with solar zenith angle < 90 degrees. Night datasets are obtained by merging MIPAS SM night, MIPAS NOM night, and GOMOS, where MIPAS night-time are MIPAS measurements with solar zenith angle > 108.

Measurements from MIPAS SM are used as the reference for the merging. Merging methodology: the anomalies from all instruments are calculated using their own seasonal cycle in the 2005-2012, which is the common period with MIPAS SM. The anomalies are then merged as the mean of what is available, this is justified by a good agreement between anomalies of parent datasets. Merged time series is restored from the merged anomalies, using the seasonal cycle from MIPAS SM. Dataset contains merged anomalies (in %) and merged time series (in number density). Uncertainties are calculated from uncertainties of monthly zonal means of the parent dataset by Gaussian error propagation.

The dataset is delivered with uncertainties, at vertical 1-km altitude grid between 50 km and 100 km, in [90S,60S], [60S,40S], [40S,20S], [20S,20N], [20N,40N], [40N,60N], [60N,90N] latitude bands, covering time period from January 2005 to April 2012.

5.1.5.2   Data participating in the merging

MIPAS special modes: MA and UA as one single dataset

In the MIPAS middle-atmosphere (MA) mode, the spectra are available at limb tangent heights from about 20 up to 102 km with a vertical sampling of 3 km. The upper atmosphere (UA) mode ranges from about 42 to 172 km, and has a vertical sampling of 3 km up to 102 km height, and 5 km above this altitude.

Figures 5-6 and 5-7 show examples of daily means from night and day measurements of two modes; a good agreement between them is observed at all heights and all latitudes bands. This allows taking the measurements from these two modes together, as one single dataset.
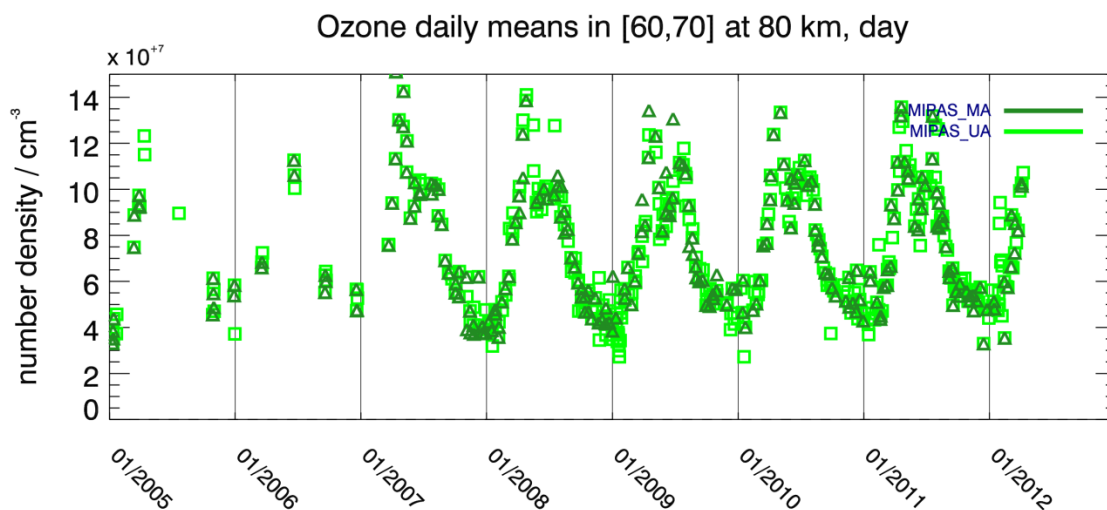

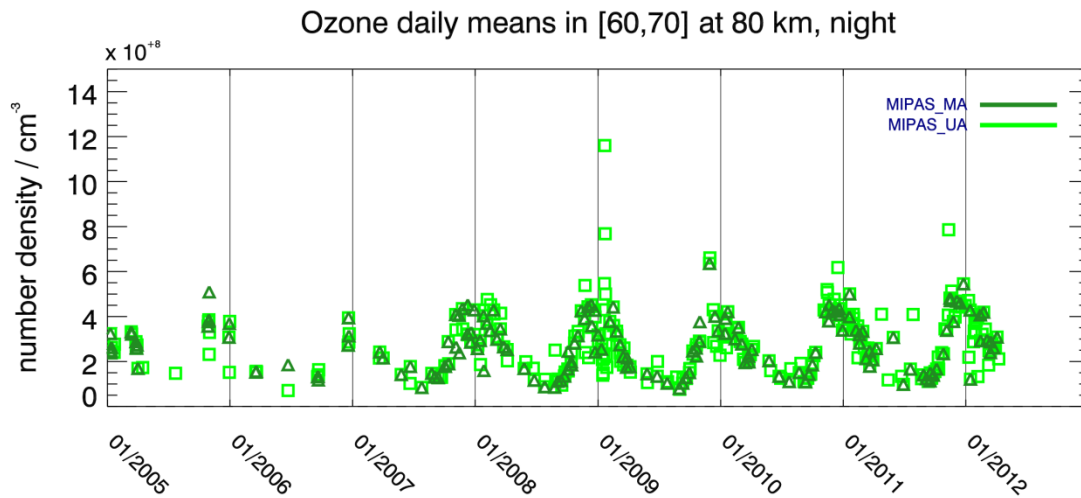**Figure 5.6 Example of daily means of daytime measurement of MIPAS UA and MA modes.**

Figure 5.7 Daily mean night-time MIPAS UA and MA measurements.

Temporal and altitude coverage

Most measurements of special modes of MIPAS instrument took place in 2005-2012 period, which reduces the temporal coverage of mesospheric merging, and makes us to ignore 2002-2004 data from MIPAS NOM, SCIAMACHY and GOMOS. Ozone data from nominal mode of MIPAS (MIPAS NOM) and SCIAMACHY have altitude coverage going up to 65 km only. Due to their measuring geometry, SCIAMACHY instrument took measurement of ozone in the daytime only, GOMOS instrument (stellar occultation) – during night time only. These considerations bring us to the following table of merging opportunities.

Table 5.4 Mesospheric merging opportunities of Ozone_cci data.

	Day time	*Night time*
65 – 100 km	MIPAS SM	GOMOS MIPAS SM
50 – 65 km	SCIAMACHY MIPAS NOM MIPAS SM	GOMOS MIPAS NOM MIPAS SM

Note that at the time of the production of the dataset, MIPAS special modes data available were produced out of the version 5 of Level 1 MIPAS data, while MIPAS_NOM data are produced out of the version 7. Version 5 of Level 1 data is known to contain some drifts (ref to MK), which are corrected in the version 7 (ref to AL). These could introduce some drifts in the merged data record. We therefore recommend not use the record for the trend studies (it is just 7 years long).

5.1.5.3   Agreement of time series, seasonal cycles and anomalies from participating datasets

At all height in all latitude bands, a good agreement is observed for time series, anomalies and seasonal cycles of participating datasets, as demonstrated at the figures below.
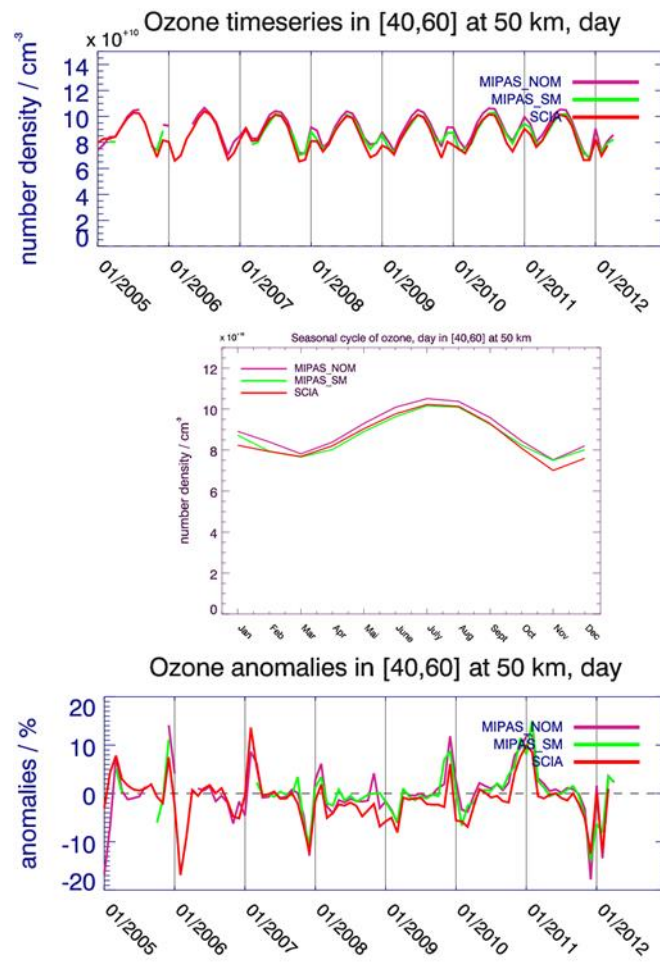
Figure 5.8 Example of daytime time series (upper panel), seasonal cycles (middle panel) and anomalies (bottom panel) of the datasets participating in the merging.

This allows simplification of the merging procedure, but first the biases between participating datasets should be evaluated.

### 5.1.5.4   Biases between datasets participating in the merging

It can be observed at the Figure that the differences do not evolve with time, i.e. no drift between the dataset, which allows take MIPAS SM data as a reference for the merging. However, the differences have the seasonal component, which is an obstacle to do the debiasing in the merging procedure.
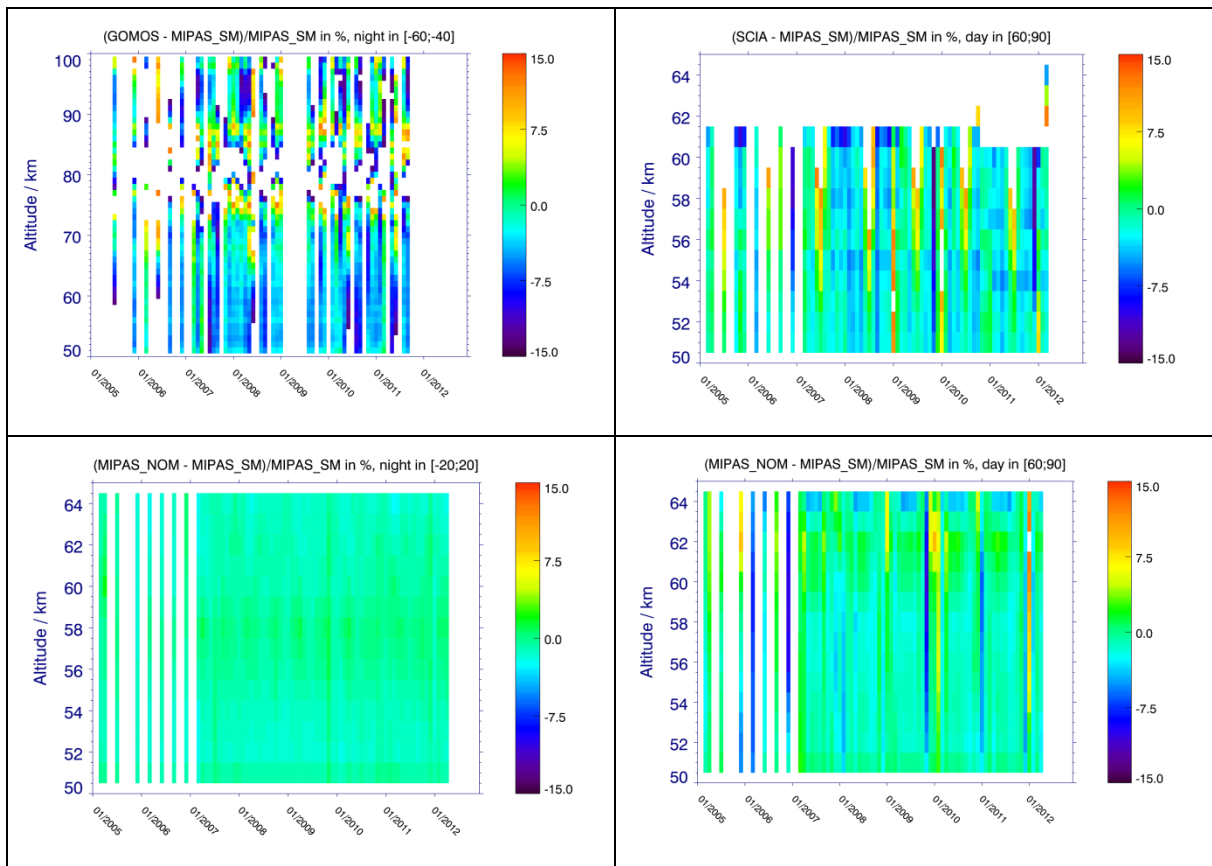
Figure 5.9 The evolution of the differences between the parent datasets and MIPAS SM with time, in percent.

5.1.5.5 MIPAS SM anomalies: day versus night

For trend calculation, anomalies are often used rather than the vmr's or number density. One way to perform the merging would be to merge day and night anomalies in one dataset. This is however not allowed, because the day and night anomalies are in partial agreement only: they are the same up to 60 km, than they differ.
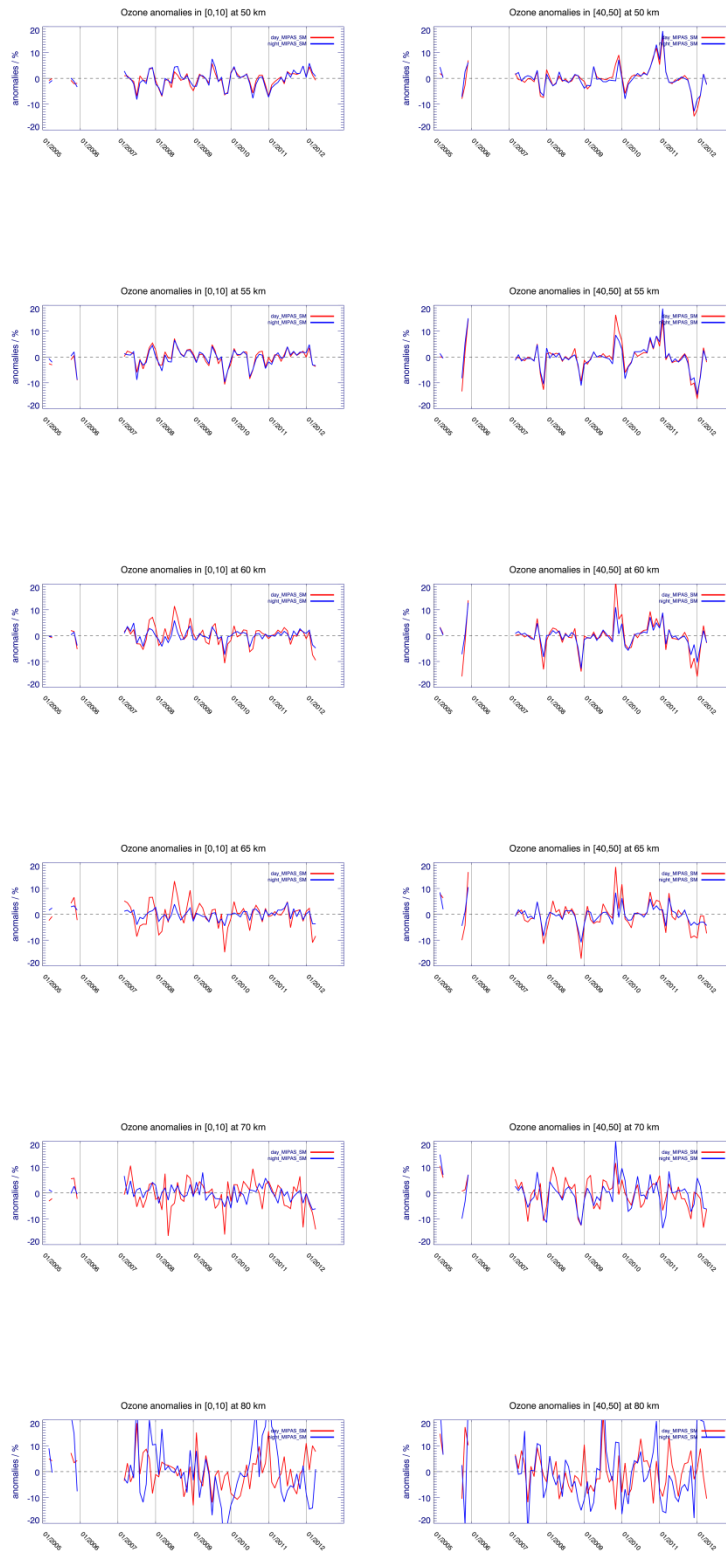
Figure 5.10 Tropical (left) and northern mid-latitudes anomalies (right) from daytime (red) and nighttime (bleu) at heights 50 km (top), 55 km, 60 km, 65 km and 70 km (bottom). The daytime and nighttime anomalies are in good agreement at heights below 60 km, they differs at upper heights.

5.1.5.6   Merging approach and resulting dataset

The merging is performed in a following way. The anomalies from all instruments are calculated using their own seasonal cycle in the 2005-2012, which is the common period with MIPAS SM. Then the anomalies are merged by taking the simple mean of what is available at each height in each latitude band. Merged time series is restored from the merged anomalies by using the seasonal cycle from MIPAS SM day / night. Examples of resulting merged anomalies and time series are given in Figure 5.11.
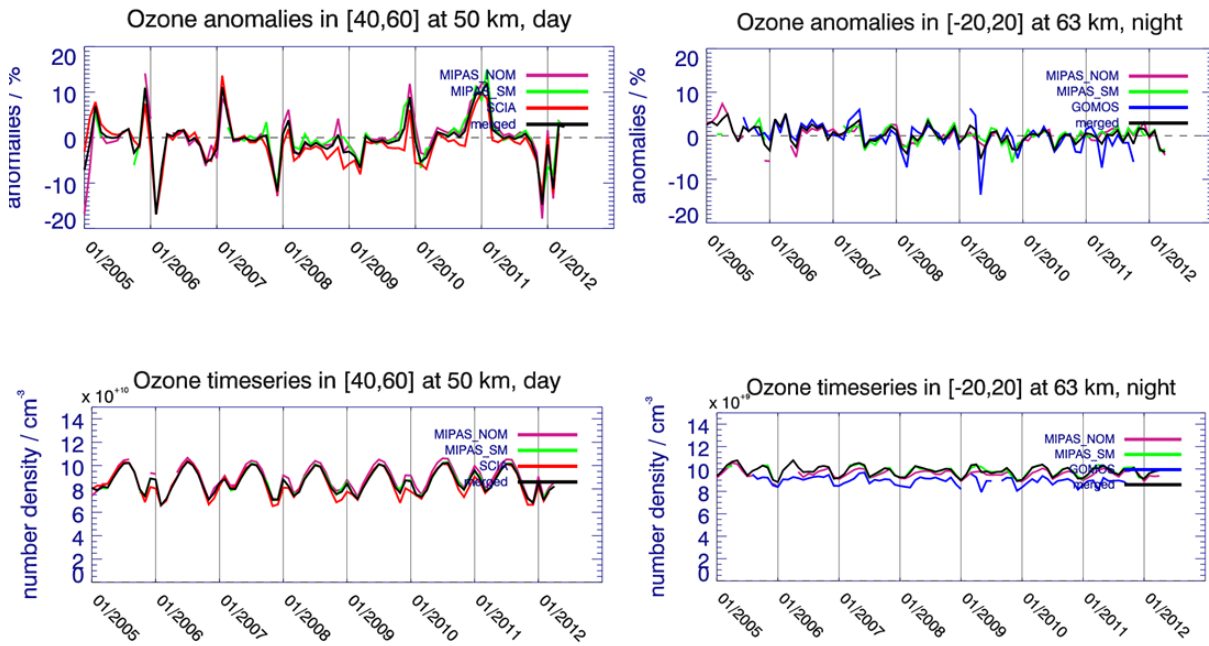

Figure 5.11. Examples of merged anomalies in the mesosphere.

5.1.5.7   UTLS datasets

The new HARMOZ_ALT datasets include the information important for the UTLS research: the tropopause height. The tropopause height is computed according to the classical definition of lapse-rate/thermal tropopause definition (WMO, 1957). Single and double tropopauses are detected using either temperature profiles retrieved by an instrument of using the ERA-Interim data.

Many Level 3 monthly zonal mean datasets from individual instruments cover the UTLS region. The merged SAGE II–Ozone_cci–OMPS dataset and merged dataset with the resolved longitudinal structure also include the UTLS.

In addition, seasonal (3-months average, for each year) ozone distribution at several pressure levels in the upper troposphere and the lower stratosphere are created for four Ozone_cci instruments with sufficiently dense horizontal sampling: MIPAS, SCIAMACHY and GOMOS on Envisat and OSIRIS on Odin. For MIPAS, data from 2005-2012 are used. For other instruments, the seasonal distributions are provided for all available data. The data are gridded in the 5° latitude x 10° longitude bins, for several pressure levels: 200, 170, 150, 130, 115, 100, 90, 80, 70 and 50 hPa.

5.1.6   Assessment of URD implementation for limb and occultation data

The input of limb instruments data into ozone ECV will be a product that will result from the merging of 4 instruments' datasets: MIPAS, SCIAMACHY, GOMOS, and OSIRIS. The very principle of the data merging understands that the data can only be ameliorated: every non-compliant characteristic of a participating dataset will be translated into error terms, leading to the smaller weight to non-reliable measurements. In other word, if at least one of participating dataset is compliant in one characteristic, one can arrange to have the merged data product being compliant in this characteristic as well.

The
Table 18 below recapitulates the compliance with URD for each of four participating datasets, and gives estimation for the potential compliance of the merged data product. "LS" stays for "lower stratosphere", "MA" for "middle atmosphere". Remark that for limb instruments, the concept of "horizontal resolution" is ambiguous. One is the "intrinsic" horizontal resolution caused by limb geometry. It can be estimated as effective length of interaction with atmosphere that provides measurements at given altitude. This effective length is measured along the line of sight. Another meaning might be related to density of measurements in horizontal direction. But then the question is on the corresponding time interval (because these measurements are not simultaneous). These considerations drove us to put "uncertain" in the corresponding row of the table.

Table 18 : Assessment of the product requirements implementation for limb and occultation ozone profiles

Requirements as stated in URD				Compliance of individual products with these requirements				Potential compliance of the merged product
Quantity	Driving research topic	Height range		MIPAS	GOMOS	SCIA	OS IRI S	Merged product
		LS	MA					
Horizontal resolution	- Regional differences in the evolution of the ozone layer (radiative forcing); - Seasonal cycle and interannual variability; - Short-term variability: exchange of air masses, streamers, regime studies	100 – 300 km	100 - 300 km	Uncertain (415-515 km along the line of sight)	Uncertain	Uncertain but a rough estimation is 240 km in LS, 960 km in MA	Unc erta in	Uncertain (not applicable to limb instruments)
Vertical resolution	- Height dependence of evolution	1-3 km	1-3 km	1.5-2 km in LS, 3.5-	compliant	4 km	tbd	compliant

	of the ozone layer (radiative forcing); -Seasonal cycle and interannual variability; -Short-term variability			5 km in MA				
Observation frequency	Seasonal cycle and inerannual variability; Short-term variability	3 days	3 days	3 days	compliant	6 days	tbd	compliant
Time period	Evol. of the ozone layer (radiative forcing)	(1980-2010) – (2003-2010)	(1980-2010) – (2003-2010)	2002-current	compliant	2002-2010	tbd	compliant
Accuracy[8] in height attribution	Evolution of the ozone layer (radiative forcing); - Seasonal cycle and interannual variability; - Short-term variability:	± 500 km	± 500 km	60-150 m	compliant	± 200 m	tbd	compliant
Accuracy[9] for mixing ratio	Evolution of the ozone layer (radiative forcing)	8%	8%	compliant	compliant	10 %	tbd	compliant
Accuracy [10] for mixing ratio	- Seasonal cycle and inter annual variability; - Short-term variability: exchange of air masses, streamers, regime studies (radiative forcing)	15%	15%	Compliant	compliant	<15%	tbd	Compliant

---

[8] In this context: the total error of the retrieval

[9] idem

[10] idem

6   Tropospheric ozone column ECV

To retrieve Tropospheric Ozone Column (TOC), different methods are used within the Ozone_cci project. Limb Nadir Matching LNM (SCIAMACHY UBR), CCD method (DLR) and Infrared Emission (IASI).
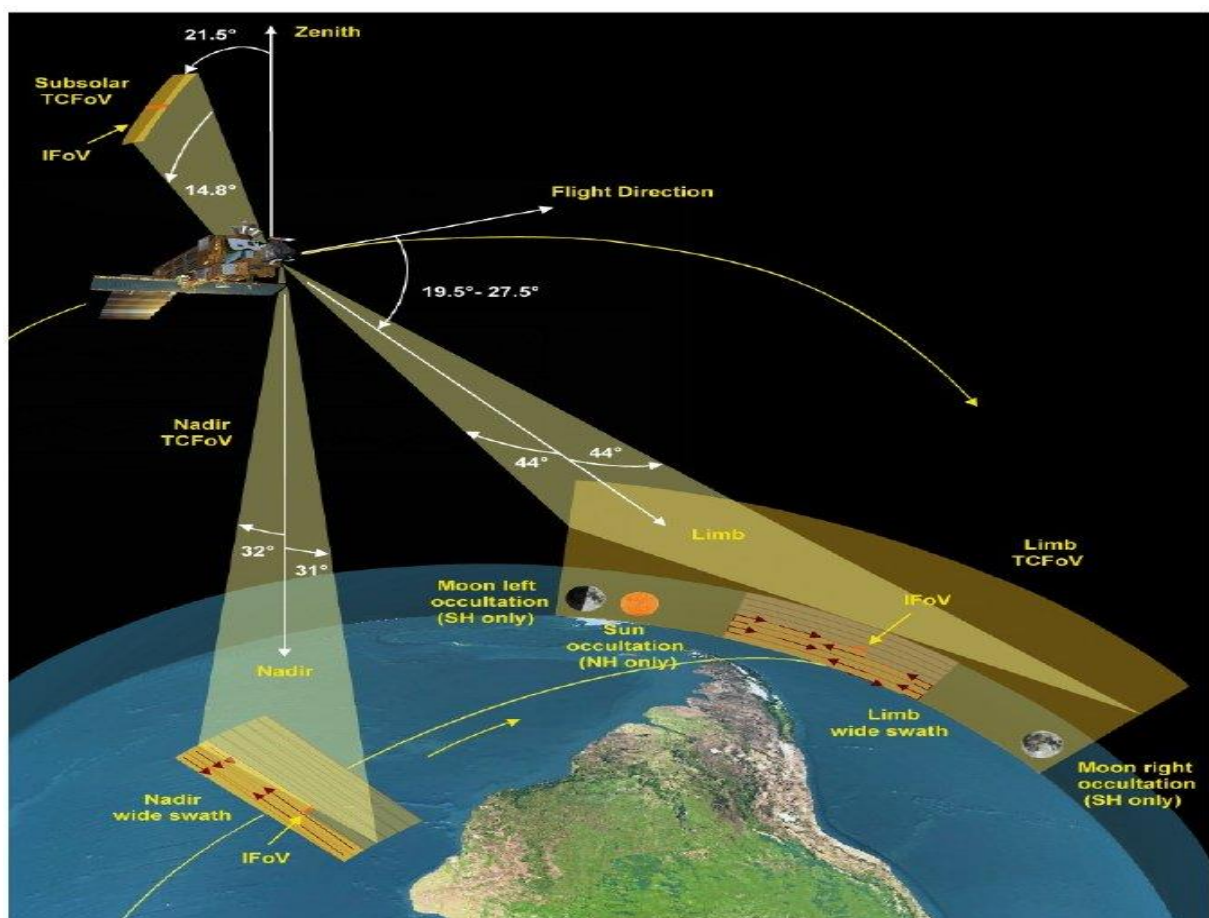
6.1.1   Limb Nadir Matching Method UBR

Figure 6.1: SCIAMACHY viewing geometry for Nadir and Limb (DLR-IMF).

The limb nadir technique for derivation of the tropospheric ozone column is used by combining matched nadir and limb profiles (Ebojie et al. 2014). The nadir viewing geometry delivers the total ozone column with high precision depending on the cloud coverage of the nadir pixel. The limb profiles are vertically resolved ozone profiles, that covers mainly the stratosphere and mesosphere (See Chapter 4). The SCIAMACHY limb ozone and nadir ozone profiles and combination of them are used here to derive the SCIAMACHY Limb Nadir Tropospheric Ozone Columns (LNTOC).

The SCIAMACHY instrument was designed to alternate between limb and nadir geometries so that the region probed during the limb scan can be observed about 7 minutes later during the nadir scan (Figure 6.1). The limb measurement delivers the stratospheric column over the same area as the nadir measurement of the total column. The matching is performed by using the same air mass from the two viewing geometries. The tropospheric column is then derived by subtraction of the two columns. For this purpose the knowledge of the tropopause height (TPH), which is the boundary between the defined troposphere and stratosphere is crucial. In the tropical band the tropopause is well above the lowest altitude of the limb measurement. This is not the case for the higher altitudes, where the tropopause can be lower than the minimum height of the limb ozone profile. In this case, interpolation of the stratospheric ozone has to be supported by the use of the ozone sonde climatologies (Ebojie 2014). The ground pixel of limb is 400km x 240km. For the nadir viewing the ground pixel is of the area 30 km x 60 km. This leads to the matched nadir limb ground pixel in the order of 60 x 240 km for the single tropospheric column (See Figure 6.2).

Figure 6.2: **Comparison of ground pixel sizes. Nadir pixel as yellow square (30km x 60 km), limb pixel as blue area (400km x 240 km) that results into a tropospheric pixel of 60km x 240km.**

Only cloud free limb scenes and nadir pixels with cloud fraction cf < 30% of cloud coverage were used. In addition, the analysis has been restricted to solar zenith angles (SZA) lower than SZA < 80° from the descending part of the orbit due to higher sensitivity of nadir measurement to ozone for higher SZAs.

6.1.2 Matching Algorithm

The Limb Nadir matching technique is based on the crossing number (CN) algorithm of Jordan Curve Theorem (Jordan 1887, Hales 2007). From this general mathematical formulation, the counting of the number of crossing points for a given polygon can lead to the detection of the position of the point source relative to the polygon.

The theorem proves for the Eucledian space the following relationship: ***Odd numbers of CN are coming from a point Q inside the polygon and even CNs from a Q outside of the polygon, respectively (Figure 5-3)***.
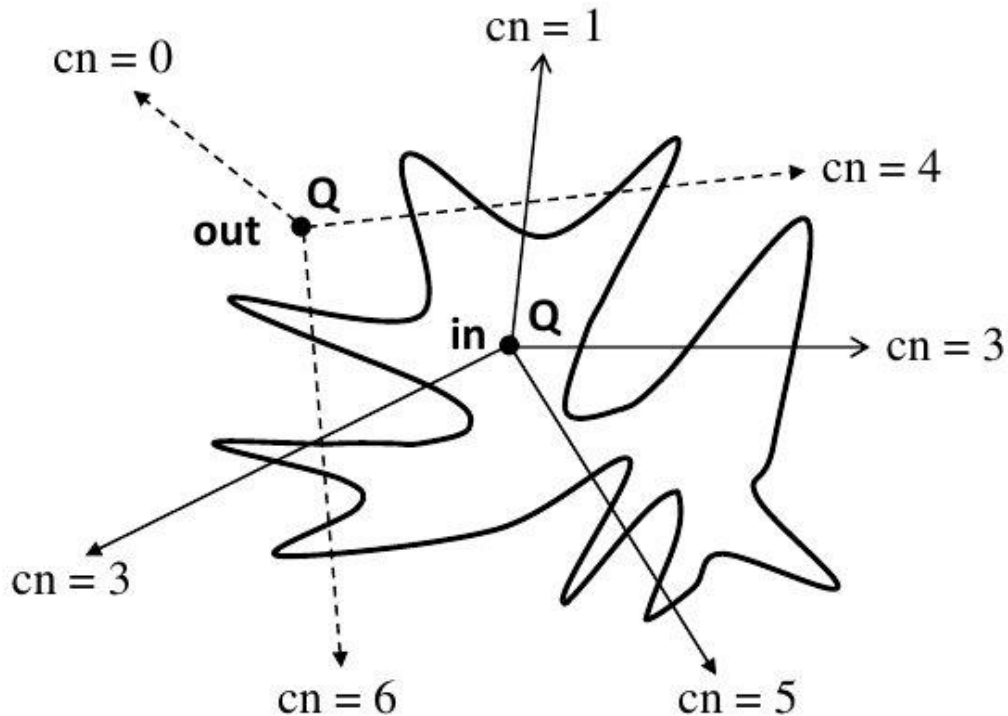
Figure 6.3: The position of the point source Q determines the number of CNs for a given polygon (Adopted from F. Ebojie 2014)

Following steps are performed for the limb/nadir pixels to match or lie within the area of each other (Ebojie 2014):

'The matched data was derived by first checking the best possible orientations of the limb box (four corners of the limb scan close to the tangent point) with vertices 1-4, which represent the latitude/longitude coordinates of a single limb scan. The orientations include from 1-3 or 2-4 or vice versa, as well as from 2-4 or 2-1 or 2-3 as shown in Fig. 5-4.

In the next step, an iteration over the corners of the nadir box (four corners of the nadir scan) is performed to find the minimum and maximum x and y coordinates of each corner, which is checked against the corners of the limb scan box. If the nadir box is confirmed to lie in the limb box, then the Total Ozone (TOZ) that meet cloud fraction threshold is averaged within a limb box. For the nadir states, which are only partially within the limb state, the nadir pixel is weighted based on the distance of its centre to nearest corners of the limb pixel. The process is iterated for all nadir pixels measured at about 7 minutes later after the limb scan.'
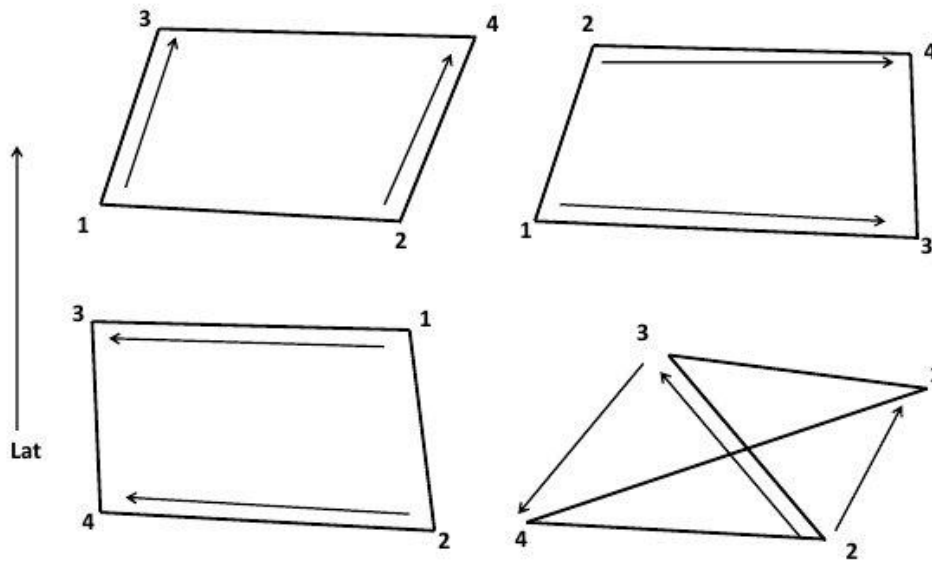
Figure 6.4: Order of the four corner pixel for nadir limb matching algorithm (Adapted from Ebojie 2014).

6.1.3   Error sources

For derivation of Tropospheric Column (TOC) from Total Ozone (TOZ) and Stratospheric Ozone Column (SOC) we use the following simple formulation:

$$TOC = TOZ - SOC$$

Hence following the Gaussian error propagation method, the error for tropospheric ozone column (X_toc) can be deduced to:

$$X_{toc} = \sqrt[2]{X\_toz^2 + X\_soc^2 + X\_tph^2}$$

where X_toz is the error in total ozone column, X_soc is the error in the stratospheric column and X_tph the contribution of the tropopause height errors. The X_soc is derived by using the error contribution of the SCIAMACHY limb ozone profiles (See Section 4.2.6).   The uncertainty in TOZ (X_toz) is calculated by applying the uncertainty in geophysical parameters in the retrieval of derivation of TOZ (Coldewey-Egbers et al. 2005).

The longitudinal structure in errors for three latitude bands 20°N-20°S, 60°N-30°N, and 60°S-30°S are shown in Figure 6.5 for January 2004 as an example. Main errors stem from the stratospheric column. The errors in TPH are negligible even though highly variable. The errors in TOC are less variable over the globe for the tropical band and highly variable for middle latitudes and presents wave structures.
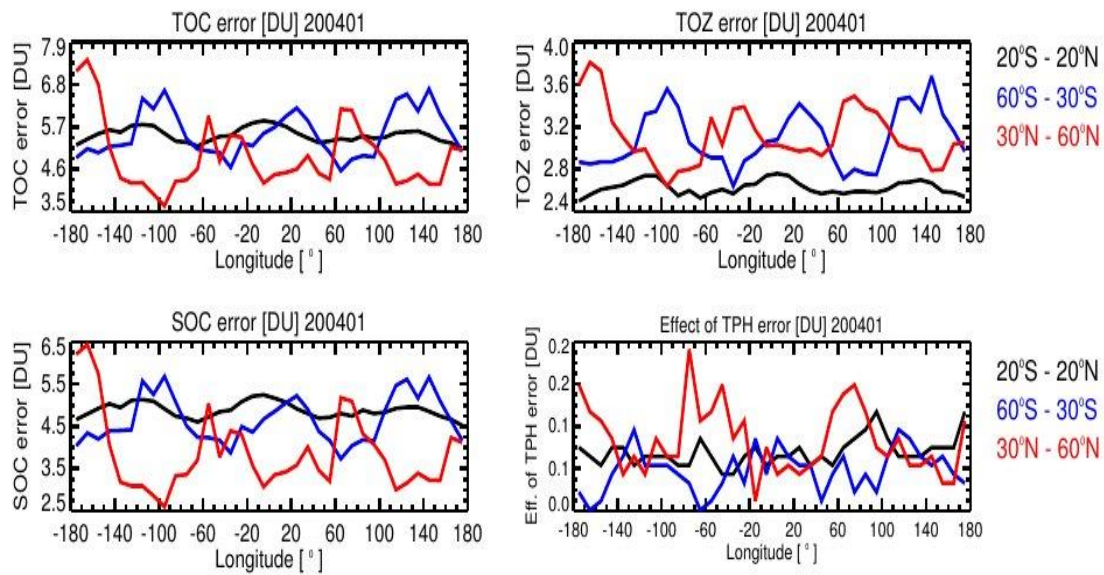
Figure 6.5: Error sources (Ebojie 2014).

The average error in the SOC is in the order of 4 DU, 0.1 DU in TPH and that of the TOZ is in the order of 3 DU, respectively. It leads to a total error of 5 DU in TOC. Since the tropospheric column is in average in the order of 30 DU, the relative fraction of the error in the TOC is around 1/6 or 16 %.

6.1.4   Convective Cloud Differential DLR

The convective cloud differential algorithm for the tropical tropospheric Ozone (TTOC) is based on the level 2 nadir total column ozone products as for example described in section 2.1. The tropospheric Ozone (TTOC) is calculated as the difference between the total column (TOZ) for cloud free pixels and the stratospheric column, where the stratospheric column (SOC) is determined as the column above high reaching clouds. Only observation with high cloud cover ($c_f > 80\%$) are taken into account, and to avoid measurements over thin cirrus clouds the cloud albedo has to be higher than 80%. The SOC is given as the difference between the total column and the ozone column below the cloud (ghost column), which is hidden below the clouds and invisible to the instrument.

For high cloud fraction: $SOC(lat, lon) = TOZ\,(lat, lon) - ghost(lat, lon)$

Because the top height of the clouds may differ, even if only clouds with a top height between 8 and 15 km are considered, the above cloud ozone columns are harmonized to a certain level (10 km). The small correction term is calculated by integrating an ozone climatology profile

between the effective cloud top and 10 km. The algorithm idea is illustrated in **Error! Reference source not found.**6. The data are monthly averaged and gridded (1.25° x 2.5°). The assumption that the SOC is constant for 1 month limits the algorithm to the tropical ozone data. Moreover, for certain regions or periods no stratospheric data are available or they are affected by up draught of tropospheric ozone pollutions e.g. over the rainforest during the burning season. Therefore only the stratospheric ozone data in a reference region are used, and assumed to be representative for the rest of the globe (Latitudinal dependency of the Stratospheric ozone column below). Thereby we indirectly presume that the stratospheric column is constant for certain latitude bands, which is a good approximation for the tropics (20°S to 20°N).

For cloud free observation: $TTOC(lat, lon) = TOZ(lat, lon) - SOC\_ref(lat)$

According to Lidar observations (Browell 2001) the upper tropospheric ozone mixing ratio in convective systems over the western pacific are less than 10 ppb, hence the up draught in this region is low. Moreover the convective cloud cover is often high. This makes the region over the eastern Indian ocean (70°E) to the western Pacific (170 W) a good reference area. More details are described in Valks et al. 2014. The cloud slicing algorithm confirms that the up draught ozone mixing ratio inside and above the cloud in the reference area is low, as explained in this paper.
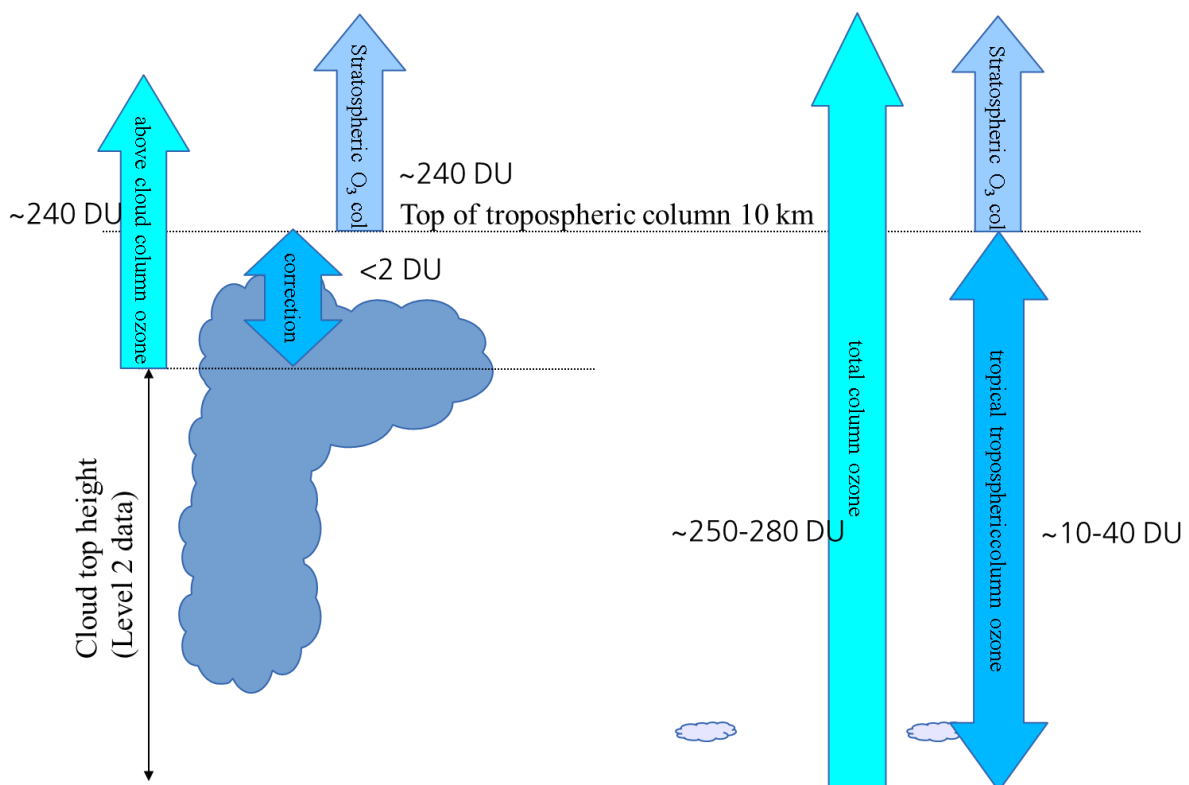

Figure 6.6: Schematic illustration of the GOME-2/CCD technique for the (sub)-tropics. Cloudy GOME-2 measurements with cloud fraction cf > 0.8, cloud top albedo ac > 0.8 and cloud top pressure pc > 320hPa, which are used to determine the above-cloud ozone.

An example of the GOME-2 tropical tropospheric ozone column distribution is shown in Figure 6-7 for September 2008. This figure illustrates the effect of biomass burning on the tropical tropospheric ozone, formaldehyde and NO_2 distribution (GDP-4.8). The bottom right figure shows the southern hemisphere biomass burning hot spots as measured by ATSR in September

2008. The biomass burning produced large amounts of NO$_2$ over Southern Africa and South America as can be seen in this figure (top left). The largest increases in ozone are found over the southern Atlantic as shown in Figure 6-7 (bottom left), and are a result of the biomass burning emissions and large-scale transport.
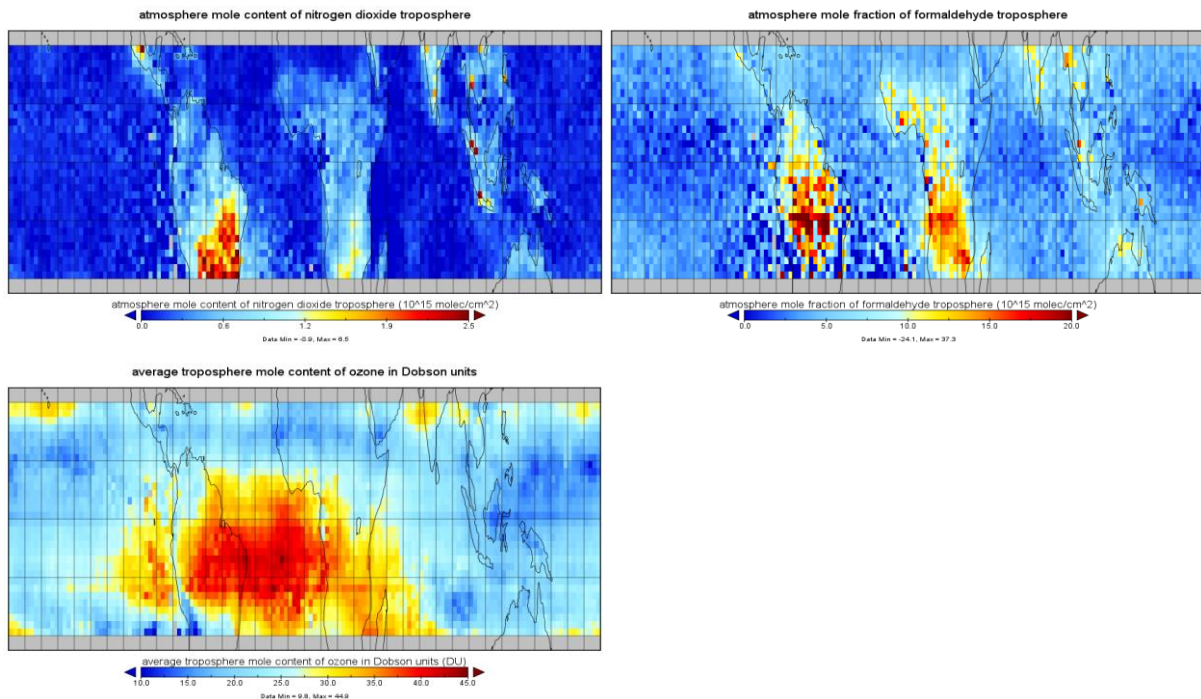
Figure 6-7 Southern hemisphere biomass burning hot spots measured by ATSR (bottom right), and tropospheric NO2 columns (top right), HCHO column (top left) and tropospheric ozone columns (bottom left) as measured by GOME-2 in September, 2008.

7   References

Acarreta, J.R., J.F. de Haan and P. Stammes, Cloud pressure retrieval using the O2-O2 absorption band at 477 nm, *J. Geophys. Res.*, 2004, **109**, D05204, doi:10.1029/2003JD003915.

August, T.; Klaes, D.; Schlüssel, P.; Hultberg, T.; Crapeau, M.; Arriaga, A.; O'Carroll, A.; Coppens, D.; Munro, R. & Calbet, X. IASI on Metop-A: Operational Level 2 retrievals after five years in orbit. *J. Quant. Spectrosc. Radiat. Transfer, 113*, 1340-1371, 2012.

Beers, Y. *Introduction to the theory of error.* Massachusets: Addison-Wesley, 1957.

Bertaux, J.-L., et al. "Global ozone monitoring by occultation of stars: an overview of GOMOS measurements on ENVISAT." *Atmos. Chem. Phys.* 10 (2010): 12091-12148.

Bhartia, P. *Algorithm Theoretical Baseline Document, TOMS v8 Total ozone algorithm .* http://toms.gsfc.nasa.gov/version8/version8_update.html, 2003.

BIPM. *Guide to the Expression of Uncertainty in Measurement (GUM), Bureau International des Poids et Mesures.* (http://www.bipm.org/en/publications/guides/gum.html, 2008.

Birch, KP & Downs, MJ. Correction to the updated Edlen equation for the refractive index of air. *Metrologia*, 31(4):315-316, 1994.

Boone, C. D., R. Nassar, K. A. Walker, Y. Rochon, S. D. McLeod, C. P. Rinsland, P. F. Bernath (2005), Retrievals for the atmospheric chemistry experiment Fourier-transform spectrometer, Appl. Opt. 44, 7218-7231.

Boone, C. D., K. A. Walker, and P. F. Bernath. "Version 3 Retrievals for the Atmospheric Chemistry Experiment Fourier Transform Spectrometer (ACE-FTS)." In *The Atmospheric Chemistry Experiment ACE at 10: A Solar Occultation Anthology*, by P. (ed) Bernath, 103–127. A. Deepak Publishing, Hampton, 2013.

Browell, E. V., et al.,: Large-scale air mass characteristics observed over the remote tropical Pacific Ocean during March–April 1999: Results from PEM-Tropics B field experiment, *J. Geophys. Res.*,106, 32481–32501, 2001.

Buehler, S., P. Eriksson, T. Kuhn, A. von Engeln, and C. Verdes. "ARTS, the Atmospheric Radiative Transfer Simulator." *J. Quant. Spectrosc. Radiat. Transfer* 91 (2005): 63-65.

Carlotti, M. (1988), Global-fit approach to the analysis of limb-scanning atmospheric measurements, Appl. Opt. 27, 3250-3254.

CCI-GUIDELINES. *ESA Climate Change Initiative. CCI Project Guidelines.* TN, Frascati: ESA ESRIN, 2010.

Chandrasekhar, S. *Radiative Transfer.* New York: Dover Publications Inc., 1960.

Clough, S, Shephard, M, Mlawer, E, Delamere, J, Iacono, M, Cady-Pereira K, Boukabara, S., Brown, P.D., Atmospheric Radiative Transfer Modeling: a Summary of the AER Codes, *J. Quant. Spectrosc. Radiat. Transfer*, 91, 233-244, 2005

CMUG-RBD. "Climate Modelling User Group Requirements Baseline Document, Deliverable 1.2, Number D1.2, Version 1.3." 2010.

Coldewey-Egbers, M., M. Weber, L. N. Lamsal, R. de Beek, M. Buchwitz, and J. P. Burrows. "Total ozone retrieval from GOME UV spectral data using the weighting function DOAS approach." *Atmos. Chem. Phys.* 5 (2005): 1015–1025.

Dalaudier, F., V. Kan, and A.S Gurvich. "Chromatic refraction with global ozone monitoring by occultation of stars. I. Description and scintillation correction." *Appl. Opt.* 40 (2001): 866-877.

Damski, J., et al. "A chemistry-transport model simulation of middle atmospheric ozone from 1980 to 2019 using coupled chemistry GCM winds and temperatures." *Atmos. Chem. Phys.* 7 (2007): 2165–2181.

Davis, S. P., M. C. Abrams, and J. W. Brault, Fourier Transform Spectroscopy (Academic, 2001).

Degenstein, D. A., et al. "Limb scatter ozone retrieval from 10 to 60 km using a multiplicative algebraic reconstruction technique." *Atmos. Chem. Phys.* 9 (2009): 6521-6529.

Doicu, A, et al. *Numerical regularization for atmospheric inverse problems.* Berlin Heidelberg : Springer-Verlag, 2010.

Dudhia, A., V. L. Jay, and C. D. Rodgers. "Microwindow selection for high-spectral-resolution sounders." *App. Opt.* 41 (2002): 3665-3673.

Ebojie, F. et al. „Tropospheric column amount of ozone retrieved from SCIAMACHY limb-nadir-matching observations, Atmos. Meas. Tech., 7, 2073 – 2096, 2014.

Ebojie, F. Tropospheric ozone columns retrieval from SCIAMACHY limb-nadir-matching observations, PhD Thesis, 2014.

Echle, G, et al. "Optimized spectral microwindows for data analysis of the Michelson Interferometer for Passive Atmospheric Sounding on the Environmental Satellite." *Appl. Opt.* 39 (2000): 5531-3340.

ECMWF. *ECMWF Data Base.* 2013. http://www.ecmwf.int/products/data/archive/ (accessed November 28, 2013).

Elsasser, W.M.. Heat Transfer by Infrared Radiation in the Atmosphere, Harvard Meteor. Studies, 6. Harvard University Press, 1942.

ENVISAT. 2011. http://earth.esa.int/pub/ESA_DOC/ENVISAT (accessed November 23, 2011).

Eriksson, P., C. Jiménez, and S. Buehler. "Qpack: A tool for instrument simulation and retrieval work." *J. Quant. Spectrosc. Radiat.Transfer* 91 (2005): 47-61.

Eriksson, P., M. Ekström, S. Buehler, and C. Melsheimer. "Efficient forward modelling by matrix representation of sensor responses." *Int. J. Remote Sensing* 27 (2006): 1793-1808.

Fischer, J., R. R. Gamache, A. Goldman, L. S. Rothman, and A. Perrin (2003), Total internal partition sums in the 2000 edition of the HITRAN database, J. Quant. Spectrosc. Radiat. Transfer 82, 401– 412.

Flittner, D. E., P. K. Bhartia, and B. M. Herman. "O3 profiles retrieved from limb-scatter measurements: Theory." *Geophys. Res. Lett.* 27 (2000): 2601-2604.

Fortuin, J.P.F., and H. Kelder. "An ozone climatology based on ozonesondes and satellite measurements." *J. Geophys. Res.* 103 (1999): 31709-31734.

Frisk, U., et al. "The Odin satellite." *Astron. Astrophys.* 402 (2003): L27–L34.

Fussen, D., and C. Bingen. "A volcanism dependent model for the extinction porifle of stratospheric aerosols in the UV-visible range." *Geophys. Res. Lett.* 22 (1999): 703-706.

GCOS-107. "Global Climate Observing System (GCOS), Systematic Observation Requirements for Satellite-based Products for climate, Supplemental details to the satellite-based component of the "Implementation Plan for the Global Observing System for Climate." 2006.

Glatthor, N., et al. "Retrieval of stratospheric Ozone Profiles from MIPAS/ENVISAT limb emission spectra: a sensitivity study." *Atmos. Chem. Phys.* 6 (2006): 2767-2781.

Grainger, J., and J. Ring. "Anomalous Fraunhofer line profiles." *Nature* 193 (1962): 762-762.

Hales, T. C. Jordan's Proof of the Jordan Curve Theorem, Studies in Logic, Grammar and Rhetoric, 10 (23), 2007.

Hasekamp, O., and J. Landgraf. "Ozone profile retrieval from backscattered ultraviolet radiances: The inverse problem solved by regularization." *J. Geophys. Res.* 106 (2001): 8077-8088.

Hughes, I., and T. Hase. *Measurements and their Uncertainties: A practical guide to modern error analysis.* OUP Oxford, 2010.

Hughes, R. C., C. Boone, and P. F. Bernath, (2014), ACE-FTS Spectroscopy – Version 3.5, ACE Project Report, 74 pages.

Hurtmans, D.; Coheur, P.; Wespes, C.; Clarisse, L.; Scharf, O.; Clerbaux, C.; Hadji-Lazaro, J.; George, M. & Turquety, S. FORLI radiative transfer and retrieval code for IASI. *J. Quant. Spectrosc. Radiat. Transfer , 113*, 1391-1408, 2012.

Joiner, J., P.K. Barthia, R.P. Cebula, E. Hilsenrath, R.D. Mcpeters, and H. Park. "Rotational Raman scattering (Ring effect) in satellite backscatter ultraviolet measurements." *Appl. Opt.* 34 (1995): 4513-4525.

Jordan, M. C.: Cours d'Analyse de l'Ecole Polythechnique, Band 3, Paris , 1887.

Kerridge, B.J.K., R. Siddans, B.L. Latter, J.P. Burrows, M. Weber, R. De Beek, I. Aben, W. Hartman. "GOME-2 Error Assessment Study. Final Report EUMETSAT Contract No EUM/CO/01/901/DK." 2002.

Koelemeijer, R., J. de Haan, J. Hovenier, and P. Stammes. "A database of spectral surface reflectivity in the range 335-772 nm derived from 5.5 years of GOME observations." *J. Geophys. Res.* 108 (2003): D4070.

Krol, M., et al. "The two-way nested global chemistry-transport zoom model TM5: algorithm and applications." *Atmos. Chem. Phys.* 5 (2005): 417-432.

Kyrölä, E., E. Sihvola, Y. Kotivuori, M. Tikka, T. Tuomi, and and H. Haario. "Inverse Theory for Occultation Measurements, 1: Spectral Inversion." *J. Geophys. Res.* 38 (1993): 7367-7381.

Kyrölä, E., et al. "Retrieval of atmospheric parameters from GOMOS data." *Atmos. Chem. Phys.* 10 (2010): 11881-11903.

Kuntz, M. (1997), A new implementation of the Humlicek algorithm for the calculation of the Voigt profile function, J. Quant. Spectrosc. Radiat. Transfer, 57, 819-824, doi:10.1016/S0022-4073(96)00162-8.

Laeng, A., Hubert, D., Verhoelst, T., von Clarmann, T., Dinelli, B. M., Dudhia, A., Raspollini, P., Stiller, G., Grabowski, U., Keppens, A., Kiefer, M., Sofieva, V., Froidevaux, L., Walker, K. A., Lambert, J.-C., and Zehner, C.: The Ozone Climate Change Initiative: comparison of four Level 2 Processors for the Michelson Interferometer for Passive Atmospheric Sounding (MI- PAS), Remote Sens. Environ., in press, 2014.

Lamsal, L. N., M. Weber, S. Tellmann, and J. P. Burrows. "Ozone column classified climatology of ozone and temperature profiles based on ozonesonde and satellite data." *J. Geophys. Res.* 109 (2004): D20304.

Lerot, C., et al. "Homogenized total ozone data records from the European sensors GOME/ERS-2, SCIAMACHY/Envisat and GOME-2/MetOp-A." *J. Geophys. Res.*, 119, 3, 1639-1662, doi:10.1002/2013JD020831, 2014.

Levenberg, A. "A method for the solution of certain non-linear problems in least squares." *Q. Appl. Math.* 2 (1944): 164-168.

Loyola, D. G., and M. Coldewey-Egbers. "Multi-sensor data merging with stacked neural networks for the creation of satellite long-term climate data records." *EURASIP J. Adv. Signal Proc. 2012* 2012 (2012): 91.

Loyola, D., et al. "Global long-term monitoring of the ozone layer - a prerequisite for predictions." *Int. J. Remote Sens.* 30 (2009): 4295-4318.

Loyola, D., W. Thomas, R. Spurr, and B. Mayer. "Global patterns in daytime cloud properties derived from GOME backscatter UV-VIS measurements." *Int. J. Remote Sensing* 13 (2010): 4295-4318.

Marquardt, D. W. "An algorithm for least-squares estimation of nonlinear parameters." *J. Soc. Ind. Appl. Math.*, 1963: 431-441.

Matthews, E. "Global vegetation and land use: new high resolution data bases for climate studies." *J. Clim. Appl. Meteo.* 22 (1983): 474-487.

McPeters, R.D., G.J. Labow, and J.A. Logan. "Ozone climatological profiles for satellite retrieval algorithms." *J. Geophys. Res.* 112 (2007): D05308.

Melsheimer, C., et al. "Intercomparison of general purpose clear sky atmospheric radiative transfer models for the millimeter/submillimeter spectral range." *Radio Sci.* 40 (2005): RS1007.

Menke, W. *Geophysical Data Analysis: Discrete Inverse Theory.* San Diego California: Academic, 1984.

Mieruch, S., et al. "Global and long-term comparison of SCIAMACHY limb ozone profiles with correlative satellite data (2002–2008)." *Atmos. Meas. Tech.* 5 (2012): 771–788.

Munro, R., R. Siddans, W.J. Reburn, and B.J. Kerridge. "Direct measurement of tropospheric ozone distributions from space." *Nature* 392 (1998): 168-171.

Murtagh, D., et al. "An overview of the Odin atmospheric mission." *Can. J. Phys.* 80 (2002): 309–319.

O3_CCI-URD. "Ozone_cci User Requirement Document, Issue 2.0, 15/06/2011." 2011.

Olberg, M., et al. "The Odin satellite." *Astron. Astrophys.* 402 (2003): L35–L38.

Papandrea, E, et al. "Two-dimensional tomographic retrieval of MIPAS/ENVISAT measurements of ozoneand related species." *Int. J. Rem. Sens.* 31 (2010): 477-483.

Picone, J. M., A. E. Hedin, D. P. Drob, and A. C. Aikin (2002), NRLMSISE-00 empirical model of the atmosphere: statistical comparisons and scientific issues, J. Geophys. Res. 107, 1468-1483.

Press, W. H., S. A. Teukolsky, W. T. Vetterling, and B. P. Flannery. *Numerical Recipes in Fortran 77, The Art of Scientific Computing, Second Edition.* Cambridge University Press, 933, 1992.

Rahpoe, N., C. von Savigny, M. Weber, A. V. Rozanov, H. Bovensmann, and J. P. Burrows. "Error budget analysis of SCIAMACHY limb ozone profile retrievals using the SCIATRAN model." *Atmos. Meas. Tech.* 6 (2013): 2825–2837.

Rodgers, C. D. *Inverse Methods for Atmospheric Sounding: Theory and Practice.* World Scientific, 2000.

Rodgers, C. D. "The Characterization and Error Analysis of Profiles Retrieved from Remote Sounding Measurements." *J. Geophys. Res.* 95 (1990): 5587-5595.

Rodgers, C. D., and B. J. Connor. "Intercomparison of remote sounding instruments." *J. Geophys. Res.* 108 (2003).

Rodgers, C.D. "Retrieval of atmospheric temperature and composition from remote measurements of thermal radiation." *Rev. Geophys.* 14 (1976): 609-624.

Roth, C.Z., D.A. Degenstein, A.E. Bourassa, and E.J. Llewellyn. "The Retrieval of Vertical Profiles of the Ozone Number Density Using Chappuis Band Absorption Information

and a Multiplicative Algebraic Reconstruction Technique." *Can. J. Phys.* XX (2007): 1225-1250.

Rothman, L.; I.E. Gordon; A. Barbe; D.Chris Benner; P.F. Bernath; M. Birk; V. Boudon; L.R. Brown; A. Campargue; J.-P. Champion; K. Chance; L.H. Coudert; V. Dana; V.M. Devi; S. Fally 1; J.-M. Flaud; R.R. Gamache; A. Goldman; D. Jacquemart; I. Kleiner; N. Lacome; W.J. Lafferty; J.-Y. Mandin; S.T. Massie; S.N. Mikhailenko; C.E. Miller; N. Moazzen-Ahmadi; O.V. Naumenko; A.V. Nikitin; J. Orphal; V.I. Perevalov; A. Perrin; A. Predoi-Cross; C.P. Rinsland; M. Rotger f; M. Šimečková 2; M.A.H. Smith; K. Sung; S.A. Tashkun; J. Tennyson; R.A. Toth; A.C. Vandaele & Auwera, J. V. The HITRAN 2008 molecular spectroscopic database. *J. Quant. Spectrosc. Radiat. Transfer, 110(9-10)*, 533-572, 2009.

Rozanov, V. V., M. Buchwitz, K.-U. Eichmann, R. De Beek, and J. P. Burrows. "SCIATRAN - a new radiative transfer model for geophysical applications in the 240 - 2400 nm spectral region: The pseude-spherical version." *Adv. Space. Res.* 29 (2002): 1831-1835.

Rozanov, V.V., A.V. Rozanov, A.A. Kokhanovsky, and J.P. Burrows. "Radiative transfer through terrestrial atmosphere and ocean: Software package SCIATRAN." *J. Quant. Spectrosc. Rad. Transfer* 133 (2014): 13-71.

Rozanov, V.V., D. Diebel, R.J.D. Spurr, and J.P. Burrows. "GOMETRAN: A radiative transfer model for the satellite project GOME - the plane-parallel version." *J. Geophys. Res.* 102 (1997): 16683-16695.

SCIATRAN. "Radiative Transfer Model and Retrieval Algorithm, Version 2.2, User's Guide for the Software Package SCIATRAN." 2002.

Ruyten, W. (2004), Comment on "A new implementation of the Humlicek algorithm for the calculation of the Voigt profile function" by M. Kuntz [JQSRT 57(6) (1997) 819–824], J. Quant. Spectrosc. Radiat. Transfer, 86, 231-233, doi:10.1016/j.jqsrt.2003.12.027.

Segers, A.J., H. J. Eskes, R. J. van der A, R. F. van Oss, and P. F. J. van Velthoven. "Assimilation of GOME ozone profiles and a global chemistry-transport model using a Kalman filter with anisotropic covariance." *Quart. J. Roy. Met. Soc.* 131 (2005): 477-502.

Siddans, R. *Height Resolved Ozone Retrievals from Global Ozone Monitoring Experiment.* PhD Thesis, University of Reading, 2003.

Sihvola, E. *Coupling of spectral and vertical inversion in the analysis of stellar occultation data.* Helsinki: Finnish Meteorological Institute, 1994.

Sofieva, V. F. et al : Merged SAGE II, Ozone_cci and OMPS ozone profile dataset and evaluation of ozone trends in the stratosphere, Atmos. Chem. Phys., 17, 12533-12552, https://doi.org/10.5194/acp-17-12533-2017, 2017b

Sofieva, V. F. et al: Improved GOMOS/Envisat ozone retrievals in the upper troposphere and the lower stratosphere, Atmos. Meas. Tech., 10, 231-246, doi:10.5194/amt-10-231-2017, 2017a

Sofieva, V. F., Kalakoski, N., Päivärinta, S.-M., Tamminen, J., Laine, M., and Froidevaux, L.: On sampling uncertainty of satellite ozone profile measurements, Atmos. Meas. Tech., 7, 1891-1900, doi:10.5194/amt-7-1891-2014, 2014, http://www.atmos-meas-tech.net/7/1891/2014/

Sofieva, V. F. et al. "Retrievals from GOMOS stellar occultation measurements using characterization of modeling errors." *Atmos. Meas. Tech.* 3 (2010): 1019-1027.

Sofieva, V. F., et al. "Harmonized dataset of ozone profiles from satellite limb and occultation measurements." *Earth Syst. Sci. Data* 5 (2013): 349–363.

Sofieva, V. F., et al. "Influence of scintillation on quality of ozone monitoring by GOMOS." *Atmos. Chem. Phys.* 9 (2009): 9197-9207.

Sofieva, V. F., J. Tamminen, H. Haario, E. Kyrölä, and M. Lehtinen. "Ozone profile smoothness as a priori information in the inversion from limb measurements." *Ann. Geophysicae* 22 (2004): 3411-3420.

Sonkaew, T., V.V. Rozanov, C. von Savigny, A. Rozanov, H. Bovensmann, and J. P. Burrows. "Cloud sensitivity studies for stratospheric and lower mesospheric ozone profile retrievals from measurements of limb-scattered solar radiation." *Atmos. Meas. Tech.* 2 (2009): 653-678.

Spang, R., J. Remedios, and M. Barkley. "Colour Indices for the Detection and Differentiation of Cloud Types in Infra-red Limb Emissions Spectra." *Adv. Space Res.* 33 (2004): 1041-1047.

Spurr, R. "LIDORT and VLIDORT: Linearized pseudo-spherical scalar and vector discrete ordinate radiative transfer models for use in remote sensing retrieval problems." In *Light Scattering Reviews, Volume 3*, by A. A. Kokhanovsky (ed.). Springer, 2008.

Spurr, R. "Simultaneous derivation of intensities and weighting functions in a general pseudo-spherical discrete ordinate radiative transfer treatment." *J. Quant. Spectrosc. Radiat. Transfer* 75 (2002): 129-175.

Spurr, R., and V. Natraj. "A linearized two-stream radiative transfer code for fast approximation of multiple-scatter fields." *J. Quant. Spectrosc. Radiat. Transfer* 112 (2011): 2630-2637.

Spurr, R., et al. *GOME/ERS-2 – GDP5.0 Upgrade of the GOME Data Processor for Improved Total Ozone Columns.* Algorithm Theoretical Basis Document, http://atmos.caf.dlr.de/gome/docs/DLR_GOME_GDP5_ATBD.pdf, 2011.

Spurr, R., V. Natraj, C. Lerot, M. Van Roozendael, and D. Loyola. "Linearization of the Principal Component Analysis method for radiative transfer acceleration: Application to retrieval algorithms and sensitivity studies." *J. Quant. Spectrosc. Radiat. Transfer* 125 (2013): 1-17.

Spurr, R.J.D., et al. "Algorithm Theoretical Basis Document: GOME Direct Fitting Phase-B (GODFIT-2)." 2007.

Stamnes, K., S.-C.Tsay, W. Wiscombe, and K. Jayaweera. "Numerically stable algorithm for discrete ordinate method radiative transfer in multiple scattering and emitting layered media." *App. Opt.*, 1988: 2502-2509.

Steck, T. et al. "Bias determination and precision validation of ozone profiles from MIPAS-Envisat retrieved with the IMK-IAA processor." *Atmos. Chem. Phys.* 7 (2007): 3639–3662.

Stolarski, R.S., and S. Frith. "Search for evidence of trend slow-down in the long-term TOMS/SBUV total ozone data record: importance os instrument drift uncertainty." *Atmos. Chem. Phys.*, 2006: 4057-4065.

Tamminen, J., E. Kyrölä, and V. Sofieva. "Does prior information improve measurements?" *Occultations for Probing Atmosphere and Climate - Science from the OPAC-1 Workshop, edited by G. Kirchengast, U. Foelsche, and A. K. Steine.* Springer-Verlag, 2004. 87-98.

Tukiainen, S., Kyrölä, E., Verronen, P. T., Fussen, D., Blanot, L., Barrot, G., Hauchecorne, A., and Lloyd, N.: Retrieval of ozone profiles from GOMOS limb scattered measurements, Atmos. Meas. Tech., 4, 659-667, doi:10.5194/amt-4-659-2011, 2011.

Tukiainen, S., Kyrölä, E., Tamminen, J., Kujanpää, J., and Blanot, L.: GOMOS bright limb

ozone data set, Atmos. Meas. Tech., 8, 3107-3115, doi:10.5194/amt-8-3107-2015,2015.

Turner, D. S.. Systematic errors inherent in the current modeling of the reflected downward flux term used by remote sensing models. *Appl. Opt.*, 43(11):2369-2383, 2004.

Urban, J., et al. "MOLIERE (v5): A versatile forward- and inversion model for the millimeter and sub-millimeter wavelength range." *J. Quant. Spectrosc. Radiat. Transfer* 83 (2004): 529-554.

Urban, J., et al. "Odin/SMR limb observations of stratosperic trace gases: Level-2 processing of ClO, N2O, O3, and HNO3." *J. Geophys. Res.* 110 (2005): D14307.

—. "Odin/SMR Limb Observations of Trace Gases in the Polar Lower Stratosphere during 2004-2005." *Proc. ESA Atmospheric Science Conference, 8-12 May 2006.* Frascati, Italy: European Space Agency, 2006.

Valks, P., et al. "Tropical tropospheric ozone column retrieval for GOME-2", Atmos. Meas. Tech., 7, 2513-2530, doi:10.5194/amt-7-2513-2014, 2014.

Van Oss, R., and R.J.D .Spurr. "Fast and accurate 4 and 6 stream linearised discrete ordinate radiative transfer models for ozone profile remote sensing retrieval." *J. Quant. Spectrosc. Radiat. Transfer* 75 (2002): 177-220.

Van Oss, R., R. Voors, and R. Spurr. "Ozone Profile Algorithm." OMI Algorithm Theoretical Basis Document, Volume II, OMI Ozone products, ATBD-OMI-02, Version 2.0, 2002., 2002.

Van Roozendael, M., et al. "Fifteen years of GOME/ERS2 total ozone data: the new direct-fitting GOME Data Processor (GDP) Version 5: I. Algorithm Description." *J. Geophys. Res.* 117 (2012): D03305.

Van Roozendael, M., et al. "Ten years of GOME/ERS2 total ozone data: the new GOME Data Processor (GDP) Version 4: I. Algorithm Description." *J. Geophys Res.* 111 (2006): D14311.

von Clarmann, T, et al. "Retrieval of temperature, H2O, O3, HNO3, CH4, N2O, ClONO2 and ClO from MIPAS reduced resolution nominal mode limb emission measurements." *Atmos. Meas. Tech., 2*, 2009: 159-175.

von Clarmann, T. "Validation of remotely sensed profiles of atmospheric state variables: strategies and terminology." *Atmos. Chem. Phys.* 6 (2006): 4311-4320.

von Clarmann, T., et al. "Retrieval of temperature and tangent altitude pointing from limb emission spectra recorded from space by the Michelson Interferometer for Passive Atmospheric Sounding (MIPAS)." *J. Geophys. Res.* 108 (2003).

von Clarmann, T; Echle, G. "Selection of optimized microwindows for atmospheric spectroscopy." *Appl. Optics, 37*, 1998: 7661-7669.

von Savigny, C., et al. "The ozone hole break-up in September 2002 as seen by SCIAMACHY on ENVISAT." *J. Atm. Sci.* 62 (2005): 721-734.

Wan, Z.: New refinements and validation of the MODIS Land-Surface Temperature/Emissivity products. *Remote Sens. Environ.*, 112(1):59-74, 2008.

Wang, P., Stammes, P., van der A, R., Pinardi, G., and van Roozendael, M.: FRESCO+: an improved O2 A-band cloud retrieval algorithm for tropospheric trace gas retrievals, Atmos. Chem. Phys., 8, 6565-6576, doi:10.5194/acp-8-6565-2008, 2008.

Wellemeyer, C., S. Taylor, C. Seftor, R. McPeters, and P. Bhartia. "A correction for total ozone mapping spectrometer profile shape errors at high latitude." *J. Geophys. Res.* 102 (1997): 9029-9038.

WGS 84 Implementation Manual Version 2.4 (European Organization for the Safety of Air Navigation, Brussels, Belgium, the Institute of Geodesy and Navigation, University FAF, Munich, Germany, 1998).

WMO: Meteorology – A three-dimensional science: Second sessionof the Commission for Aerology, WMO Bull., IV, 134–138, 1957

Ziemke, J.R., S. Chandra, G. J. Labow, P. K. Bhartia, L. Froidevaux, and J. C. Witte. "A global climatology of tropospheric and stratospheric ozone derived from Aura OMI and MLS measurements." *Atmos. Chem. Phys.* 11 (2011): 9237–9251.

Zhou, D. K.; Larar, A. M.; Liu, X.; Smith, W. L.; Strow, L. L.; Yang, P.; Schluessel, P. & Calbet, X. Global Land Surface Emissivity Retrieved From Satellite Ultraspectral IR Measurements. *IEEE Trans. Geosci. Remote Sens.*, 49(4):1277-1290, 2011.